UNIVERSITY OF CALIFORNIA
SANTA CRUZ

STELLAR MASS BUILDUP IN GALAXIES IN THE FIRST 1.5 GYR OF THE UNIVERSE.

A dissertation submitted in partial satisfaction of the
requirements for the degree of

DOCTOR OF PHILOSOPHY

in

ASTRONOMY AND ASTROPHYSICS

by

Valentino Gonzalez

June 2012

The Dissertation of Valentino Gonzalez
is approved:

Garth Illingworth, Chair

Sandra Faber

Piero Madau

Pascal Oesch

Tyrus Miller
Vice Provost and Dean of Graduate Studies

Table of Contents

List of Figures

List of Tables

Abstract

Stellar Mass Buildup in Galaxies in the First 1.5 Gyr of the Universe.

by

Valentino Gonzalez

The buildup of galaxies is one of the most fundamental questions in modern cosmology. The study of this process in the first few Gyr of the Universe, starting from the first stars, is a challenging endeavor. In this thesis we have made extensive use of the deepest optical and infrared images currently available from the *Hubble Space Telescope* (*HST*) and the *Spitzer Space Telescope* to study the properties of the stellar populations and the stellar mass buildup in galaxies in the first 1.5 Gyr after the Big Bang.

We have studied the spectral energy distributions (SEDs) of $z \sim 4-8$ Lyman break galaxies (LBGs) in the rest-frame UV and optical and compared them to synthetic stellar population models to learn about the properties of these galaxies. We have found that the typical best fit ages for these systems are in the range $300-600$ Myr. In a more general context this is not a very old population but at $z \gtrsim 4$ this represents a large fraction of the cosmic time, indicating that these galaxies likely started forming stars much earlier, at $z \gtrsim 10$.

The star formation Rates (SFRs) estimated for LBGs at $z \gtrsim 4$ are generally in the range $1-100\,M_{\odot}$ yr^{-1}. The stellar mass estimates are most robust for sources with good *Spitzer*/IRAC detections, corresponding to galaxies with stellar masses $\gtrsim 10^{8.5}\,M_{\odot}$ at $z \sim 4$ ($\gtrsim 10^{9.5}\,M_{\odot}$ at $z \sim 7$). For sources with lower rest-frame optical luminosities, that, as a result, are individually undetected in IRAC, their average stellar masses have been studied in a stacking analysis of a large number of sources. This enables us to reach stellar masses $\sim 10^{7.8}\,M_{\odot}$ at $z \sim 4$. The stellar masses show a fairly tight correlation with UV luminosity or SFR, and the zeropoint of the relation does not seem to evolve strongly with redshift. This relation is a

direct reflection of a correlation between the UV and optical colors and it favors a typical star formation history (SFH) at high redshift in which the SFR of a galaxy increases as a function of time. This is consistent with the observed brightening of the UV luminosity function (UV LF) and with expectations from numerical simulations.

We have taken advantage of the UV luminosity vs. stellar mass relation observed in LBGs at $z \gtrsim 4-7$ to derive the stellar mass function (SMF) of galaxies at these redshifts. The method uses a combination of the UV LF and the mean UV vs. stellar mass relation (including the scatter, estimated to be ~ 0.5 dex at bright luminosities at $z \sim 4$). This method allows an analytic estimate of the low mass slope of the SMF. This slope (the power-law exponent of the SMF at low masses), is estimated to be in the $-1.44 - -1.55$, range which is flatter than the UV LF faint end slope at these redshifts ($\lesssim -1.74$). This means that low mass systems contribute less to the total stellar mass density (SMD) of the Universe than would have been estimated assuming a constant mass-to-UV-light ratio. We show that this is also much flatter than the theoretical predictions from simulations, which generally over-predict the number density of low mass systems at these redshifts.

The UV luminosity vs. stellar mass relation indicates only a small variation of the mass-to-light ratio as a function of UV luminosity. This is confirmed in a stacking analysis of a large number of sources from the HUDF and the Early Release Science fields (~ 400 $z \sim 4$, ~ 120 $z \sim 5$, ~ 60 $z \sim 6$, 36 at $z \sim 7$). Interestingly, the stacked SEDs at $z \gtrsim 5$ in the rest-frame optical shows a color $[3.6]-[4.5] \sim 0.3$ mag. This color is hard to reproduce by synthetic stellar population models that only include stellar continua, and it probably indicates the presence of moderately strong emission lines (Hα EW$_{\rm rest}$ ~ 300 Å). The contribution from such emission lines in the IRAC fluxes indicates that the stellar masses and ages could both be over-estimated by a factor ~ 2.

One of the most interesting results presented in this thesis is the apparent plateau of the specific SFR (sSFR = SFR / stellar mass). In early results, the similarity in the SEDs of

galaxies at a given UV luminosity in the $z \sim 4-7$ redshift range resulted in very similar estimates of the SFR and stellar masses of these galaxies. Furthermore, we find that the reported sSFR estimates at $z \sim 2$ are also very similar to the ones in the $z \sim 4-7$ redshift range ($\sim 2\,\mathrm{Gyr}^{-1}$ for $\sim 5 \times 10^9\,M_\odot$ galaxies). A puzzle arises from the fact that the dark matter accretion rate onto halos is predicted to decrease monotonically and rather fast as a function of cosmic time (approximately $\propto (1+z)^{2.5}$). If gas and star formation follow the inflow of dark matter, the sSFR at a constant mass should also decrease monotonically with time, which is contrary to the indication from these observations. When we include the possible effects of emission lines, the stellar masses decrease by a factor $\sim 2\times$ at $z \gtrsim 5$. The revised stellar masses may favor a slowly rising sSFR at $z \gtrsim 2$, but the rise as a function of redshift is still much slower (sSFR(z) $\propto (1+z)^{0.7}$) than that of specific dark matter accretion rate. This suggests that the stellar mass buildup is somehow decoupled from the dark matter buildup at early times.

A detailed understanding of the connection between the buildup of galaxy mass and dark matter is key for models of galaxy formation in the early Universe. It will be crucial to expand on analyses like the one presented here, including larger samples and broader stellar mass ranges, to explore the buildup of galaxies with improved statistics. Wide-area surveys with newly acquired *HST* and *Spitzer* data, and the upcoming generation of instruments, will likely provide the opportunity to make such a connection.

A mis padres,

Rosa y Valentino.

Acknowledgments

The work presented in this thesis is the product of several years of collaboration with a great team of scientists. I will be forever grateful for having the opportunity to work and learn from such wonderful characters. In particular, my advisor Garth Illingworth, Rychard Bouwens, and Ivo Labbe provided invaluable guidance and encouragement along the way. Their constant excitement and enthusiasm for the study of the most distant galaxies, and in general for pushing the limits of what seems possible is perhaps the most important lesson I learned from them. I am very thankful to Marijn Franx, whose insight was always a great contribution to the work developed in this thesis. I am also thankful to Pascal Oesch with whom I had the privilege to collaborate and share interesting discussions that have sparked ideas the we will hopefully develop in the future.

The text of this dissertation includes reprints of the following previously published material: (i) Gonzalez, V., Labbé, I., Bouwens, R., Illingworth, G., Franx, M., Kriek, M., and Brammer, G. 2010, ApJ 713, 115, (ii) Labbé, I., Gonzalez, V., Bouwens, R., Illingworth, G., Franx, M., Trenti, M., Oesch, P., van Dokkum, P., Stiavelli, M., Carollo, M., Kriek, M., Magee, D. 2010, ApJ 716, L103, (iii) Gonzalez, V., Labbé, I., Bouwens, R., Illingworth, G., Franx, M., Kriek, M. 2011, ApJ 735, L34 (iv) Gonzalez, V., Bouwens, R., Labbé, I., Illingworth, G., Oesch, P., Franx, M., and Magee, D. 2011 arXiv:1110.6441 (submitted to ApJ). I was the lead author in articles (i), (iii), and (iv), and I am responsible for the majority of the work presented in them. In article (ii) I am the second author and was responsible for most of the *Spitzer*/IRAC data analysis. These data and the analysis was subsequently used to complement articles (iii) and (iv). Articles (i) through (iv) are presented as Chapters 2 through 5.

This research was supported by NASA grants NAG5-7697, HST-GO10937, HST-GO11563, HST-GO11144. I am also grateful for the support provided from a joint Fulbright-CONICYT fellowship. This work is based in part on observations made with NASA/ESA the Hubble Space

Telescope, obtained at the Space Telescope Science Institute. STScI is operated under the Association of Universities for Research in Astronomy, Inc. under NASA contract NAS 5-26555. Based in part on observations made with the Spitzer Space Telescope, which is operated by the Jet Propulsion Laboratory, California Institute of Technology under contract with NASA.

While working on this thesis I had the privilege to live in the wonderful city of Santa Cruz, CA. In this city, I had the fortune to meet some of the most extraordinary friends one can ask for. I will always remember Sonia, Javiera, Luis, Maïté, and Daniel for their fun and stimulating company. Especially, I will be forever thankful to them for taking care of me at times when I could not do it myself.

For many years now, Feña has been my partner in life, sharing both the good and the bad of our adventure in these foreign lands. She has been a source of what at times seems infinite patience and support. Working in this thesis would have certainly not been the same without her company. I am very grateful to Feña for making my life so much happier.

Finally, all I may accomplish in life is thanks to the amazing parents I have the good fortune to have. They gave me a happy and stimulating childhood, infinite love, and an education that their money could not buy. In a country where education has for many years been used as a tool to perpetuate social injustice, they managed to open doors that were meant to be close for people like me and my brother. Their infinite love, encouragement, and inspiration have taken me where I am and I will always be grateful for that.

Chapter 1

Introduction

One of the most important questions in modern observational cosmology concerns the mass growth of galaxies, from the very first stars to the galaxy population observed in the local Universe. The stellar mass content that we observe in galaxies today started its assembly quite early in the history of the Universe. Simulations predict that the first stars, which formed out of primordial, metal free gas, first appeared around 100-200 Myrs after the Big-Bang, or at $z \sim 20 - 30$. These so called population III stars were massive and short lived, and their explosions polluted their surroundings with the first metals, which in turn facilitated the cooling of gas necessary to form the next generation of stars. Tracing the build-up of stellar mass from as early as possible all the way to the observed structure of the local Universe is very fundamental question of observational cosmology. Characterizing the properties of the first formed galaxies and their rate of growth will provide important clues to understand the very early stages of galaxy formation and evolution, which in the local Universe can only be studied indirectly.

Finding the first galaxies ever formed, however, represents a challenge that we have still been unable to meet. The reasons for this are not surprising. First and foremost, the observed bolometric surface brightness of the sources, decreases rapidly with redshift as $(1+z)^4$ requiring very deep integrations to be able to detect the most distant sources. Another important factor is

that due to the expansion of the Universe, the bulk of the light of these galaxies has been shifted to infrared wavelengths, where the atmosphere becomes too bright for effective ground-based observations, and where our best detectors are less sensitive.

Due to the limitations mentioned above, we have still been unable to observe the very first galaxies ever formed in the Universe. In the recent years, however, there has been substantial progress in pushing the frontier of the most distant galaxy observations much closer to the Big-Bang.

1.1 Finding the Most Distant Galaxies

Despite the previously described difficulties associated with the search for very distant galaxies, today we know thousands of galaxies at $z \gtrsim 4$ (only 1.5 Gyr after the Big-Bang), and even hundreds of candidates have been identified at $z \sim 7$ and 8. This pushes our frontier to only $\sim 600\,\mathrm{Myr}$ after the Big-Bang, and provides an opportunity to study galaxy build-up in the primordial Universe, when galaxies are still in the early stages of assembly and appear to be growing rapidly. The success in finding galaxies at $z > 4$ is due, for the most part, to the development of two search techniques, both of which rely in observations of the rest-frame far-UV light from these galaxies.

The two most successful techniques at identifying the highest redshift sources are the searches for *Lyman-α emitters*, and the *Lyman Break Galaxy* (LBG) technique. Lyman-α emitters are identified in narrow band filter surveys that aim at detecting strong Lyman-α emission. Follow up spectroscopy of the candidates is necessary to confirm that the emission line detected in the narrow band filter corresponds, in fact, to Lyα. The LBG technique, meanwhile, takes advantage of the large optical depth of the intergalactic medium (IGM) at wavelengths shorter than the Lyman limit. At $z \gtrsim 2$, the hydrogen gas in the IGM is mostly ionized but there are still numerous clouds of neutral hydrogen. These clouds absorb in the Lyman series in their

rest-frame, causing line blanketing at wavelengths shorter than the Lyα line ($\lambda = 1216\,$Å), and a sharp break bluewards of the Lyman limit ($\lambda = 912\,$Å). At higher redshift, neutral hydrogen becomes more abundant, which results in increasingly stronger breaks closer to the wavelength of Lyα as one approaches the epoch of reionization at $z \sim 6$. By using a set of broad-band filters, it is possible to search for galaxies that exhibit very red colors across the wavelength of the break and then typically blue colors at longer wavelengths, indicative of galaxies that are actively forming stars. Both these techniques have been extensively applied both in the field and also in searches behind massive galaxy clusters. Taking advantage of the gravitational magnification produced by the clusters, the searches for the first galaxies behind massive clusters will enable the study of the very faint end of the galaxy population, which would require much deeper observations than currently feasible for field galaxy surveys.

This thesis focuses on the observational study of the rest-frame UV and rest-frame optical properties of galaxies at $z \gtrsim 4$ and is based exclusively on the searches for LBGs in the field. These observations are used to model the physical properties of these galaxies, with special emphasis on the stellar mass buildup exhibited from the earliest times accessible with current data. We focus first on describing the LBG technique in more detail with a short discussion of its advantages and weaknesses compared to other alternatives.

1.1.1 The Lyman Break Galaxy Technique

Pioneered by Steidel et al. (1996), the LBG technique provided the first large samples of galaxies at $z \sim 2-3$, an epoch which was largely unexplored at the time due to the difficulties of finding galaxy candidates. Through a large investment of telescope time, the Steidel et al. group showed that galaxies at these redshifts could be effectively selected based on a limited set of broad-band colors. This a very cost-effective technique to find distant galaxies but an extensive spectroscopic follow up was required to confirm the redshifts of the candidate galaxies. Spectroscopic identifications are based primarily on Lyα emission. For the brightest population,

it is also possible to establish spectroscopic redshifts based on the UV continuum break in the spectra and on stellar absorption features in the far UV. These follow-up observations have permitted establishing the redshift distributions of the LBGs and the contamination rates expected from samples selected with this technique (typically 10-20%).

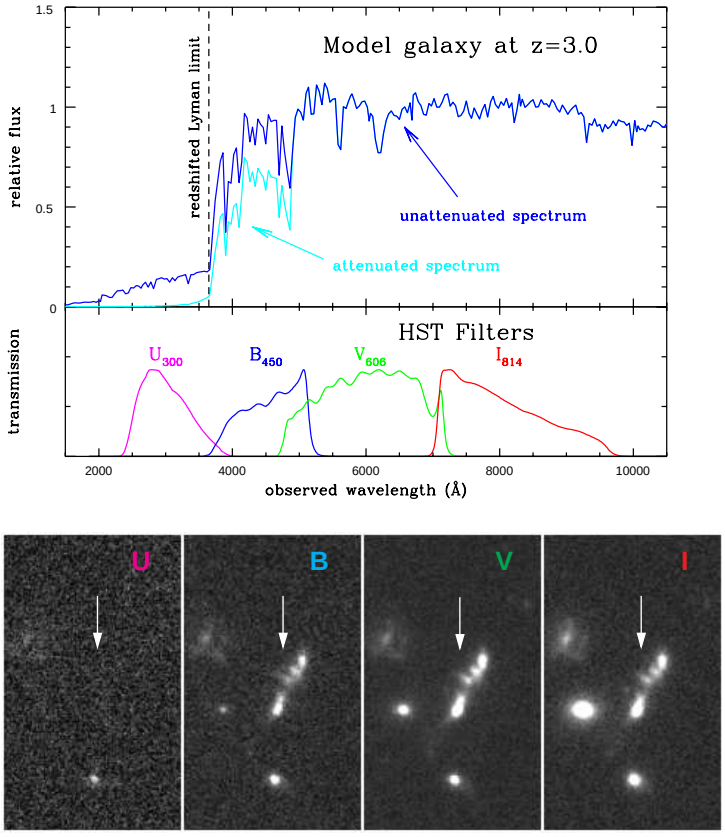

Figure 1.1: Illustration of the Lyman Break Galaxy technique at $z \sim 3$ (Dickinson 1998). The light emitted at wavelengths shorter than the lyman limit is absorbed by the neutral hydrogen in the IGM making the galaxy *dropout* of the U-band image. The subsequent redder filters (B, V, and I) show blue colors characteristic of a star forming galaxy. Using a similar set of filters but at longer wavelengths (for example a combination of the *HST* ACS and WFCR/IR filters), it is possible to search for galaxies at even higher redshifts. The highest redshift searches so far, involve sources that dropout of the WFC3/IR J_{110} filter ($\lambda_o \sim 1100$ Å). These galaxy candidates are expected to be at $z \sim 10$ but only one reliable candidate has been found so far (Oesch et al. 2012; and possibly another recent candidate behind a cluster, Zheng et al. 2012).

As described earlier, the technique takes advantage of the break observed between the Lyman limit and Lyα in the spectral energy distribution (SED) of star forming galaxies. A set of filters that samples the wavelength region across the break will show a very red color

followed by blue rest-frame UV colors at wavelengths longer than the break (see Figure 1.1). The population of star forming galaxies at the target redshift can be separated in the color-color space from the rest of the galaxy population, as shown in Figure 1.2.

To study the stellar populations and the stellar mass build-up of galaxies, the searches for LBGs in the field have several advantages over the previously mentioned Lyman-α emitter searches and the searches behind clusters. The main advantage is that the redshift window, or in other words, the search volume for a given color selection criterion is considerably larger than for Lyα emitters searches, resulting in larger samples. The sources identified through the LBG technique also generally have brighter stellar continuum fluxes in the UV and optical compared to the Lyα emitters (e.g., Cowie & Hu 1998, Steidel et al. 2000), which ensures that their stellar populations can be better studied (although some Lyα emitters have been detected in the rest-frame optical with *Spitzer*/IRAC, most are too faint to show significant detections either in the UV or the rest-frame optical). The contamination rates in a LBG search, can be estimated statistically without relying on spectroscopic confirmation of all sources. A small spectroscopic sample is in general required to validate the selection criteria. Compared to searches behind clusters, the effective volumes being probed in a LBG search are both larger and much more straightforwardly estimated since they do not depend on the challenging modeling of the magnification maps. This allows for much more precise estimates of the number densities (and subsequent stellar mass densities) and the luminosity function, for example.

The main shortcoming of the LBG technique is that it is only sensitive to galaxies that have significant UV fluxes, an indication of current high star formation activity. A population of passively evolving, or highly obscured sources, for example, would show much weaker Lyman breaks and could be missed by these searches. This is partially alleviated when the search is applied at the highest redshifts ($z \gtrsim 4$). The time span since the formation of the first stars and $z \sim 4$ corresponds to ~ 1.4 Gyr and it is much shorter at higher, redshifts (e.g., ~ 800 Myr at $z \sim 6$). This period is too short for a significant population of passive galaxies to have evolved

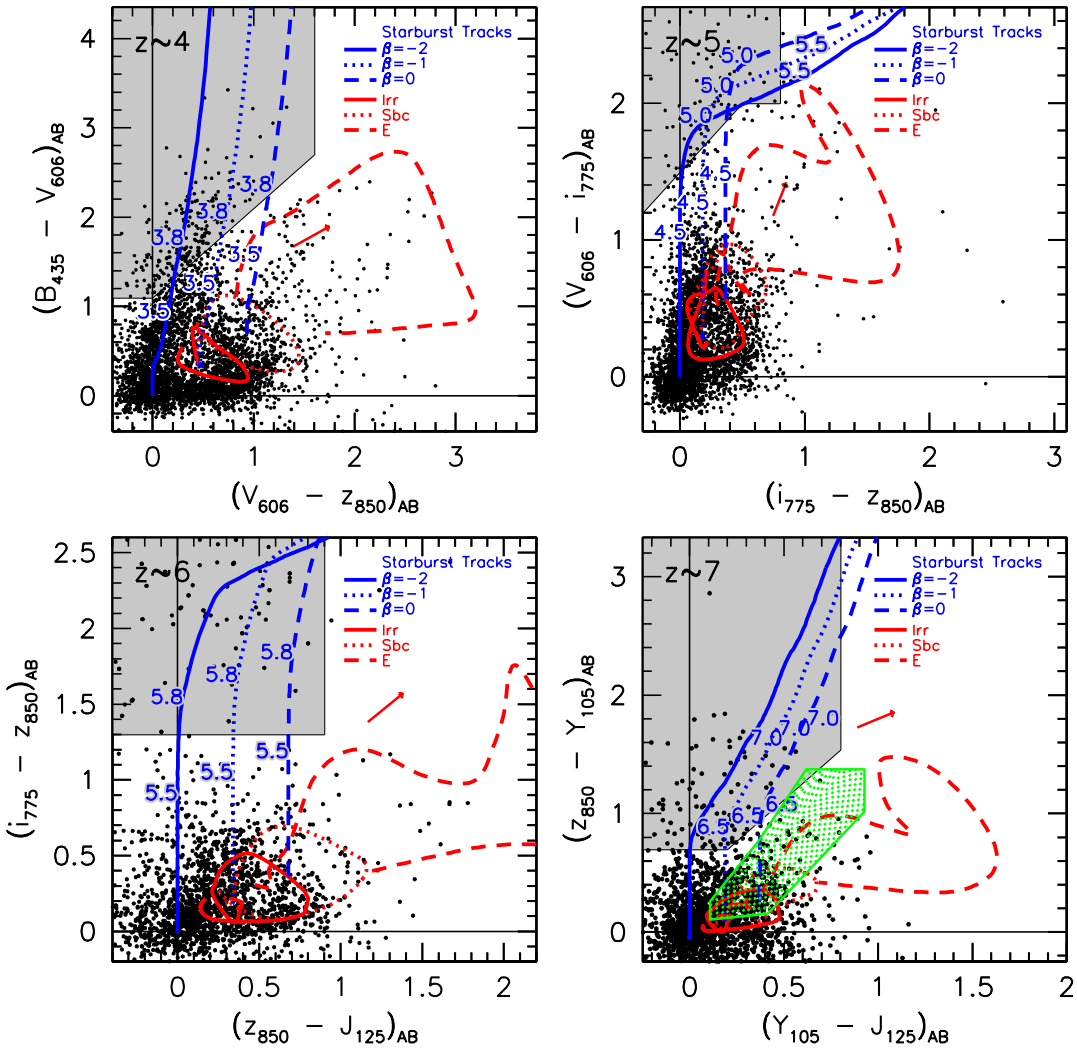

Figure 1.2: The color selection used in Bouwens et al. (2011b) to select galaxies at $z \sim 4$, 5, 6, and 7. The blue lines indicate the color evolution tracks of star forming galaxies as a function of redshift. A set of SEDs of star forming systems with varying UV slope β (defined by a a power law fit to the SED in the UV region: $f_\lambda \propto \lambda^\beta$) is considered. A two color criterion (based on very deep images and a set of filters from *HST* ACS and WFC/IR) it is possible to efficiently identify galaxies at the desired redshifts. As can be seen in the figures, the two color criterion is sufficient to isolate galaxies in the desired redshift range from the rest of the population (black dots). This includes low mass stars, as shown for example by the green area in the $z \sim 7$ panel.

to extremely faint UV fluxes (and contribute significantly to the stellar mass content of the Universe at the same time). It is also difficult to build large amounts of dust so quickly. To significantly obscure galaxies, large amounts of dust must be created in the short periods of time mentioned before. It seems, however, that this is not impossible, as some studies have shown the existence of extremely dusty galaxies at $z \sim 4$ (e.g., Michałowski et al. 2010). Far infrared studies have demonstrated the existence of sub-millimeter galaxies (SMGs) at redshifts as high as $z \sim 4 - 5$, exhibiting far-IR fluxes that suggest massive amounts of dust (Michałowski et al. 2010; and references therein). How these galaxies managed to form so much dust so quickly is still under investigation. In terms of studying the stellar mass assembly of the bulk of the population, however, this does not seem problematic, as these sources have been found to be extremely rare at early times.

The previous considerations make LBG searches the current best tool to study the formation and evolution of galaxies at early cosmic times. Even though it was first developed and tested to find candidate galaxies at $z \sim 2 - 3$, the principles, are easily extrapolated to the higher redshifts. The physical constraints from the age of the Universe and the intrinsic characteristics of the population at early times make the LBG technique a great tool to study the galaxy assembly at very high redshifts. The technical requirements for such searches at the most extreme redshifts (the current limit is at $z \sim 10$), however, are quite stringent, and application to the redshift range $4 < z < 8$ has only become possible recently thanks to technological advances. These advances include more sensitive cameras to detect the very faint fluxes of these galaxies and the development of better detectors and filters at the longer wavelengths. The most important of these advances have been the recent upgrades to the *Hubble Space Telescope* (*HST*), particularly the installation of the Wide Field Camera 3 (WFC3).

1.1.2 *Hubble Space Telescope* Upgrades

Since the first servicing mission (SM1) corrected the optical aberration in its primary mirror, *HST* has provided some of the most impressive observations of the Universe, captivating the imagination, not only of the astronomical community, but most interestingly the imagination of the general public, making it a flagship of the astronomical exploration. Furthermore, with each SM the observatory has seen remarkable upgrades that have each time pushed the frontier of galaxy exploration to higher redshfits. In particular, the installation of the *Advanced Camera for Surveys* (ACS) during SM3 caused a significant breakthrough in the exploration of the first 1.5 Gyr in the history of the Universe. A similar revolution that has allowed to push the envelope of the known galaxies in the Universe to $z \sim 10$ came more recently, during SM4, in which the WFC3/IR camera was installed.

SM3 was a two-part mission carried out in 1999 and 2002. During this mission the ACS camera was installed. The large field of view (FOV, $202'' \times 202''$), great sensitivity, and a set of filters that reached to 0.85μm (the z_{850} filter is centered at $\sim 0.85\mu$m), permitted highly efficient searches for LBGs at $z \sim 4-6$ and allowed the study of the very faint population of galaxies at these redshifts. Moreover, it was possible to combine this very efficient instrument with the *Near Infrared Camera and Multi-Object Spectrograph* (NICMOS) that provided wavelength coverage at longer wavelengths, to $\sim 1.6\mu$m (although with poorer sensitivity and smaller FOV). This combination permitted the first extensive search for $z \sim 7$ galaxy candidates. The most complete of such samples of $z \sim 7$ candidates using these two instruments (ACS and NICMOS) is the subject of study in Chapter 2.

The bulk of this thesis, however, is based on data obtained after the latest upgrade to *HST*. Carried out in May 2009 after years of delays and heated discussion to fund and authorize the execution of the project, SM4 was successfully completed. It involved the repair of ACS (which had failed not long before the launch of SM4) and the installation of the Wide Field

Camera 3 (WFC3). This high sensitivity camera is equipped with a set near infra-red (NIR) filters (reaching 1.6μm) that can replace the old NICMOS filters and is 40$\times$ more efficient. This allows efficient LBG searches at $z \sim 7-10$ (that is 500-700 Myr after the Big-Bang) and, very importantly, a much more detailed study of the UV light of galaxies at $z \sim 4$ over a wide wavelength range that covers the near and far UV (from Lyα to the 4000Å break).

These significant improvements in instrumentation have allowed a great progress in our understanding of the rest-frame UV properties of galaxies in the early Universe. Because the light at these wavelengths is a good tracer of the star formation rate, it has also provided the first information about the stellar mass assembly from very early times.

1.2 The UV Luminosity Function at $z > 4$ and the Star Formation Rate Density

The luminosity function (LF) is one of the most fundamental quantities that can be derived for a galaxy population. This function is a measure of the abundance of sources as a function of luminosity. Ideally, it is measured in the rest-frame optical, because the fluxes are more robust to changes in age and dust content than in the UV, where large variations can be observed in $10-100$ Myr periods. As mentioned before this is not feasible at $z > 4$, and so our best determinations of the LF are in the UV.

Even though it may be less stable than an optical LF, the UV LF has some interesting and important properties. The rest-frame far-UV light probed by the *HST* observations of galaxies at $z > 4$ is produced by very massive O and B stars. Since these stars have short lives (> 10 Myr), the flux measured at this wavelength is a good indicator of very recent star formation. In fact, for a variety of star formation histories, a similar conversion can be inferred between the UV flux and the recent star formation rate (Madau et al. 1998; the most common of such relations used in the literature). The UV LF, then, is a measurement of how the star

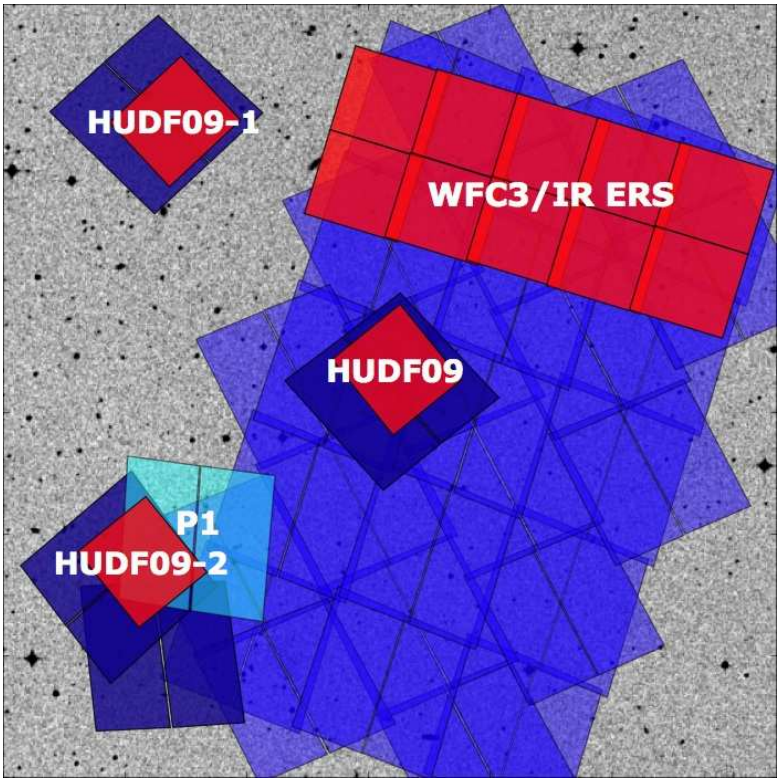

Figure 1.3: Deep *HST* fields in the CDF South (Bouwens et al. 2011c). The red regions indicate some of the latest WFC3/IR observations (the HUDF and the two parallels and the ERS field). The blue corresponds to ACS observations. These fields have allowed good determinations of the UV LF at $z \sim 4-8$ over a luminosity range that spans from $M_{1600,\mathrm{AB}} \sim -21$ to $M_{1600,\mathrm{AB}} \sim -16$ at $z \sim 4$. These fields have also been observed with *Spitzer*/IRAC, which allows for the study of the stellar populations and stellar masses of the galaxies found in these fields.

formation activity is distributed in the population (see, for example, the SFR functions derived by Smit et al. 2012 at $z \sim 4-7$). The integral of these UV LFs corresponds to the total star formation rate density (SFRD) of the Universe (proper corrections for dust extinction need to be considered).

To construct the UV LFs and be able to constrain their shapes properly, it is important to obtain samples over a large luminosity range. This has been done via a combination of deep fields like those from the GOODS program (Giavalisco et al. 2004), and ultra-deep fields like the HUDF, which is ideally suited to study the faint population. In addition, shallow searches over large areas from ground based surveys can provide valuable constrains to the abundance

of bright galaxies (e.g., Castellano et al. 2010b), which are rare and require large areas to be found in sizable numbers. Most of this thesis is based on the *HST* fields that have recently been observed with the WFC3/IR camera and that have *Spitzer*/IRAC imaging. The main fields are shown in Figure 1.3.

Based on the observations from fields like the ones shown in Figure 1.3, the UV LF has been determined to impressive precision at $z \sim 4-8$ (e.g., Bouwens et al. 2011c; see Figure 1.4). One of the main lessons obtained from these LFs is that the overall UV luminosity of the population of galaxies (and hence its SFR) has been steadily increasing since at least $z \sim 8$, with strong indications that this evolution was even stronger from $z \sim 10$ to $z \sim 8$ (Oesch et al. 2012).

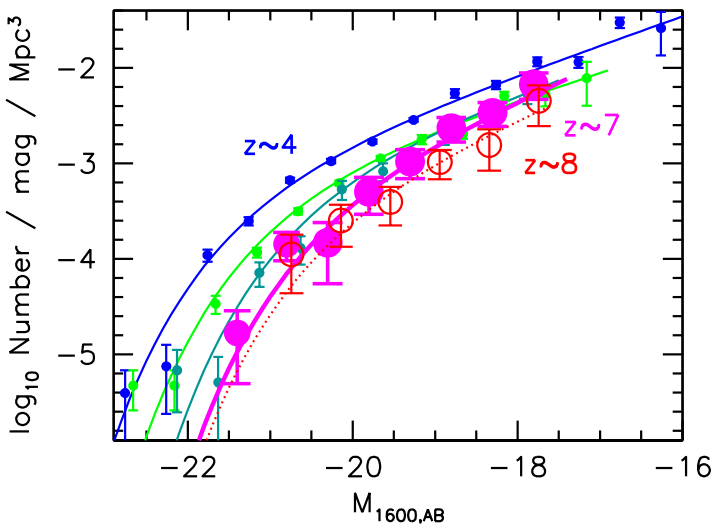

Figure 1.4: Latest determinations of the UV Luminosity functions at $z \sim 4,\ 5,\ 6,\ 7$ and 8 from Bouwens et al. (2011c). These LFs show a steady increase in the average UV luminosity of the population (and hence the SFR) as a function of cosmic time.

These studies have also suggested that the faint end slope of the UV LF, may become steeper as a function of increasing redshift. This suggests the abundant existence of very faint sources that are beyond the limits of current surveys (e.g., Bouwens et al. 2007, Oesch et al. 2010a).

Another very interesting result comes from the integral of the UV LFs. The UV luminosity density as a function of redshift shows a rapid increase with cosmic time (when a luminosity cut is imposed, see Figure 1.5). This translates in a rapid increase in the SFRD of the Universe which corresponds to about an order of magnitude change between $z \sim 8$ and $z \sim 3$ (near the cosmic maximum). A subsequent factor $10\times$ decline in the SFRD is observed from $z \sim 3$ to $z \sim 0$. The increase at high redshift, however, occurs over a much shorter timescale of $\sim 1.5\,\mathrm{Gyr}$ (compared to $\sim 11\,\mathrm{Gyr}$ in the decline to $z \sim 0$).

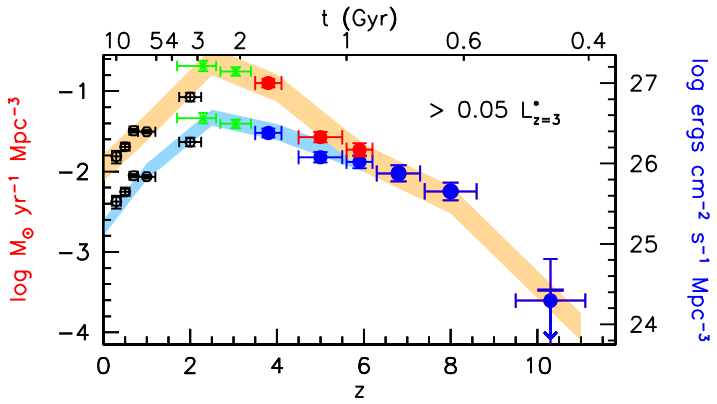

Figure 1.5: Star formation rate density of the Universe as a function of redshift derived from the UV luminosity of LBGs (corrected for dust extinction: red, and without corrections: blue; Bouwens et al. 2011c). A very rapid increase by a factor $10\times$ in the SFRD is observed from $z \sim 8$ to $z \sim 3$. This frenetic pace in the galaxy assembly process is significantly slowed down at later times ($z < 3$).

The evolution of the SFRD indicates that galaxies assembled their stellar masses and started forming their structures at a very rapid pace shortly after the Big Bang. This growing frenzy has slowed down significantly at later times ($z < 3$). The high redshift Universe, then, is an epoch of rapid assembly in which evolution happens at an accelerated rate. It is then very interesting to see how this rapid evolution is reflected on the properties of the galaxies. In particular, it is very important to corroborate that the stellar mass content of these galaxies (and the stellar mass density of the Universe) does in fact grow as would be predicted from the evolution of the SFRD. Studying the stellar mass and stellar populations of $z > 4$ galaxies

requires access to longer wavelengths than are accessible with *HST*. This type of study represents the core of this thesis.

1.3 Studying the Stellar Population of High-z Galaxies and the Stellar Mass Determinations

The great quality of the *HST* data not only has allowed us to find very distant LBGs, it has also given us important information about their SFRs and, in consequence, about their stellar mass assembly history. The previously mentioned studies are based solely on the light emitted by the most massive stars in these galaxies, and in consequence, represent a study of a transient property that could change in timescales of 10-100 Myr. It is desirable then to study the less massive stars that live longer and can provide information about cumulative properties of these galaxies (in particular we are interested in the stellar mass), but they emit the bulk of their light at wavelengths $\lambda_{\rm rest} > 4000\,$Å. Ideally we would like to observe these galaxies at $\lambda_{\rm rest} \sim 2\,\mu$m to have the most reliable estimate of their stellar masses. The study of this light at $z \sim 4$ requires observations far in the infrared (and redward at higher redshifts). This wavelength range is not accessible today with current telescopes and instrumentation.

Deriving stellar masses from UV fluxes only has huge uncertainties associated ($>$ 1.8 dex, Papovich et al. 2001, Labbé et al. 2010a). Even though the rest-frame K band is inaccessible, great improvement can be achieved in determining this quantity if fluxes at wavelengths $\lambda_{\rm rest} > 4000\,$Å is included in the stellar population modeling. There is today only one instrument that can efficiently provide such data for the studies of galaxies at $z \gtrsim 4$: the *Spitzer Space Telescope*, in particular with the used of the *Infra-Red Array Camera* (IRAC).

The *Spitzer*/IRAC camera has a large FOV (5.2'×5.2') and is quite sensitive, making it ideal to study rare and faint high-z galaxies. The main shortcoming of this instrument is the fairly large size of its point spread function (PSF), which is much larger than that of the *HST*

observations (i.e., $\sim 2''$ vs. $\sim 0''.1$). This limits its effectiveness for studying small faint sources in long integrations because the PSF creates crowding issues, making it difficult to obtain reliable fluxes in the rest frame optical of $z > 4$ galaxies (we will describe throughout the thesis how we have minimized this problem). As a consequence, most previous studies that combine deep *HST* LBG samples and *Spitzer*/IRAC measurements of the rest-frame optical light at $z \gtrsim 4$ have relied on small samples of galaxies that are fairly isolated in the projected sky (to avoid flux confusion created by crowding).

1.3.1 The UV-to-optical Colors of High-z LBGs

The earliest studies to exploit the capabilities of the IRAC camera at $z > 4$ proved that it was possible to learn about the stellar populations of these galaxies. This has generally been done by fitting synthetic stellar population models (e.g., the Bruzual and Charlot 2003 models, or the models by Maraston et al. 2005) to the observed SEDs (see Figure 1.6). By fitting the total fluxes observed and assuming an initial mass function (IMF, a commonly used one is the Salpeter 1955), the stellar masses of these galaxies can be estimated. The IMF assumption is necessary because, as mentioned earlier, the observations only detect the light from the most massive stars so an extrapolation is necessary to determine the contribution of the lower mass stars (actually, the *lowest* mass stars play a dominant role in the stellar mass content of galaxies).

Some of the earliest results from such studies were fairly surprising. The UV-to-optical colors measured for LBGs at redshifts as high as 6 showed indications of significant 4000 Å breaks, typically $\gtrsim 0.5$ mag. This feature is generally understood as a good indicator of the age of a stellar population. The exact ages estimated depend on the exact star formation history (SFH) of the galaxy (which is a great unknown) but for the typical assumptions (exponentially declining or constant SFH), the observed colors indicate ages of ~ 500 Myr (Yan et al. 2005; 2006, Eyles et al. 2005; 2007, Labbé et al. 2006, Egami et al. 2005). This is a significant fraction of the age of the Universe at the high redshifts been studied here (~ 900 Myr at $z \sim 6$). Even though age

is one of the most uncertain quantities that can be estimated based on SED data, this provides a strong indication that these galaxies have been forming stars for a very long period of time that is comparable to the age of the Universe at the time of observation. This opened the possibility that we could constrain the stellar mass assembly of galaxies at times that are much closer to the Big Bang, beyond those galaxies that we could directly detect.

Moreover, using the stellar population modeling techniques described before, the stellar masses were estimated for galaxies at redshift as high as 7 (Egami et al. 2005, Labbé et al. 2006). The stellar mass estimates for these galaxies indicated stellar mass contents as high as $\gtrsim 10^{10} M_{\odot}$. In combination with the estimated ages, these results indicated that the star formation activity had been quite intense even at very early times.

Although samples were small and the data somewhat limited, it was also possible to use these samples and the stellar mass estimates for individual galaxies to make the first estimates of the stellar mass density of the Universe at $z \gtrsim 4$. The UV studies of the SFRD suggested a rapid increase in the star formation activity, and it was expected that the accumulated mass should show that. In fact these early studies already showed a very rapid increase in the stellar mass content of the Universe (e.g., Eyles et al. 2007), supporting a picture of a rapid early development in the baryonic content of galaxies.

Results like these previously mentioned were derived from small samples and only for bright isolated sources that were amenable to *Spitzer*/IRAC observations. They were also limited generally to one redshift selection. It was interesting then to systematically explore the evolution of the stellar mass content and of the properties of these galaxies as a function of cosmic time. A first comprehensive work to perform such study was the excellent work of Stark et al. (2009).

Stark et al. (2009) studied the properties of a large number of LBGs found over the two GOODS fields in the $z \sim 4 - 6$ redshift range. Combining *HST* imaging from ACS and *Spitzer*/IRAC from the GOODS program, they were able study the stellar populations (based

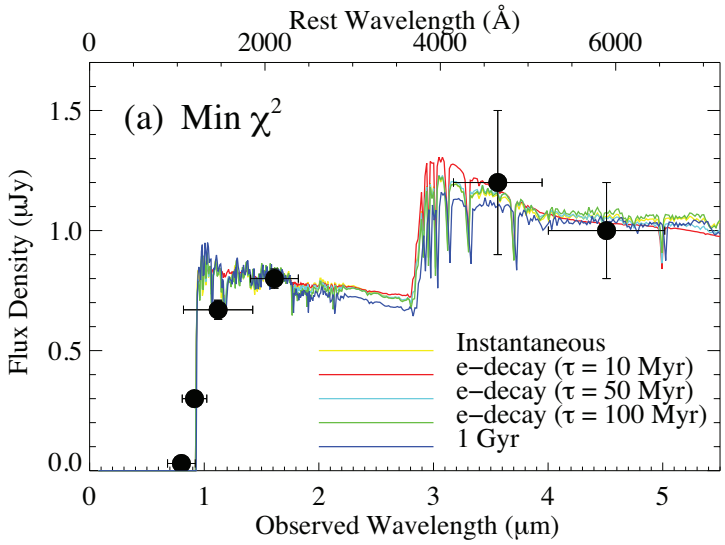

Figure 1.6: Example of a high-z (best estimate $z \sim 6.6-6.9$) LBG with *Spitzer*/IRAC detection. This is one of the earliest examples of a $z \sim 7$ candidate (Egami et al. 2005). The IRAC detection allows for reliable stellar mass estimates for this source, wich corresponds to $\sim 10^9 M_\odot$ (Egami et al. 2005). This is a remarkable amount of mass, considering that the Unverse is only 750 Myr old at $z \sim 7$, which indicates that this galaxy was intensely forming stars at earlier times.

on rest-frame UV and optical observations) of galaxies over the period from $\sim$ 900 Myr to $\sim$ 1.5 Gyr after the Big Bang. This study showed that the previously mentioned $\sim$ 0.5 mag color across the Balmer break is a typical feature of high-z LBGs. In fact, they showed a fairly tight correlation between the rest-frame UV fluxes and the rest-frame optical fluxes of these galaxies and that this correlation is observed, apparently unchanged in this period of time (from $z \sim 6$ to $z \sim 4$). Since the colors observed seem to be fairly constant as a function of redshift, the ages, and other properties derived through SED fitting seem also fairly constant with redshift. This is a very interesting result that could teach us about the mode of evolution that galaxies present in the early Universe. Stark et al. (2009), for example, interpret the constant age derived through SED fitting as evidence that the LBGs in their samples have low duty cycles and that they are generally included in the samples only in the periods when they are actively forming stars (and missed from the samples otherwise – for constraints on the duty cycle based on clustering see, for example, Lee et al. 2006, Lee 2007).

The advent of the WFC3/IR camera on *HST* has opened the opportunity to significantly improve on systematic studies of galaxy evolution at early times like the Stark et al. (2009) work. It is now possible to obtain much larger samples of galaxies at the adequate redshifts, extending their study to very fainter luminosities, and with better coverage of the UV region of the SED at $z \gtrsim 4$. Most remarkably, it has been possible to extend the studies of the properties of LBGs to redshifts reaching $z \sim 7$ and 8 (600 Myr after the Big Bang). This has in fact been one of the major developments in the thesis presented here. As will be shown in the following chapters, this thesis represents the most complete exploration to date of the observed properties of galaxies in the first 1.5 Gyr in the history of the Universe. It includes detailed stellar population modeling of the very faint population observed (relying on stacked SEDs to push to the faintest possible luminosities), a systematic study of the evolution of the stellar mass function down to very low masses and of the stellar mass content of the Universe and its comparison to the expectations from the SFRD determinations from the UV studies. It also addresses several caveats and explores the effects of phenomena that cannot be directly constrained today, for example, the possibility of very strong rest-frame optical emission lines in high-z galaxies and their likely effect on the results derived throughout.

We present now an outline of the contents of this thesis.

1.4 Outline

This thesis contains previously published material and material that is in the process of being revised for publication at the time of this writing. In Chapter 2, published as "The Stellar Mass Density and Specific Star Formation Rate of the Universe at $z \sim 7$", Gonzalez, V., Labbé, I., Bouwens, R., Illingworth, G., Franx, M., Kriek, M., and Brammer, G. 2010, ApJ 713, 115; we study one of the earliest samples of galaxies at $z \sim 7$ in the pre-WFC3/IR era. It combines observations with *HST* ACS and NICMOS and *Spitzer*/IRAC which is used throughout this

thesis. This chapter includes one of the earliest determinations of the stellar mass density of the Universe at $z \sim 7$ and presents a theoretical challenge that is sometimes referred to as the *Specific Star Formation Rate Plateau* and that has motivated a series of theoretical works that try to explain these observations.

Chapter 3 has been published as "Star formation rates and stellar masses of $z \sim 7-8$ galaxies from IRAC observations of the WFC/IR ERS and HUDF fields", Labbé, I., Gonzalez, V., Bouwens, R., Illingworth, G., Franx, M., Trenti, M., Oesch, P., van Dokkum, P., Stiavelli, M., Carollo, M., Kriek, M., Magee, D. 2010, ApJ Letters 716, 103L. It presents a first large sample of 36 $z \sim 7$ sources, and the first rest-frame optical detection of $z \sim 8$ galaxies. The stellar mass vs. SFR relation is studied at $z \sim 7$ and the stacked SEDs as a function of luminosity. The first author of this work was Ivo Labbé. V. G. did much of the analysis of the *Spitzer*/IRAC data on these galaxies, and the results from this work are combined with lower redshift sample in later chapters.

Chapter 4, published as "Evolution of Galaxy Stellar Mass Functions, Mass Densities, and Mass to Light ratios from $z \sim 7$ to $z \sim 4$", Gonzalez, V., Labbé, I., Bouwens, R., Illingworth, G., Franx, M., Kriek, M. 2011, ApJ Letters 735,L34; is a detailed study of the Stellar Masses of $z \sim 4-7$ sources. In particular, it studies the stellar masses as a function of UV-luminosity down to very faint luminosities, relying on stacking of faint IRAC sources to derive a robust relation. This relation is combined with the UV LFs at these redshifts to estimate the Stellar Mass Functions at $z \sim 4-7$. These stellar mass functions include estimates for incompleteness corrections at very low masses. This study also presents the stellar mass density evolution of the Universe since $z \sim 8$ both for luminosity limited samples and also an estimate for a mass limited sample based on the stellar mass vs. UV luminosity relation derived.

Chapter 5, which was submitted for publication as "The Rest Frame UV to Optical Colors and SEDs of $z \sim 4-7$ Galaxies", Gonzalez, V., Bouwens, R., Labbé, I., Illingworth, G., Oesch, P., Franx, M., and Magee, D. 2011 (submitted to ApJ) arXiv:1110.6441; is a further

exploration of the SEDs of very faint high-z galaxies. To study the very faint population at reasonable signal-to-noise, this work relies on a stacking analysis. This work explores the different color trends observed as a function of redshift and luminosity. The optical colors observed in the stacked SEDs strongly suggest the presence of emission line contribution to the rest-frame optical fluxes measured with IRAC.

Chapter 6, revisits one of the most important results presented in Chapter 2, the sSFR as a function of redshift and its apparent *plateau* at $z \gtrsim 2$. It takes advantage of the most recent progress in our understanding of the properties of galaxies at $z > 4$. This includes studying the effects of a rising star formation history (supported observationally and theoretically), and the probable evolution of the dust content of galaxies as a function of redshift and luminosity. This work also explores the likely effects of emission lines in the estimated evolution of the sSFR with redshift. This Chapter will be submitted for publication to the Astrophysical Journal.

A summary and some final remarks are presented in Chapter 7.

Chapter 2

The Stellar Mass Density and Specific Star Formation Rate of the Universe at $z \sim 7$

2.1 Introduction

Direct observations of galaxies at high redshift from complete, well-defined searches place strong constraints on galaxy formation and evolution models. Extensive studies have been made of galaxies selected by the dropout technique out to redshift 6 (see e.g., Stanway et al. 2003, Bunker et al. 2004, Yan & Windhorst 2004, Bouwens et al. 2006; 2007, McLure et al. 2009) thanks in part to the capabilities of the *HST*/ACS and NICMOS cameras. Studies at higher redshifts, however, have been much more challenging. In particular, one of the key issues has been the derivation of stellar masses. These masses can provide both strong additional constraints on formation models and information about the star formation rates at even earlier times, effectively opening a window towards the earliest phases of galaxy formation. Deriving

masses at higher redshifts does however face some distinct challenges.

At redshifts $z > 4$, ACS and NICMOS only access the rest-frame UV continuum, which is not a reliable tracer of stellar mass. To obtain better constraints on this quantity through SED fits it is necessary to extend the observations to the rest-frame optical. Although *Spitzer* data present challenges due to the large instrumental PSF, these rest-frame optical measurements can be made at high redshifts with the 3.6 μm and 4.5 μm IR channels of the IRAC camera (Fazio et al. 2004). The IRAC 3.6 μm and 4.5 μm bands probe the rest-frame optical fluxes around $0.5-0.6$ μm of $z \sim 5+$ sources and reach to $\gtrsim$26 AB mag at 5σ in deep $\gtrsim$23 hr integrations. This is a remarkable achievement for a 0.8-m telescope. *Spitzer* data will continue to play a unique role in the determination of fundamental properties like ages and stellar masses of the earliest galaxies until JWST is launched. These *Spitzer* and *HST* data have permitted estimates of stellar masses for large numbers ($\gtrsim$150) of z ~5-6 sources (Yan et al. 2005; 2006, Eyles et al. 2005, Egami et al. 2005, Stark et al. 2009, Mobasher et al. 2005, Bradley et al. 2008, Zheng et al. 2009). One surprising early finding was the number of quite massive $\sim 10^{10}$ $M_{\odot}$ galaxies in $z \sim 6$ samples (e.g., Yan et al. 2005, Eyles et al. 2005). It suggested that $z \sim 5-6$ galaxies experienced substantial amounts of star formation at much higher redshifts and earlier times, well into the epoch of reionization (Stark et al. 2007a, Yan et al. 2006).

These analyses have also opened the possibility of looking at the SFR-Mass relation at higher redshifts, or equivalently, at the specific SFR or sSFR (i.e., SFR/Mass). The sSFR tells us how fast galaxies are growing with respect to their current stellar masses. While at low redshifts ($0 < z < 1$) it has been shown that galaxies grew faster in earlier times than they do today (Noeske et al. 2007), it has been suggested that at higher redshift ($4 < z < 6$) the SFR-Mass relation remains much more constant (Stark et al. 2009). This transition in the sSFR is an interesting and important result and needs to be assessed over a long redshift baseline.

It is imperative then to try to extend these studies to $z \geq 7$ and investigate what are the characteristics of the probable progenitors of these rather massive $z \sim 6$ sources. Doing

so, however, has been challenging due to the difficulty in obtaining deep enough near-IR and optical data to robustly identify $z \sim 7$ sources. Such sources only start to become "common" at $\gtrsim$26.5 AB mag. Thus, early selections of $z \sim 7$ z-dropouts from the HUDF included only a handful of candidates, and the situation has only improved slowly (Bouwens et al. 2004b; 2008, Oesch et al. 2009). Consequently, very little has been published on the stellar masses of $z \sim 7$ z-dropout galaxies (Egami et al. 2005, Labbé et al. 2006). Labbé et al. (2006) performed stellar population modeling of four ACS z_{850}-band dropout sources found in the HUDF and derived stellar masses of $\sim 10^9 - 10^{10}$ $M_\odot$, ages of $\sim 100 - 200$ Myr, and was able to estimate a stellar mass density (SMD) of 1.6×10^6 $M_\odot$ Mpc^{-3} (to $0.3L^*_{z=3}$).

Fortunately, as a result of continued efforts to select $z \sim 7$ galaxies from the growing quantity of deep near-IR NICMOS data, Bouwens et al. (2010a) have succeeded in substantially expanding the size of current $z \sim 7$ z-dropout selections, and now 14 NICMOS-selected, rather luminous $z \sim 7$ z-dropout galaxies are known that are amenable to stellar mass estimates. The recent advent of WFC3 on*HST* has expanded the number of known $z \sim 7$ sources and now $\sim$25 sources are known at $z \sim 7$ (Oesch et al. 2010b, Bouwens et al. 2010b, McLure et al. 2010, Bunker et al. 2010, Castellano et al. 2010a, Yan et al. 2010, Ouchi et al. 2009, Hickey et al. 2010, Wilkins et al. 2010). Most of the newly discovered galaxies, however, are too faint to attempt stellar mass estimations on individual basis, although valuable information can be obtained from these samples through stacking analysis (see Labbé et al. 2010b[1]). Galaxies in the Bouwens et al. (2010a) sample extend from $\sim$25.5 AB mag to $\sim$27.8 AB mag (rest-frame 1500 Å) and are found in the HUDF and in and around the two wide-area GOODS fields. These candidates also possess very deep $\gtrsim$23.3 hr coverage with IRAC from the *Spitzer* GOODS program and present us with a unique opportunity to better understand what the typical properties (ages, stellar masses) of $z \sim 7$ z-dropouts are.

[1]The Labbé et al. (2010b) work focuses exclusively on the ultrafaint, sub-L* sources. Only sources UDF-387-1125 and UDF-3244-4727 from this work (our faintest $z_{850}-$dropouts in the UDF) are also included in Labbé et al. (2010b).

Here we take advantage of the larger sample of 15 z_{850}-dropout sources identified by Bouwens et al. (2010a) to estimate the typical properties of $z \sim 7$ galaxies. The much larger size of current samples allows us to get a better handle on the typical properties of $z \sim 7$ galaxies than was possible from the smaller and brighter samples previously available (Labbé et al. 2006). For example, sizeable variations in the M/L ratios of individual galaxies can considerably skew the averages for the population as a whole. The present sample also includes galaxies from two independent lines of sight, i.e., the HDF-North GOODS and CDF-South GOODS, so the results should be less impacted by cosmic variance. In estimating rest-frame optical fluxes for our $z \sim 7$ candidates from the IRAC, we will take advantage of the well-tested deblending process described by Labbé et al. 2006 (see also Wuyts et al. 2007) which enables us to estimate fluxes even when there is moderate overlap with nearby sources. This also allows for a larger sample, since the well-known problems with blending and confusion in IRAC data have limited previous studies.

We provide a brief outline for this paper here. We present the sample selection and observational data we have used in this work in Section 2.2 and Section 2.3 respectively. In Section 2.4, we will describe the photometry of the sample with particular emphasis in the deblended photometry from the IRAC channels. We devote Section 2.5 to a discussion of the photometric redshifts obtained and possible contamination and in Section 2.6 we present the procedure and results in the process of fitting synthetic stellar populations to the observed SEDs (including our sSFR results). Section 2.7 presents our estimated SMD at $z \sim 7$ and confidence intervals. We compare our results to previous work in Section 2.8 and present a discussion of them in Section 2.9. We summarize our conclusions in Section 2.10. All magnitudes quoted in the paper are in the AB system (Oke & Gunn 1983). We have used cosmological parameters $\Omega_\Lambda = 0.7, \Omega_M = 0.3$ and $H_0 = 70$ kms s^{-1} Mpc^{-1} to facilitate comparison to previous works.

2.2 Sample Selection

The present selection of $z \sim 7$ z-dropout candidates is based upon ~ 80 arcmin^2 of very deep optical ACS, near-IR NICMOS, and IRAC data available over and around the two GOODS fields – including the HUDF and HDF-North (see Section 2.3 for a more detailed description of these data). This selection is described in Bouwens et al. (2010a).

Candidate $z \sim 7$ galaxies were required to satisfy a two-color Lyman-Break Galaxy (LBG) criterion adapted to $z \sim 7$ – showing a strong $z - J$ break but possessing a blue $J - H$ color (redward of the break). In detail, the color criterion used is:

$$(z_{850} - J_{110})_{\rm AB} > 0.8$$

$$\wedge\ (z_{850} - J_{110})_{\rm AB} > 0.8 + 0.4(J_{110} - H_{160})_{\rm AB},$$

where $\wedge$ represents the logical **AND** operation and where the colors were measured in a $\sim 0\farcs4$-diameter aperture using *SExtractor* in double image mode with the H_{160} band image being the detection image. Candidate $z \gtrsim 7$ sources were also required to be undetected to better than 2σ in the optical ACS bands (B_{435}, V_{606}, and i_{775}). Sources were also removed from the sample if they were detected at 1.5σ in two or more of the optical bands. Only detections of at least 5σ in the H_{160}-band images (measured in apertures of $0\farcs6$ in diameter) were considered to ensure that candidates correspond to real sources. The candidates –with GNS IDs– were also required to have have ($H_{160}-$[5.8] μm) colors bluer than 2.5 ([5.8] μm photometry measured in $2''$-diameter apertures). This provided added confidence that the sources were not low-redshift interlopers.

By applying the above criteria to $\sim$80 arcmin^2 of deep NICMOS data, Bouwens et al. (2010a) identified 15 $z \sim 7$ z-dropout candidates (see Table 2.2). The candidates range in $H_{160,AB}$ magnitude from 25.5 to 27.6 AB mag and are typically only marginally resolved at NICMOS/NIC3 resolution (FWHM of the PSF is $\sim 0\farcs37$). Contamination rates for the sample are determined by running a number of photometric scattering simulations on a fake sample

of low redshift sources. This sample is constructed to match the color distribution of observed galaxies in the 24.5 $<H_{160}<$ 26 range. We have added noise to the fluxes in each individual band according to the depths of the different fields. By applying the selection criteria previously described, we characterize when and with what frequency low-redshift contaminants enter our selection. A more detailed discussion of the procedure is given in Bouwens et al. (2008) and Bouwens et al. (2010a). Through this technique we find that the contamination for the sample (by lower redshift galaxies, time-variable sources, low-mass stars, for example) is expected to be just $\sim$ 10% of the sample for sources found over the HUDF and HUDF05 fields, and only $\sim$ 20% for sources within the GOODS fields.

We only use those 11 z-dropout candidates from the Bouwens et al. (2010a) selection that have deep (23+ hr) IRAC data in both 3.6 and 4.5 μm and which were in the Bouwens et al. (2010a) z-dropout sample as of 2009 June.

2.3 Observational Data

The very deep optical, near-IR, and mid-IR IRAC data available for our z $\sim$7 z-dropout candidates permit us to study the properties of these sources in detail. A summary of the available imaging data for the candidates we have in our various search fields is given in Table 2.1.

The deep near-IR data we have available for our candidates at $\sim$1.1 μm and $\sim$1.6 μm come from NICMOS. For the candidates within the GOODS fields, the NICMOS data reach to depths of $\sim$26.8 AB mag and $\sim$26.7 AB mag (5σ, aperture flux within a $0\farcs6-$diameter, used for detection) in the J_{110} and H_{160} bands, respectively. For purposes of SED fitting we use a larger ($0\farcs9-$diameter) aperture to minimize differences in the aperture corrections among the optical, NIR and mid-IR images. The 1σ limits relevant for the SED fitting are $\sim$ 27.8 and $\sim$ 27.9 AB mag (J_{110} and H_{160} bands, corrected to total fluxes using aperture corrections of $\sim$ 20% derived

from stellar profiles). The near-IR data over the HUDF reach some ~ 0.5 AB mag deeper. The FWHM of the NICMOS PSF is $0\farcs34$ and $0\farcs37$ in the J_{110} and H_{160} bands, respectively.

We also have very deep $\sim$2.2 μm K-band data available for our $z \sim 7$ z-dropout candidates over the HUDF and in the central region of the HDF-North. These data are particularly valuable for providing a constraint on the UV-continuum slopes. The K-band data over the

Table 2.1: Summary of Available Data

Filter	Depth $[1\sigma]$	Reference
HUDF		
ACS - B_{435}	29.9	[1]
ACS - V_{606}	30.4	[1]
ACS - i_{775}	29.9	[1]
ACS - z_{850}	29.4	[1]
NICMOS - J_{110}	28.7	[5, 6]
NICMOS - H_{160}	28.3	[5, 6]
ISAAC - K_s	27.3	[11]
IRAC - 3.6μm	27.5	[15]
IRAC - 4.5μm	26.8	[15]
IRAC - 5.8μm	25.8	[15]
IRAC - 8.0μm	25.7	[15]
GOODS South		
ACS - B_{435}	28.8	[2, 3]
ACS - V_{606}	29.1	[2, 3]
ACS - i_{775}	28.5	[2, 3]
ACS - z_{850}	28.3	[2, 3]
NICMOS - J_{110}	28.0	[7, 8]
NICMOS - H_{160}	27.9	[7, 8]
IRAC - 3.6μm	27.2	[15]
IRAC - 4.5μm	26.4	[15]
IRAC - 5.8μm	25.4	[15]
IRAC - 8.0μm	25.3	[15]
GOODS North		
ACS - B_{435}	28.7	[2, 3]
ACS - V_{606}	29.0	[2, 3]
ACS - i_{775}	28.6	[2, 3]
ACS - z_{850}	28.5	[2, 3]
NICMOS - J_{110}	27.8	[7, 8]
NICMOS - H_{160}	27.7	[7, 8]
MOIRCS - J_s	27.1[a]	[12, 13, 14]
MOIRCS - K_s	27.4[a]	[12, 13, 14]
IRAC - 3.6μm	27.2	[15]
IRAC - 4.5μm	26.4	[15]
IRAC - 5.8μm	25.4	[15]
IRAC - 8.0μm	25.3	[15]

Summary of available data (continued)

Filter	Depth $[1\sigma]$	Reference
	HDFN[b]	
ACS - B_{435}	29.2	[2, 3]
WFPC2 - B'_{450}	30.2	[4]
ACS - V_{606}	29.4	[2, 3]
WFPC2 - v'_{606}	29.0	[4]
ACS - i_{775}	28.6	[2, 3]
WFPC2 - I_{814}	28.8	[4]
ACS - z_{850}	28.23	[2, 3]
NICMOS - J_{110}	27.9	[9, 10]
NICMOS - H_{160}	28.1	[9, 10]
MOIRCS - K_s	27.6	[12, 13, 14]
IRAC - $3.6\mu m$	26.8	[15]
IRAC - $4.5\mu m$	26.2	[15]
IRAC - $5.8\mu m$	25.8	[15]
IRAC - $8.0\mu m$	25.7	[15]

Notes. The depths of the data in the different fields. Optical to NIR were estimated using $0\farcs9$ diameter apertures and corrected to total assuming stellar profiles (aperture corrections of 5% and 20% for the ACS and NICMOS data respectively). Apertures of $1\farcs8$ were dropped randomly in empty regions of the IRAC images and then the fluxes corrected to total assuming PSF profiles (aperture correction multiplicative factors of 2.4, 2.7, 3.5, and 3.7 for the 3.6 μm , 4.5 μm , 5.8 μm , and 8.0 μm images respectively).
[a] Only source ID GNS-zD5 is covered in this MOIRCS image.
[b] Only source ID HDFN-3654-1216 is contained in this set.
References. (1) Beckwith et al. 2006; (2) Giavalisco et al. 2004; (3) Bouwens et al. 2007; (4) Williams et al. 1996; (5) Thompson et al. 2005; (6) Oesch et al. 2009; (7) Conselice et al. 2009, in preparation; (8) Bouwens et al. 2010a; (9) Thompson et al. 1999; (10) Dickinson 1999; (11) Labbé et al. 2003; (12) Kajisawa et al. 2006; (13) Ouchi et al. 2007; (14) Bouwens et al. 2008;

HUDF correspond to the 40 hr integration in the best seeing conditions in the K_s-band filter at ISAAC (VLT) and PANIC (Magellan; Labbé et al. 2006). We estimate 1σ depths of $\simeq 27.1-27.4$ AB magnitudes in $0\farcs9$ diameter apertures. The other two sources are in the HDFN and their K-band data come from the deep Subaru GTO MOIRCS imaging campaign (Kajisawa et al. 2006, Ouchi et al. 2007: see Bouwens et al. 2008 for a description of our reductions). We have only made use of the deepest GTO pointing which reaches down to 25.4 total AB magnitudes at 5σ ($0\farcs9$ diameter apertures). The FWHM for the K-band PSF is $\sim 0\farcs5$.

Deep optical B_{435}, V_{606}, i_{775}, and z_{850} observations are available for our candidates with ACS and typically reach to depths of ~ 30 mag in the HUDF and $\sim$1.5 mag shallower in the rest of our fields. For the single z-dropout candidate in the HDF-North WFPC2 field, we have the very deep ($\gtrsim 28$ mag at 5σ) B_{450}, V_{606}, and I_{814} WFPC2 observations – which permit

us to set very strong constraints on the strength of the Lyman Break.

The *Spitzer*/IRAC imaging data from the GOODS program (Dickinson et al. 2009, in preparation) provide us with deep rest-frame optical coverage on our $z \sim 7$ z-dropout candidates – which is critical for estimates of the stellar mass in these sources. Two exposures of ∼23-hr each were taken in two different epochs with the IRAC camera – rotated by 180 deg – and overlapping in the center of the GOODS field. The region of overlap contains the HUDF in the GOODS South. We find AB magnitude detection limits for point sources of 27.4, 26.6, 25.4, and 25.3 for the 3.6, 4.5, 5.8, and 8.0 μm channels respectively (1σ, measured on apertures of $1\farcs8$ in diameter and corrected to total flux assuming stellar profiles with aperture corrections of 2.4, 2.7, 3.5, 3.7 respectively – multiplicative factors). These limiting depths (for single epoch ∼23.3 hr IRAC observations) were estimated by dropping apertures at random empty regions of the sky and measuring the flux variations. A good summary of the IRAC observations is provided in Labbé et al. (2006) and Stark et al. (2007a), for example. In this work we make use of the reductions of Data Release (DR) 3 of epoch 1 observations and DR2 of epoch 2 of the GOODS-S field. In the case of the GOODS-N field we make use of the reductions of Data Release (DR) 2 of both epochs.

2.4 Photometry

Optical/near-IR Photometry: Optical to NIR fluxes were measured in standard $0\farcs9$-diameter circular apertures. We corrected these measured fluxes for the missing light outside these apertures assuming stellar profiles. These latter corrections increased the measured flux by 5% - 20% depending on the band. All the sources in our sample were sufficiently separated from their neighbors that we could use this simple approach, except for the one in the HDFN field where there was a faint but very close (almost overlapping) neighbor. This made it impossible to use the standard circular aperture to measure the flux of HDFN-3654-1216 (ID from Bouwens

et al. 2010a). To ensure that measurement of its flux was not contaminated by the flux of this neighbor, we fitted a PSF profile to the neighbor using GALFIT (Peng et al. 2002) and subtracted it from the image before measuring the flux of this z-dropout.

IRAC Photometry: One of the biggest challenges in estimating the masses of our $z \sim 7$ candidates is the acquisition of reliable mid-IR fluxes for these candidates from the available IRAC data. The extremely broad PSF of this instrument and large pixel sizes make the images extremely crowded and so fluxes from neighboring sources spill over onto each other. To overcome this issue, a wide variety of different approaches have been developed, almost all of which involve modeling the IRAC image with a number of smoothed sources of varying flux. In the most common cases, the model light profiles are theoretical like the ones produced by GALFIT. The use of these models can result in systematic errors in the photometry if the sources have irregular or clumpy spatial profiles.

We have used here the technique described in Labbé et al. (2006), which consists in the creation of an empirical light profile based in the higher resolution NICMOS images. This technique uses a segmentation map created by *SExtractor* (Bertin & Arnouts 1996) to define the boundaries of each source in the area to be cleaned (we use a 2σ threshold to ensure all the possibly relevant neighbors are fitted) and use the light profiles of the sources within those boundaries as the empirical light profiles (assuming a similarity between the profiles at both 1.6 μm and 3.6 μm). The individual profiles are then convolved with a carefully constructed kernel (based on the instrumental PSFs) to simulate how they would look in the IRAC images (modulo a normalization factor). Finally we fit for the total flux of each neighbor and subtract them off the image. Instead of using the z-dropout flux measurement determined from these fits, we subtract off the flux from the neighbors and perform standard aperture photometry in relatively small apertures on the "cleaned" image. We find that the optimal aperture diameter for maximizing the signal-to-noise ratio of our flux measurements (assuming point sources) is $\sim 1\farcs8$ in all the channels. The aperture corrections are 2.4, 2.7, 3.5, and 3.7 (multiplicative

factors) in the 3.6, 4.5, 5.8, and 8.0 μm channels respectively. The errors in the measured flux include both the typical variations on the sky brightness, and the uncertainty in the flux removed from the aperture.

A simple inspection of our images shows that 5 of the 11 $z \sim 7$ z-dropout candidates in our sample (i.e., GNS-zD2, GNS-zD5, UDF-387-1125, UDF-3244-4727, HDFN-3654-1216) are severely blended with bright foreground sources. The other six sources are more isolated but with the size of the instrumental PSF it is obvious that flux from neighboring sources will spill over onto these candidates (often contributing $\gtrsim$20% of the light within the 1.″8-diameter aperture centered on our candidates). Of the 5 severely blended sources we are able to satisfactorily "clean" the images in at least 2 cases (we will discuss the other three cases GNS-zD2, GNS-zD5 and HDFN-3654-1216 in the next paragraph). We could check the consistency of the method for 5 of the sources that were imaged in both epochs. As was mentioned before, there is a 180° rotation in the IRAC camera (and thus in the asymmetric instrumental PSF) between the two epochs, which makes the light profile models (for the neighboring sources) almost independent. Obtaining consistent fluxes in these two images is a good indication of the reliability of the method. For the sources where IRAC observations are from >1 epoch (and consistent within the measurement errors), we average the fluxes and combine the errors accordingly which reduces them by a factor $\sqrt{2}$.

In the cases of GNS-zD2 and GNS-zD5 strong color gradients in the closest neighbor cause the model light profiles to be inadequate and so large residuals are evident (after subtracting the flux from the neighbors). GNS-zD5 was imaged in both epochs and we find a difference of 2σ between the measurements in the 3.6 μm channel but a much cleaner residual (and better agreement) in the 4.5 μm image. A similar discrepancy was found for the 3.6 μm flux measurement for HDFN-3654-1216. In this case the poor subtraction is not due to strong color gradients but to the extreme proximity of its neighbor. In all three cases we adopt the single epoch uncertainty. Given the small size of our present sample of z-dropouts, we choose to

Table 2.2: Summary of Photometry

ID	Field	B_{435}	V_{606}	i_{775}	z_{850}	J_{110}	H_{160}	K_s^a	3.6 μm	4.5 μm
UDF-640-1417	HUDF	>29.9	>30.4	>29.9	27.8±0.2	26.5±0.2	26.1±0.2	25.8±0.2	25.2±0.1	25.9±0.4
UDF-983-964	HUDF	>29.9	>30.4	>29.8	>29.2	26.7±0.2	26.8±0.3	26.6±0.6	26.2±0.3	26.6±0.9
UDF-387-1125	HUDF	>30.0	>30.6	>30.0	29.1±0.8	27.7±0.4	26.9±0.3	>27.4	>27.5	>26.8
UDF-3244-4727	HUDF	>30.0	>30.4	>30.0	>29.4	27.6±0.3	26.9±0.3	>27.1	26.5±0.4	26.7±1.0
GNS-zD1	GOODS-S	>28.6	>29.0	>28.3	>27.9	26.5±0.3	26.2±0.2	...	24.9±0.1	25.4±0.4
GNS-zD2	GOODS-S	>28.9	29.0±1.0	>28.4	>28.4	27.0±0.4	26.7±0.3	...	26.4±0.6*	26.2±0.9
GNS-zD3	GOODS-S	>29.1	>29.4	>29.0	>28.7	27.3±0.7	26.7±0.3	...	25.7±0.3	25.9±0.7
GNS-zD4	GOODS-N	>28.5	>28.8	>28.4	>28.4	26.7±0.4	26.3±0.3	...	25.2±0.2	25.4±0.4
GNS-zD5[b]	GOODS-N	>28.8	>29.1	>28.7	28.1±0.7	26.2±0.3	25.3±0.1	25.4±0.2	24.6±0.1*	25.4±0.3
CDFS-3225-4627	GOODS-S	>28.7	>29.0	>28.6	>28.4	26.8±0.4	26.4±0.3	...	26.1±0.3	26.0±0.5
HDFN-3654-1216[c]	HDFN	>29.2	>29.4	>28.6	26.5±0.2	26.2±0.2	25.9±0.2	26.4±0.4	25.2±0.3*	25.7±0.7
Mean SED[d]		>30.3	>30.6	>30.1	28.41±0.29	26.70±0.09	26.27±0.07	26.68±0.30	25.58±0.07	25.91±0.18

Notes. Magnitudes are total and in the AB system. Optical to near infrared photometry measured in $0''.9$ diameter apertures with aperture corrections of 5% - 20% (derived assuming stellar profiles). Mid infrared IRAC photometry performed on "cleaned" images with $1''.8$ aperture diameters. Aperture correction factors in this case are 2.4 and 2.7 in the 3.6 and 4.5 μm channels respectively. Upper limits and error bars are 1σ.
[a] K-band from either MOIRCS or ISAAC depending on the Field, see Table 2.1.
[b] After subtracting a bright nearby neighbor from the 3.6 μm image of this source, sizeable residuals remain, and so the quoted 3.6 μm flux measurements from these sources may suffer from systematic errors.
[c] MOIRCS J_s band imaging is deep enough at the location of this source. We measure $J_s = 25.6 \pm 0.3$.
[d] There are additional WFPC2 optical imaging constraints for HDFN-3654-1216: $B'_{450} > 30.2$, $V'_{606} > 29.0$, $I_{814} > 28.8$.
[e] This mean SED was constructed rescaling all the SEDs so that the H_{160}-band fluxes coincide with the mean value and then averaging all the other bands. The 3.6 μm IRAC fluxes from sources GNS-zD2, GNS-zD5, and HDFN-3654-1216 were excluded from the average. See section Section 2.6.2 and Figure 2.4.

keep these three sources in the sample – keeping in mind the caveat that the flux measurements for these sources could possess large systematic errors. In summary, we are able to perform reliable cleaned photometry on 8 out of the 11 sources (73%).

We obtain $> 2\sigma$ detections for 9 of the 11 sources in the 3.6 μm image and for 5 sources in the 4.5 μm image. The two sources with quite marginal ($< 2\sigma$) detections in both IRAC images are UDF-387-1125 and GNS-zD2. A simple stacking of the images of these two sources (adding both sources in both IRAC images) shows a significant detection, which provides evidence for the reality of the sources.

Optical to mid-Infrared image stamps ($\sim 4'' \times 4''$) for all the sources are presented in Figure 2.1. The 5.8 μm and 8.0 μm channels have been omitted because none of the sources are detected in those bands (as expected). The two epochs have been co-added when available. The measured magnitudes are summarized in Table 2.2.

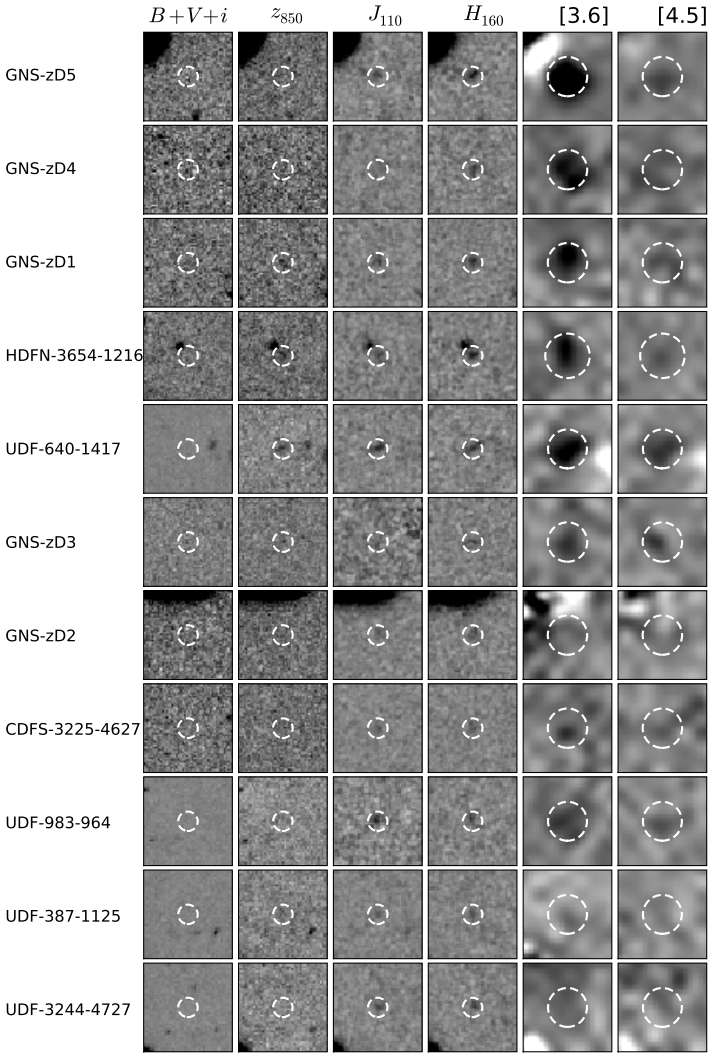

Figure 2.1: Postage stamps of the $z_{850}-$dropouts. Each stamp is $4''\times4''$ in size ($\sim$ 21 kpc at $z = 7$). The dashed circles indicate the apertures used for photometry ($0\farcs9$ for the optical to NIR and $1\farcs8$ in the IRAC bands). All the sources are undetected in B_{435}, V_{606}, and i_{775} and only UDF-640-1417 and HDFN-3654-1216 are weakly detected in z_{850}. The last two sources are estimated to be the lowest redshifts of the sample. 3.6 μm and 4.5 μm stamps show the sources after the flux from the nearby neighbors have been fit and removed (i.e., they are "cleaned" images), with the two epochs of IRAC data added together when available. The cleaning process in the case of sources GNS-zD5 and GNS-zD2 has left nearby residuals (seen in white) attributed to the close and bright nearby sources visible in the other bands. To a lesser degree this seems to also be the case for sources UDF-640-1417 and UDF-3244-4727. Since these latter sources were observed in both epochs, it was possible to check that the measured fluxes are consistent among them. As expected, all sources are undetected in the 5.8 and 8.0 μm channels. The sources have been placed in order of increasing H_{160} magnitude from top to bottom.

2.5 Photometric Redshifts

Perhaps the most fundamental quantity that we can estimate for galaxies in our z_{850}-dropout sample is their redshift. We first explore the probable redshifts of our sources using the photometric redshift code EAZY (Brammer et al. 2008). The code works by comparing the observed photometry with that predicted on the basis of the specific SED templates. We use the default template set which was derived from the Pegase population synthesis models (Fioc & Rocca-Volmerange 1997) and optimized to reproduce the properties of galaxies in the range $0 < z < 4$. Comparisons of the photometric redshift estimates output from EAZY with some of the deepest spectroscopic surveys available show minimal systematic errors and a scatter in $z_{spec} - z_{phot}$ of $\sigma = 0.034$ over the range $0 < z < 4$ (see Table 1 in Brammer et al. 2008). The few sources at higher redshifts ($z \sim 6$) with available spectroscopy are also in good agreement with its photometric redshift estimates. One relevant advantage over other photometric redshift codes is that EAZY works with fluxes instead of magnitudes and naturally handles negative measurements, which are common in our optical bands.

We use the available flux measurements in the B_{435}, V_{606}, i_{775}, z_{850}, J_{110}, H_{160}, 3.6 μm, 4.5 μm bands, and also the B'_{450}, V'_{606}, I_{814}, K bands if available for our photometric redshift estimates. We do not include the IRAC 5.8 μm and 8.0 μm flux measurements of the sources (consistent with no detection) in the comparison – since they do not help us to meaningfully discriminate between the competing redshift solutions. We restrict the redshift range of our fits to $z \sim 4 - 11$ and adopt no redshift prior. Solutions at $z \sim 1.5$ are also possible for most of the sources but at lower probability for all of them. However, quantifying this is challenging given our poor knowledge of the demographics of galaxies at both $z \sim 1.5$ and $z \sim 7$. Furthermore, the existence of synthetic solutions at any of these redshifts does not necessarily imply the existence of real galaxies with the observed properties. We have provided an independent (short) description of the estimate of the fraction of low-redshift contaminants

in Section 2.2. A more detailed discussion is provided in the Bouwens et al. (2010a) study where the sample is described (but see also Bouwens et al. 2008 which describes the estimate for a similar sample). The estimated contamination fraction for this sample is $\sim 10\%$ and $\sim 20\%$ for sources in the HUDF and outside the HUDF, respectively.

We explore the solutions in the range $4 < z < 11$ in a grid with steps of 0.01. At each step there is a $\chi^2(z)$ value associated with the best solution that is used to create a probability function $p(z) \propto \exp[-\chi^2(z)/2]$. The redshift is estimated marginalizing over this probability and probability contours are used to determine the 68% confidence intervals. Because of the shape of this function at redshifts $z > 7$, the estimated redshifts are usually located somewhat above the absolute minimum χ^2. The typical $1\,\sigma$ uncertainties we estimate for individual sources are of order $\Delta z = \pm 0.6$. Finally, the redshift distribution obtained from EAZY is $z = 7.2 \pm 0.5$, similar to what would be expected based on the shape of the ACS z_{850} passband and the color cuts imposed in the sample (see Figure 2.2).

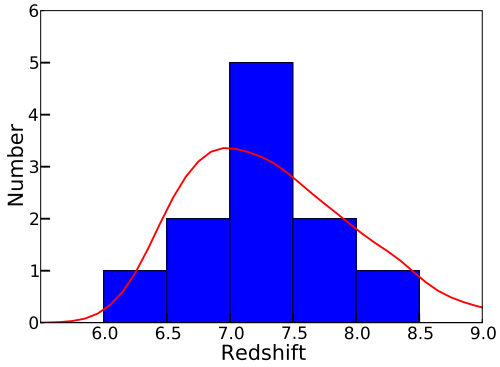

Figure 2.2: The photometric redshifts of our $z \sim 7$ z-dropout sample (histogram). The solid line shows the redshift distribution that Bouwens et al. (2008) predict for the z-dropout selection. The photometric redshifts were estimated with EAZY (see Section 2.4). Typical uncertainties in the redshift for individual sources is $\Delta z \sim 0.6$. The lowest redshift in the sample corresponds to object HDFN-3654-1216 at $z = 6.2$. This object presents the bluest $z_{850} - J_{110}$ color due to it being weakly detected in the z_{850} band image.

2.6 Stellar Population Modeling

We can make sense of the present photometric selection of z-dropouts in terms of their *intrinsic* properties – like age, stellar mass, or dust extinction – by modeling the spectral energy distributions observed for individual sources. Such modeling is now ubiquitous in the literature (Sawicki & Yee 1998, Brinchmann & Ellis 2000, Papovich et al. 2001, Labbé et al. 2007), and has proven quite powerful in the interpretation of distant galaxies – both given the abundance (and quality) of photometric data and the plausibility of the photometric estimates. Indeed, studies have found reasonable agreement between stellar masses determined from such modeling and those determined from the dynamics (Erb et al. 2006c).

Here we model the stellar populations with the Bruzual & Charlot (2003; hereafter BC03) spectral synthesis libraries. Over the wavelength range covered by the present study, these libraries show almost no difference with respect to the newest Charlot & Bruzual (2012, in preparation, hereafter CB07; e.g. Stark et al. 2009, Labbé et al. 2010b) and have been shown to be in reasonable agreement with other libraries (e.g., Maraston 2005). We use a Salpeter (1955) initial mass function (IMF) between 0.1 and 100 $M_{\odot}$ and sub-solar metallicity (0.2 $Z_{\odot}$) so that comparisons to existing works are more straightforward. Our selection of sub-solar metallicity models is based on the observed trends at high redshifts (e.g., Maiolino et al. 2008) as well as on the direct observations of extremely blue UV slopes of the most recently found $z \sim 7$ sources (Bouwens et al. 2010c, Labbé et al. 2010b). However, since other IMFs (or metallicity models) fit our observations just as well, we will remark on how the results change if we adopt a different IMF or metallicity. For simplicity, we assume a constant star formation (CSF) rate when modeling the star formation histories of the galaxies in our sample. This assumption seems preferable to an exponentially-decaying SF history (which implies increasing SFRs with redshift), as there is currently no evidence that UV-selected samples form stars at a faster rate at earlier epochs (e.g., Papovich et al. 2001; Stark et al. 2009, and others).

Finally, given the challenges in constraining both age and reddening based upon the photometric information available for individual sources, we will assume that galaxies in our sample show negligible dust extinction when doing the stellar population modeling. We have good reasons for making this assumption. $z \gtrsim 5$ galaxies have been found to have very blue UV-continuum slopes β and thus little dust extinction (e.g., Lehnert & Bremer 2003, Stanway et al. 2005, Yan et al. 2005, Bouwens et al. 2006; 2010c). As we will show later, a similarly steep UV-continuum slope β (-2.4 ± 0.4) is found for the mean SED of our sample (Section 2.6.2) – again suggesting minimal dust extinction. For individual sources, however, it is difficult for us to obtain useful constraints on the UV-continuum slope and hence dust extinction. While we have high quality H_{160}-band fluxes for our candidates, the other fluxes we have which probe the UV-continuum are not adequate: the J_{110}-band fluxes we have available depend significantly on the redshift of the source (the J_{110}-band extends to $\sim$8000 Å) and the K-band fluxes (available on fewer sources) are more uncertain in general (due to the shallower nature of the K-band imaging data). We have tested the impact of allowing modest amounts of extinction ($A_V < 0.5$) to the models and found that the main results (SMD, sSFR, ages) are unchanged or at least consistent within the uncertainties.

Within these general specifications, we explored a wide variety of different parameters (redshift, Age) in modeling the observed photometry of each $z \sim 7$ candidate:

$$\begin{aligned} z &= 4.0 - 11.0 \text{ (steps of 0.01)} \\ \log(\text{Age[Myr]}) &= 7.5 - \text{Age}_{\text{max}} \text{ (steps of 0.01)}, \end{aligned}$$

where Age_{max} is the age of the universe at the corresponding redshift so that the models avoid solutions in which the populations are older than the universe. To derive 68%, 95%, and 98% confidence intervals for the above parameters, we ran a number of simulations where we added photometric scatter (noise) to the observed fluxes and then used the results to determine the threshold χ^2 values that encompass these confidence intervals. We performed the above calcu-

lations with the stellar population modeling code named FAST (see appendix in Kriek et al. 2009).

Note that in stellar population modeling, we do not use the photometric redshift estimates from the previous section. This was to avoid additional complications in the definition of the confidence intervals (as the templates are slightly different). However, we found that the two redshift estimates are consistent (the typical discrepancies are rms $\Delta z \sim 0.04$).

In Figure 2.3, the observed SEDs are presented along with the best fit models with no extinction. The corresponding properties we derive for these galaxies using these models are detailed in Table 2.3. The ages in that table correspond to the average age of the stellar population, i.e., $M_{\rm total}^{-1} \int t_{\rm lookback} {\rm SFR}(t_{\rm lookback}) dt_{\rm lookback}$ (=age$_w$). In the case of constant SFR models, this is simply equal to one half of the time elapsed since the onset of star formation. Similar to what others have found at somewhat lower redshifts, these models indicate the presence of quite massive systems very early in the universe. We find masses in the range of $0.2 - 12 \times 10^9 M_\odot$. These models also show quite large ages that place the formation of most of the stars up to 380 Myrs earlier with typical values on the order of 300 Myr. The uncertainties in the derived age, however, are quite substantial, typically $^{+70}_{-120}$ Myr (68% confidence intervals). From Table 2.3, it can be noticed that the values of age$_w$ imply that some galaxies have been forming stars for times comparable to the age of the Universe at this redshift. We have preferred not to impose any arbitrary restrictions on the time of onset of star formation because any redshift constraint (e.g., $z < 100$) would not meaningfully restrict the ages (16 Myr for $z < 100$), particularly when compared to the uncertainties associated with the estimation, typically $^{+70}_{-120}$ Myr. Such constraint implies insignificant fractions of stellar mass assembled at extreme redshifts.

2.6.1 Parameter dependencies

In the above stellar population modeling, we adopted a Salpeter IMF and assumed sub-solar metallicity ($0.2\,Z_\odot$). We also explored the effects of using a Chabrier IMF and of

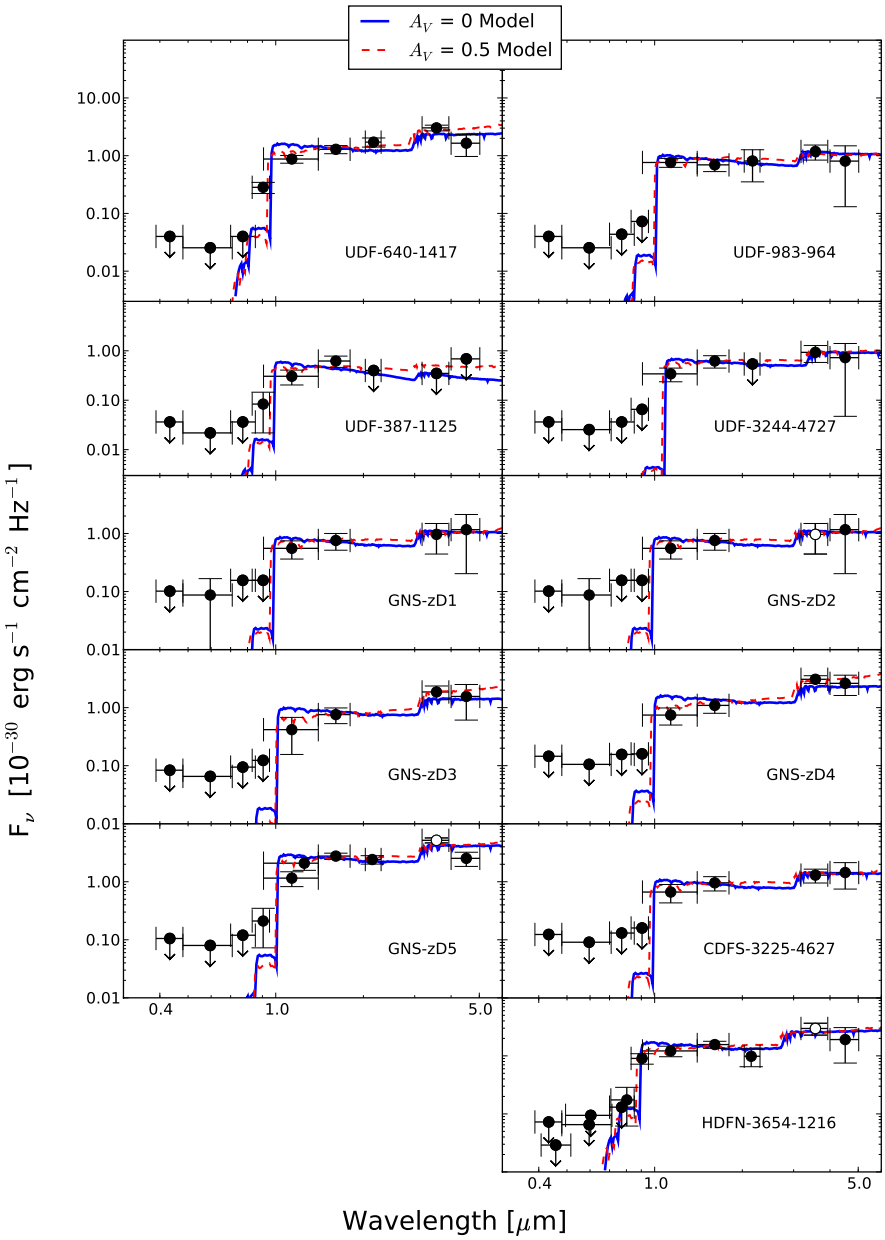

Figure 2.3: Observed SEDs and synthetic stellar population model fits. The error bars and upper limits are 1σ. The models shown here are from Bruzual & Charlot (2003) with a Salpeter IMF and $0.2\,Z_\odot$. The red curve represents the best fit models without extinction and the blue curve shows the effect of imposing a maximal extinction of $A_V = 0.5$. The open circles shown for the 3.6 μm flux measurements of objects GNS-zD2, GNS-zD5, and HDFN-3654-1216 correspond to points with poor photometry.

Table 2.3: Summary of BC03 Model Fit Parameters

ID	$z_{\rm phot}$	Mass ($10^9\ M_\odot$)	Age^a_w (Myr)	SFR$_{L_{1500}}$ ($M_\odot$ yr^{-1})	SFR ($M_\odot$ yr^{-1})	sSFR^b (Gyr^{-1})	$L^d_{\rm UV}$ ($10^{10}\ L_\odot$)	M/L_V ($M_\odot/L_\odot$)	U–V	$H_{160}-3.6$	$\chi^2_{\rm red}$
UDF-640-1417	$6.9^{+0.1}_{-0.1}$	$6.6^{+0.3}_{-0.9}$	379	13.2	$10.5^{+0.7}_{-0.7}$	$2.0^{+0.3}_{-0.1}$	5.4	0.19	0.5	0.9	1.7
UDF-983-964	$7.3^{+0.4}_{-0.3}$	$2.2^{+2.0}_{-1.5}$	173	9.0	$7.4^{+2.4}_{-1.4}$	$4.1^{+8.9}_{-1.9}$	3.7	0.14	0.1	0.6	0.4
UDF-387-1125	$7.1^{+2.0}_{-0.5}$	$0.2^{+1.4}_{-0.1}$	19	4.8	$5.2^{+5.0}_{-2.4}$	$25.6^{+12.3}_{-22.6}$	2.0	0.02	-0.7	-0.8	0.3
UDF-3244-4727	$7.9^{+0.8}_{-0.6}$	$2.8^{+0.5}_{-2.1}$	315	6.8	$5.4^{+2.0}_{-1.2}$	$2.4^{+6.9}_{-0.4}$	2.8	0.21	0.4	0.4	0.9
GNS-zD1	$7.2^{+0.2}_{-0.2}$	$7.6^{+0.4}_{-0.5}$	362	15.8	$12.6^{+1.2}_{-1.1}$	$2.1^{+0.1}_{-0.1}$	6.5	0.15	0.5	1.3	1.5
GNS-zD2	$7.1^{+1.5}_{-0.6}$	$2.5^{+1.8}_{-2.2}$	251	7.3	$5.9^{+6.4}_{-1.6}$	$3.0^{+24.7}_{-1.3}$	3.0	0.20	0.3	0.3	0.4
GNS-zD3	$7.3^{+0.9}_{-0.4}$	$4.2^{+0.4}_{-1.5}$	354	8.8	$7.1^{+2.0}_{-1.1}$	$2.1^{+1.2}_{-0.2}$	3.6	0.15	0.4	1.0	0.3
GNS-zD4	$7.2^{+0.4}_{-0.2}$	$6.8^{+0.3}_{-0.7}$	362	13.9	$11.2^{+1.4}_{-1.2}$	$2.1^{+0.3}_{-0.1}$	5.7	0.16	0.5	1.1	0.8
GNS-zD5	$7.3^{+0.2}_{-0.2}$	$12.3^{+0.3}_{-2.1}$	354	26.1	$20.9^{+1.5}_{-1.4}$	$2.1^{+0.4}_{-0.0}$	10.7	0.22	0.4	0.7	2.3
CDFS-3225-4627	$7.1^{+1.5}_{-0.5}$	$3.5^{+2.0}_{-2.3}$	281	9.2	$7.4^{+5.2}_{-1.8}$	$2.7^{+5.2}_{-1.0}$	3.8	0.22	0.3	0.3	0.6
HDFN-3654-1216	$6.3^{+0.2}_{-0.2}$	$6.9^{+0.3}_{-3.8}$	426	12.4	$9.8^{+1.7}_{-0.9}$	$1.8^{+2.2}_{-0.1}$	5.1	0.27	0.5	0.7	0.8
Mean SED^c	$7.3^{+0.1}_{-0.0}$	$6.3^{+0.1}_{-0.1}$	354	13.4	$10.7^{+0.5}_{-0.2}$	$2.1^{+0.0}_{-0.0}$	5.5	0.28	0.4	0.7	3.3

Notes. Best fit parameters, 68% confidence intervals and corresponding χ^2 for Bruzual & Charlot (2003) fits with subsolar metallicity ($0.2\,Z_\odot$) and Salpeter IMF between 0.1 and 100 $M_\odot$. We obtain a redshift for the sample of 7.2 ± 0.5. The models suggest that in some of these galaxies most of the stars were born at considerably earlier times ($z \lesssim 10$), well into the epoch of reionization. The masses of these sources range $(0.2 - 12) \times 10^9\,M_\odot$. We have restricted the dust extinction to zero, consistent with the trend observed at these high redshits. SFRs from the models are consistent with the ones derived from the extrapolated L_{1500} using the usual Madau et al. (1998) formula. These SFRs are somewhat high, $\sim 10\,M_\odot\,{\rm yr}^{-1}$ typically. The mean sSFR of the sample is $2.4 \pm 0.6\,{\rm Gyr}^{-1}$, with an outlier corresponding to the youngest model. The estimated best fit ages do not change considerably if we consider either Chabrier IMF or solar metallicity models. As expected for a Chabrier IMF, the masses derived are a factor ∼0.55 lower and so are the SFRs. Solar metallicity models produce masses ∼ 10% larger. The maximal extinction model with $A_V = 0.5$ produces ∼ 45% lower ages and ∼ 45% higher masses (with the consequent increase in SFR) with more scatter.

[a] Age$_w$ corresponds to the SFH-weighted ages. In the case of CSF models, this corresponds to half the time since the onset of star formation. The typical uncertainties in this quantity are substantial ($^{+70}_{-120}$ Myr).

[b] The sSFR (= SFR/Mass) here is derived from the extrapolated L_{1500} luminosity and the masses from the CSF models.

[c] These are not the mean values of the best fit parameters derived for the sample but rather the parameters derived from the modeling of the mean SED described in Section 2.6.2 (see Figure 2.4).

[d] To convert L_{UV} into $L_\odot$ units we have used $L_\odot = 3.826 \times 10^{33}$ erg s^{-1} and assumed a monochromatic νL_ν.

varying the metallicity of the models. We find that, while the distribution of best fit redshifts and ages is unchanged, the derived masses are ∼45% smaller if we use Chabrier IMF (instead of Salpeter), and 10% larger if we consider models with solar metallicity (instead of $0.2\,Z_\odot$). For both metallicities ($0.2\,Z_\odot$ and $Z_\odot$) and both IMFs (Chabrier and Salpeter), we obtain reasonable χ^2 fit results, so there is no reason to prefer one IMF or metallicity over the others.

We have also assumed that our sources suffer from minimal dust extinction (both due to the very blue UV-continuum slope β measured from the mean SED here [Section 2.6.3] and due to the blue UV-continuum slopes β observed at $z \gtrsim 5$: Lehnert & Bremer 2003, Stanway et al. 2005, Yan et al. 2005, Bouwens et al. 2006; 2010c). However, this extinction is not very well constrained for individual $z \sim 7$ galaxies (which lack strong constraints on their UV-continuum slopes), and so it is worthwhile to mention how larger values of the dust extinction would affect

the ages and stellar masses derived from our modeling. Imposing an extinction of $A_V = 0.5$ (following Calzetti et al. 2000 – we consider this a safe upper limit based on the previously mentioned studies), yields best fit models that are $\sim 40\%$ more massive (to compensate for the dimming) but $\sim 45\%$ younger (which prevents their $H - [3.6]$ colors from becoming too red to match the observations) with the consequent increase in SFR. We also find reasonable χ^2 for these models.

Finally, we must remember that we adopted a specific form for the SFH – supposing the SFR for each was constant in time. We could easily have adopted other star formation histories (instantaneous burst, exponentially decaying) in fitting the observed SEDs and found acceptable results. To determine the approximate effect of the star formation history on our derived parameters, we also considered exponentially decaying $e^{-t/\tau}$ histories and instantaneous bursts in modeling our sources. In general we found larger ages and masses for histories with larger τ's (where τ for a constant SFR model is of course ∞ and 0 for an instantaneous burst) though all assumed histories produced acceptable fits. In that sense, the unrealistic instantaneous burst models provide a lower limit for the age$_w$ of the sample that we find to be 80 Myr. Using a more reasonable approximation like $\tau = 100$ Myr this number goes up to 170 Myr. This latest result would imply that we are observing a quiescent population right after the main star formation episode is over, which seems unlikely.

While we note these dependencies, we will use our fit results assuming no dust extinction, a Salpeter IMF, sub-solar metallicity ($0.2\,Z_\odot$), and a constant SFR when deriving results in subsequent sections and in particular to estimate the Stellar Mass Density (SMD) of the universe. Relaxing our assumption that there is no dust extinction (A_V=0) to $A_V < 0.5$ produces no significant change in the derived quantities.

2.6.2 Average Spectral Energy Distribution

One significant challenge in modeling the stellar populations of z-dropouts in our sample is the faintness of the sources and therefore the still sizeable uncertainties in the fluxes we derive. Consequently, it becomes difficult for us to obtain tight constraints on the model parameters – like dust or age – for individual sources.

We can obtain much tighter constraints by averaging the measured fluxes for the sources and deriving a mean spectral energy distribution, per unit wavelength. This is particularly valuable for a determination of the UV-continuum slope β for the sample, since this slope is constrained from the H and K_s-band fluxes and since the K-band flux is only poorly constrained for individual sources. To derive this mean SED, we first normalize all the sources to the average H_{160}-band flux and then take a weighted mean of the fluxes of all sources ($< x >= \sum(x_i/\sigma_i^2)/(\sum 1/\sigma_i^2)$). The mean K-band flux is derived from the 6 sources where we have deep K-band data. The sources with poor photometry (GNS-zD2, GNS-zD5 and HDFN-3654-1216 in 3.6 μm) were not considered when taking the mean. The mean SED is presented in Table 2.2 and Figure 2.3. The UV-continuum slope β we estimate from the H and K photometry is -2.4 ± 0.4.

We perform the stellar population modeling for this source in the same way as for the other sources and include the estimated properties in Table 2.3. When modeling, however, the z_{850} flux has not been included in the fits to minimize the influence of our lowest redshift sources. The best-fit model is also compared with the mean SED in Figure 2.3. If we allow the dust reddening to be non-zero and include that in the fits, we find a best fit $A_V = 0.4$. This provides support for our assumption in Section 2.6 that our $z \sim 7$ galaxy candidates are largely dust free. Using the mass of the best fit to the mean SED ($6.3 \times 10^9\,M_\odot$) and the extrapolated luminosity at 1500 Å ($5.5{\times}10^{10}\,L_\odot$) we infer a mass to light ratio of $M/L_{\rm UV} = 0.12\,M_\odot/L_\odot$, and also an $M/L_V = 0.28\,M_\odot/L_\odot$ (from $L_V = 2.2 \times 10^{10}\,M_\odot$ measured from the best fit model

at 5500 Å). We will use these M/L ratios to provide one estimate of the SMD in Section 2.7.

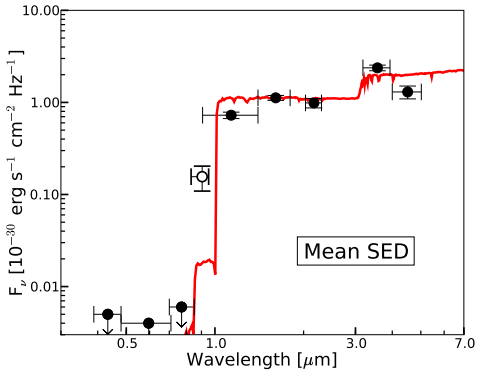

Figure 2.4: The average observed SED (black circles) for galaxies derived from the 11 sources in our z-dropout selection. Error bars and upper limits are at 1σ. The fluxes of each source in our $z \sim 7$ z-dropout selection were scaled so that the H_{160}-band flux matched the average H_{160}-band flux for the sample, after which the rescaled fluxes from the entire sample were averaged. Flux measurements which were poor (due to difficulties in precisely subtracting a nearby neighbor, as for the 3.6 μm flux measurements of GNS-zD2, GNS-zD5, and HDFN-3654-1216) were not included in the average. Note, the average K-band flux we derive here was only determined from the 6 sources for which we had deep K-band data. Stellar population models were fit to this average observed SED using the same technique that was used for individual sources (model shown in solid line). The parameters of the fit are presented in Table 2.3. The average z_{850}-band flux (open circle) was not included in the fit – since it would not make sense to include both the z_{850} and J_{110}-band flux (both of which have a different dependence on redshift) in the fits. This average SED shows no detection in the optical B, V, or i bands and a very large break (> 3 mag) between the optical and J bands – suggesting that the majority of sources in our sample do in fact correspond to $z \sim 7$ galaxies. The extremely blue $H - K$ color, which traces the UV continuum, imply that the dust reddening must be very low – consistent with our assumptions in modeling individual z-dropouts (Section 2.6). The pronounced break (~ 1 mag) between the K and the 3.6 μm bands suggests the presence of a Balmer break, indicating that the typical $z \sim 7$ galaxy has experienced several previous generations of star formation. We have used the derived M/L ratio from this mean SED to make a simplified estimate of the stellar mass density of the universe at $z \sim 7$ of $4.5 \times 10^5\, M_\odot\, \mathrm{Mpc}^{-3}$ (see Section 2.7).

2.6.3 Specific Star Formation Rate

A key quantity in considering the build-up of stars within a galaxy is the specific star formation rate – similar to the b parameter which was more frequently used in the past to characterize a galaxy's star-formation history. It is the star formation rate within a galaxy divided by its stellar mass – or equivalently the fraction of the stellar mass in a galaxy that

forms per unit time. As such, the sSFR provides us with a useful way of thinking about galaxy growth over cosmic time – and so it is not surprising that it has been estimated out to $z \sim 6$.

Here we make use of our best fit synthetic models to estimate L_{1500} and then use the usual formula from Madau et al. (1998) to estimate the SFR. We combine this with the masses of the best fit models to obtain the specific SFR (see caption in Table 2.3). We find values of $1.8 - 4.1$ Gyr^{-1} for this quantity across our sample, with a median value of 2.4 ± 0.6 Gyr^{-1} (the outlier at $\sim$20 Gyr^{-1} is undetected in the mid-IR so the constraints are poor). To put this value in context, it makes sense for us to compare our derived sSFRs with the values at lower redshift. Given that the sSFRs can depend somewhat on stellar mass, we compare our results to the same median mass as we find in our sample, 5×10^9 $M_\odot$. From the data presented in Stark et al. (2009), we find 2.1, 2.0, and 2.0 Gyr^{-1} in their $z \sim 4, 5$, and 6 samples; from Papovich et al. (2001), Sawicki et al. (2007) and Daddi et al. (2007) we find ~ 2 Gyr^{-1} at $z \sim 2$; and from Noeske et al. (2007) we estimate $0.3 - 1.2$ Gyr^{-1} for $z \sim 0.2 - 1$ samples. At $z \sim 2$, Reddy et al. (2006) find a much higher value of ~ 10 Gyr^{-1} but at that mass it is only based on MIPS detected sources. Obviously, any MIPS-detected sample would be biased to include only those sources with substantial enough SFR to show MIPS detections, and hence probably is not representative for the $10^{9.5} M_\odot$ population. The results are shown in Figure 2.5.

From $z \sim 7$ to $z \sim 2$, there is little apparent evolution in the sSFR, and the present results provide a continuation of the trend delineated by Stark et al. (2007a) and Yan et al. (2006) from the Reddy et al. (2006) points. However, from $z \sim 2$ to $z \sim 0$ the sSFR shows a rapid decrease. This suggests that SFR at $z > 2$ mostly proceeds in a largely self similar way, but that at $z < 2$ there must be some physical processes inhibiting SFR. Similar to many other comparisons of merit, e.g., evolution of M^* with redshift (Bouwens et al. 2006; 2007, Yoshida et al. 2006), we find that SF in galaxies at $z \gtrsim 2$ seems to follow somewhat different principles than for galaxies at $z \lesssim 2$.

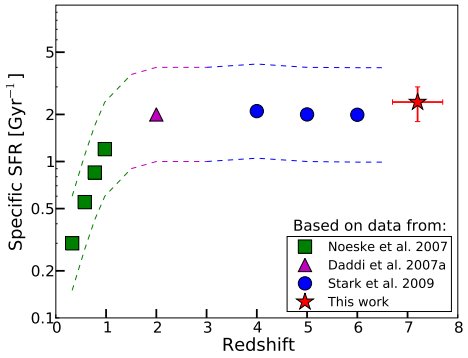

Figure 2.5: The sSFR measured from our data at $z \sim 7$ compared to the values derived from the data presented by others at a constant stellar mass of 5×10^9 $M_\odot$ (corresponding to the median of the present sample). Our estimates of the sSFR are based on results from Noeske et al. (2007), Daddi et al. (2007) (in good agreement with Papovich et al. 2001), and Stark et al. (2009). We estimate that the typical errors at $z < 7$ (dashed lines) are ~ 0.3 dex. The sSFR seems to be remarkably constant at 2 Gyr^{-1} between $z \sim 2 - 7$ suggesting that the star formation - mass relation does not evolve strongly between $z \sim 2 - 7$. The drop observed at $z < 2$, however, indicates that some physical process might be inhibiting star formation. This result suggests that star formation in galaxies at $z \gtrsim 2$ follows somewhat different principles than for galaxies at $z \lesssim 2$.

2.7 Stellar Mass Density

One of the most fundamental quantities we can try to infer from $z \sim 7$ selections and the present stellar population modeling is the stellar mass density. The stellar mass density tells us how much star formation occurred in the universe to the point of observation, and therefore provides us with a very powerful constraint on early galaxy formation.

2.7.1 Selection Volumes

An essential step in determining the stellar mass density from our $z \sim 7$ z-dropout selection is obtaining an accurate estimate of the selection volume. This requires that we model the selection of dropout galaxies from all six of the Bouwens et al. (2010a) search fields and estimate the effective volume we are able to search versus H_{160}-band magnitude. The selection volumes are calculated by adding artificial sources to our search fields and then attempting to reselect them as $z \sim 7$ z-dropouts according to the criterion described in Section 2.2. The

artificial sources are assumed to have a mean UV-continuum slope β of -2, consistent with the observed trends at $4 < z < 6$ (Bouwens et al. 2009). Their pixel-by-pixel surface brightness profiles are identical to those of random $z \sim 4$ B-dropouts from the HUDF (Bouwens et al. 2007) of similar brightness, but their sizes have been rescaled as $(1+z)^{-1}$, following the observed size trends with redshift at $z > 2$ (Oesch et al. 2010b, Ferguson et al. 2004, Bouwens et al. 2004a). We have not included the possible contribution from Lyα emission to the SEDs. A more detailed description of these simulations can be found in Bouwens et al. (2010a; but also see Bouwens et al. 2008).

We estimate the following total search volumes as a function of H_{160}-band magnitude for the entire Bouwens et al. (2010a) $z \sim 7$ z-dropout selection (from both the *HST* NICMOS and ground-based near-IR data):

$$V_{eff}(H_{160}) = \begin{cases} 33 \times 10^4\,\mathrm{Mpc}^3, & \text{if } 25.3 < H_{160} < 25.8 \\ 16 \times 10^4\,\mathrm{Mpc}^3, & \text{if } 25.8 < H_{160} < 26.3 \\ 6.0 \times 10^4\,\mathrm{Mpc}^3, & \text{if } 26.3 < H_{160} < 27.1 \\ 1.2 \times 10^4\,\mathrm{Mpc}^3, & \text{if } 27.1 < H_{160} < 27.5 \end{cases}$$

2.7.2 Stellar Mass Density Determinations

We proceed now to estimate the stellar mass density of the sources we find in these search volumes. We do so in the three different ways, as detailed below:

Direct Approach. Here we estimate the stellar mass density by simply summing over the expected mass density to come from each source. The expected mass density is simply the estimated stellar mass for a source multiplied by the likelihood it is not a contaminant (90% for sources in the HUDF and 80% otherwise) divided by the selection volume above. The stellar mass density we derive by summing over the 11 sources is 5.7×10^5 $M_\odot$ Mpc^{-3}. We estimate the uncertainties in the mass density by bootstrap resampling (detailed below). This approach has

the advantage of being very direct and even-handedly including all candidates in our selection in the estimate. The disadvantage, of course, is that this estimate may be affected by the mass estimates of the three z-dropouts with perhaps unreliable 3.6 μm fluxes.

Mean SED Approach. For our second estimate, we use our average SED from Section 2.6.2 to derive the mean $M/L_{\rm UV}$ ratio for sources in our sample – reasoning that this M/L ratio is much more accurately known than any individual M/L ratio in our sample. If the photometric redshifts are accurate ($z \sim 7.2 \pm 0.5$), then the limiting depth of our search corresponds to $\sim M_{\rm UV,AB} = -20$. We have then used the Bouwens et al. (2008) UV LF at $z \sim 7$ to estimate the UV Luminosity density integrated to that depth and multiplied it by the $M/L_{\rm UV}$ ratio to obtain a stellar mass density of $4.5{\times}10^5$ $M_\odot$ Mpc^{-3}. Again for the uncertainties, we rely on a bootstrap resampling procedure (below).

Random M/L Approach. For our final estimate of the stellar mass density, we ran a monte-carlo simulation where we match up the 11 galaxies in our $z \sim 7$ z-dropout sample with randomly sampled M/L ratios from the 8 galaxies with reliable IRAC fluxes. We then divide the masses by the search volumes that correspond to their UV luminosities. After repeating the match up process 100000 times we find a median value of $6.6{\times}10^5$ $M_\odot$ Mpc^{-3}. The estimate of the uncertainties based on bootstrap resampling is described below.

Uncertainty Estimates. To estimate the uncertainties in our estimate of the stellar mass density at $z \sim 7$, we must fold in the many uncertainties that contribute to this density, including uncertainties in the sampling of the LF, the M/L ratios of the galaxies we uncover in our search, whether any individual source is a contaminant, and finally the mass estimates themselves of candidates in our sample.

The simplest way of including all these uncertainties in our final estimate is to run a Monte-Carlo simulation. For each simulation, we iterate over all 11 candidates in our sample and include $P_1(x)$ number of sources in that trial with a UV luminosity equal to that candidate – where $P_1(x)$ is a Poisson distribution with mean equal to 1. Then, we run over all the

sources and give each source 10-20% chance of being thrown out (to account for uncertainties in the contamination fraction). Next, we assign a mass to each of the objects in the particular realization by drawing a random $M/L_{\rm UV}$ from the observed values. When doing this, we also include individual uncertainties in the $M/L_{\rm UV}$ determinations, specifically, we make a weighted choice of a mass from the distribution associated to a particular source (with the weights derived from the χ^2 as was already described for the determination of the ages). Finally, we divide each source by the selection volume appropriate to its UV luminosity and sum the sources to calculate the stellar mass density for a given trial. We repeated the simulation 10000 times to ensure that our results were not limited by the number of trials. After sorting the distribution, we found that the 68% upper and lower limits on the stellar mass density were 3.3×10^5 $M_\odot$ Mpc^{-3} and 1.2×10^6 $M_\odot$ Mpc^{-3}, respectively.

Summary. Above we derive three different estimates of the stellar mass densities with uncertainties. The estimates are 5.7, 4.5, and $6.6^{+5.4}_{-3.3} \times 10^5$ $M_\odot$ Mpc^{-3}. All these estimates are consistent with each other but we prefer the random M/L approach because this one should be less affected by possible systematic errors in the mass derived from poor photometry. We present this stellar mass density in Figure 2.6 and show the previous determinations of Stark et al. (2009) at $z \sim 4-6$ and Labbé et al. (2006) at $z \sim 7$ for context. We discuss differences between these stellar mass density determinations and the observed trends in Section 2.8 and Section 2.9. We should also note here that allowing moderate extinction ($A_V < 0.5$) produces SMD measurements that are fully consistent with the previous values (within the uncertainties).

2.7.3 SFR Density Determinations

The advantage of the current stellar population modeling is that it permits to estimate the SFR in our candidates at even earlier times. Combining our age constraints with the estimated SMD we can place limits on the SFR density at even earlier times.

In terms of the previous history, the constant SF models imply ages of the galaxies

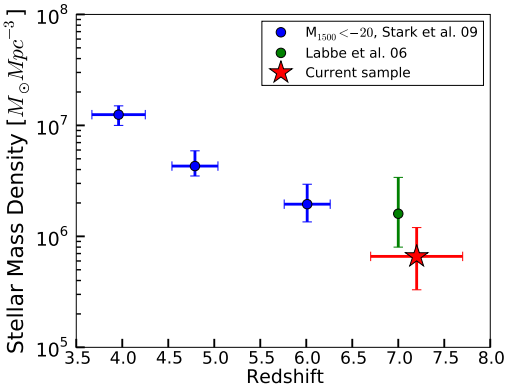

Figure 2.6: The stellar mass density as a function of redshift. Our estimate of the stellar mass density at $z \sim 7$ is shown with the red star and considers the contributions from galaxies with absolute magnitudes $M_{\rm UV,AB} < -20$. The horizontal error bars show the approximate width of our samples in redshift space. Also shown are the stellar mass density determinations of Stark et al. (2009) at $z \sim 4$, $z \sim 5$, and $z \sim 6$ (blue points). The green point at $z \sim 7$ is from Labbé et al. (2006). That estimate was derived from two $z \sim 7$ candidates in the HUDF identified by Bouwens et al. (2004b). Those candidates are also included in this study. The limiting UV luminosity probed by our sample is comparable to the points at lower redshift.

consistent with them being in place at around $z \sim 10$, which combined with their assembled masses imply a very simple estimate of the average SFRD between $7 < z < 10$. The amount of time elapsed corresponds to 300 Myr and the stellar mass assembled in that amount of time is $3.3 \times 10^5\,M_\odot\,{\rm Mpc}^{-3}$. This implies a SFRD of $1.1 \times 10^{-3}\,M_\odot\,{\rm yr}^{-1}\,{\rm Mpc}^{-3}$ (Figure 2.7). An extreme approach that would maximize the SFRD comes from the single burst models. Simply dividing the total masses ($6.6 \times 10^5\,M_\odot\,{\rm Mpc}^{-3}$) by the ages of the sources (80 Myr for the single burst models) yields an average SFRD of $8 \times 10^{-3}\,M_\odot\,{\rm yr}^{-1}\,{\rm Mpc}^{-3}$ in the previous 80 Myr.

2.8 Reliability of Current Results

2.8.1 Comparison with Previous Photometry

In general, our optical to near-IR photometry is consistent with the photometry presented in Bouwens et al. (2010a) although a systematic offset of ~ 0.2 magnitudes is present due to the fact that the fluxes presented there were measured in a somewhat smaller aperture

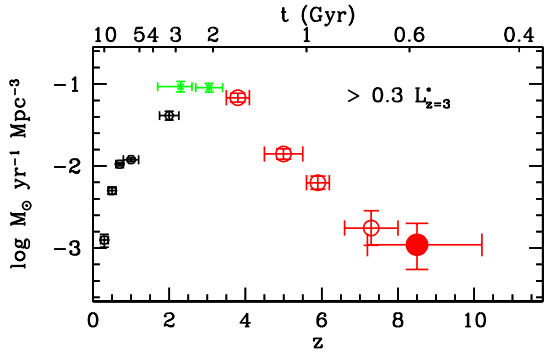

Figure 2.7: The approximate star formation rate density inferred at $z \sim 8.5$ (solid red circle) by combining the age constraints we have on $z \sim 7$ galaxies with the stellar mass density we estimate (Section 2.7.3). For our estimated SFR density, we use the stellar mass density we derive at $z \sim 7$ divided by the average age of our sample. Included on this figure are the dust-corrected SFR density determinations at $z \sim 7$ from $z \sim 7$ z-dropout search (Bouwens et al. 2008: *open red circle*), the Bouwens et al. (2007) determination at $z \sim 4-6$ (*open red circles*), the Reddy & Steidel (2009) determinations at $z \sim 2-3$ (*green crosses*), and the Schiminovich et al. (2005) determinations at $z \lesssim 2$ (*black hexagons*). Dust corrections are as in Bouwens et al. (2010b).

and no aperture corrections were applied. We also find excellent agreement between the mid-IR IRAC fluxes measured for our HUDF z-dropouts and those presented in Labbé et al. (2006). Although this might not be surprising due to our use of the same technique for doing photometry, our modeling of the flux from neighboring sources (and subsequent removal of this flux) is completely independent. This illustrates the robustness of our method for doing photometry. An independent test of the quality of photometry can be obtained by comparing flux measurements for sources with deep IRAC observations taken in both GOODS epochs (rotated by 180 degrees). In general, we observe excellent agreement between the two measurements for the five sources with two epoch data (the four UDF z-dropouts and CDFS-3225-4627) – suggesting that systematics are minimal. The only exception to this is for the 3.6 μm measurement for GNS-zD2, GNS-zD5, and HDFN-3654-1216 where there are bright nearby neighbors.

2.8.2 Comparison with Previous Estimates of the Stellar Mass Density at $z \sim 7$

Previously, Labbé et al. (2006) made an estimate of the stellar mass density at $z \sim 7$ based upon a small (4 galaxy) HUDF z-dropout sample. They estimated a stellar mass density of $1.6^{+1.8}_{-0.8} \times 10^6\, M_\odot\, \mathrm{Mpc}^{-3}$ to $>0.3\ L^*_{z=3}$. Since we adopt a similar limiting luminosity, we can make a direct comparison with the stellar mass density estimated here. We find a fiducial value that is a about half the one estimated by Labbé et al. (2006). This is mostly due to our different choice of star formation histories (we favor constant SF histories versus the average between SSP and constant SFR used in that work). These estimates are fully consistent within the uncertainties.

This quantity was also estimated by Stark et al. (2009) at $z \sim 4-6$ for sources in the GOODS fields to similar depth (see Figure 2.6). A simple calculation shows that the observed growth in mass between $z \sim 7$ and $z \sim 6$ is consistent with the observed SFRD derived from the UV LF studies of Bouwens et al. (2008).

2.8.3 How Significant is Crowding for Current Samples

Because of the broad PSF in IRAC data, crowding is considered to be a potentially significant concern in doing photometry on faint sources, particularly when these sources are nearby bright foreground galaxies. In fact, in many studies, it is thought that perhaps ∼50% of faint sources are sufficiently close to their neighbors that IRAC photometry is impossible. What do we find here?

We attempted to do IRAC photometry on all 11 z-dropouts in the Bouwens et al. (2010a), without excluding any sources due to crowding issues. Of the 11 sources presented here, 5 suffered significant blending with nearby neighbors. However, as a result of our deblending technique (Labbé et al. 2006), we were able to recover reliable fluxes for all 11 in the 4.5 μm

band and 8 of 11 (73%) in the 3.6 μm band (excluding GNS-zD2, GNS-zD5, and HDFN-3654-1216 which showed strong residuals from the neighbors after the subtraction process – implying large systematic errors in those two cases). This agrees with Monte-Carlo experiments that we performed that suggest that photometry is possible for $\gtrsim$80% of faint sources and that the largest errors in the recovered fluxes should be roughly a factor of 2.

2.9 Discussion

2.9.1 Stellar Mass Growth During the First Gyr of the Universe.

Despite the large uncertainties in the derived individual masses, it seems clear now that quite massive ($> 10^{10}$ $M_{\odot}$) systems with evolved stellar populations were already present in the universe at very early times ($z \sim 7$ or at least $z \sim 6$). These very massive systems likely correspond with the most massive Dark Matter Haloes (DMH) and are predicted to exist but in low numbers in the standard Press–Schechter formalism. It can be challenging to probe the high mass end of the mass function since obtaining sufficient statistics on galaxies in this regime requires simulations with large volumes. Davé et al. (2006) ran an SPH simulation with a comoving volume of 10^5 Mpc^3 which they find to be adequate to probe the stellar mass range $10^{7.2} - 10^{10}$ $M_{\odot}$ at $z \sim 7$. At the median mass of our sample of 5×10^9 $M_{\odot}$, they find a number density of $\sim 10^{-4}$ Mpc^{-3}. More recently, Choi & Nagamine (2010), ran a simulation in a larger box of $\sim 3 \times 10^6$ Mpc^3 and find the number density at 5×10^9 $M_{\odot}$ at $z \sim 7$ to be approximately one half that predicted by Davé et al. (2006). Given the uncertainties, these predictions agree quite well with the density of such objects that we find of 1.6×10^{-4} Mpc^{-3}. Although our sample may still suffer from small number statistics, the fact is that such massive objects are found to be fairly common at this early epochs and their moderately evolved SEDs show that their stellar populations are not pristine but were partly formed at higher redshifts.

2.9.2 Star Formation Histories of High-redshift Galaxies.

It is well known that the results (e.g., derived masses, SFRs, etc.) of stellar population analyses can depend significantly on the functional form one assumes for the star formation history. Some care, therefore, needs to be given to the parameterization of these histories to ensure that the conclusions drawn do not depend too much on artifacts of this parameterization.

To illustrate, there are three different model parameterizations of the star formation history in common use in the literature: instantaneous burst models, exponentially decay star formation models, and constant star formation models. Instantaneous burst models give younger ages and lower masses than exponential decay models which in turn give younger ages and lower masses than constant star formation models. The instantaneous burst models do not seem realistic but are useful to set lower limits on the derived ages and masses. Exponential decay models are the most popular in the literature (e.g., Yan et al. 2006, Eyles et al. 2007, Stark et al. 2009) – perhaps because of their versatility in modeling a wide range in star formation histories – but give rise to a troubling prediction, namely, that the star formation rates of galaxies were larger in the past. This prediction is troubling because it contradicts both the observed and predicted trend that the SFR density of the universe increases with cosmic time.

Given these concerns, we prefer to model the stellar population of high-redshift galaxies with constant star formation histories. The reason for this preference is as follows: first, constant star formation models do not naturally predict that the SFR density will be greater at early times, as exponentially decaying models do. Second, constant star formation models do not predict a large population of UV luminous sources at earlier times as found from exponentially-decaying models (e.g., Yan et al. 2006). This is more consistent with the observation that such sources are not found in large numbers at $z \sim 7$. Third, constant star formation models are more consistent with the low evolution seen in the specific star formation rate (e.g., Figure 2.5 here, Section 2.6.2, and as discussed by Stark et al. 2009). We realize that *some* luminous galaxies

may have mass-to-light ratios suggesting their SFRs were higher in the past, but we suspect this may be a duty cycle issue that is due to feedback, etc. These galaxies are simply experiencing a period where their SFRs are less than their norm.

2.9.3 Reionization

As outlined in Section 2.7.3, the stellar population modeling we do of $z \sim 7$ galaxy candidates allow us to estimate the SFR density at even earlier times. Having an estimate of this SFR density is valuable since it allows us to assess how much ionizing radiation the star-forming population at $z \gtrsim 7$ might likely produce – and hence repose the question about whether z$\gtrsim$6 galaxies are capable of keeping the universe reionized. From absorption studies to bright $z \sim 6$ QSOs, the process of reionizing the hydrogen of the universe was just ending at $z \sim 6$ (Fan et al. 2006, Becker et al. 2001) while the five year WMAP results suggest it began at least as early as $z \sim 11$ (Komatsu et al. 2009).

Madau et al. (1999) presented a prescription to estimate the critical density of UV radiation necessary to reionize the universe at a given redshift. Updated to a more current cosmology (Komatsu et al. 2009), that formula becomes:

$$\rho_{SFR}^{crit}(z) \approx \frac{0.04}{f_{esc}} \left(\frac{1+z}{8}\right)^3 \left(\frac{C}{30}\right) \left(\frac{\Omega_b\ h_{70}^2}{0.0463}\right)^2 M_\odot\ \mathrm{yr}^{-1}\ \mathrm{Mpc}^{-3}. \quad (2.1)$$

At $z = 7$, for an escape fraction $f_{esc} = 0.1$ (e.g. Shapley et al. 2006), and for a clumping factor $C = 30$ (but see Pawlik et al. 2009 who suggest $C \sim 6$) the value of of $\rho_{SFR}^{crit} = 0.4\ M_\odot\ \mathrm{yr}^{-1}\ \mathrm{Mpc}^{-3}$. The sources capable of producing such radiation remain unknown, but young O and B stars in early galaxies stand out as the most likely candidates given the observed decrease in the number density of quasars at high redshifts.

Based upon the stellar mass density and the mean ages we derive in Section 2.6 and Section 2.7 for the sample, we estimated an average SFR density of 0.0011 $M_\odot\ \mathrm{yr}^{-1}\ \mathrm{Mpc}^{-3}$ between $7 < z < 10$ (Section 7.3). This is more than 2 orders of magnitude below the SFR

Table 2.4: Key Results Derived from $z \sim 7$ Sample

Quantity	Value
Redshifts	7.2 ± 0.5
Masses	0.1-12$\times 10^9$ $M_\odot$
$M/L_{\rm UV}$ ratio	0.01-0.1 $M_\odot/L_\odot$
Minimum Age[a]	80 Myr
Average Age	300 Myr
UV-continuum Slope β	-2.4 ± 0.4
sSFR	2.4 ± 0.6 Gyr^{-1}
Mass density (direct)	5.7×10^5 $M_\odot$ Mpc^{-3}
Mass density (M/L of Mean SED)	4.5×10^5 $M_\odot$ Mpc^{-3}
Mass density (Random M/L)[b]	$6.6^{+5.4}_{-3.3} \times 10^5$ $M_\odot$ Mpc^{-3}
Predicted SFR density (at $z = 9$)	0.0011 $M_\odot$ yr^{-1}Mpc^{-3}
M/L_V (sed)	0.19

Notes.

[a] From single burst models.

[b] Our best estimate.

density required to reionize the universe at $z = 7$. We can also obtain an upper limit to the SFR density by considering the minimal ages obtained from the single burst models. The mean age of 80 Myr obtained from these models implies a SFR density of 0.008 $M_\odot$ yr^{-1} Mpc^{-3} at $z = 8$ (Section 2.7.3). Even for this larger value for the SFR density, we are still a factor ~ 50 below that required to reionize the universe. Of course, these values are based only on the brightest observable sources and so including the mass from galaxies of even lower luminosities than our selection limit would increase these numbers by a factor of $\gtrsim 2-3$. In any case, it bears mention that we cannot include the contribution from a population of dust obscured sources that we would miss in LBG selections. However, as we have already noted in Section 2.6.1 and Section 2.6.2 there is strong evidence that the contribution from this population is not large (e.g., Bouwens et al. 2009).

2.10 Summary

We use the very deep optical, near-IR, and IRAC data over and around the two GOODS fields to study the properties of a large sample of $\sim$11 z-dropout galaxies at $z \sim 7$. Considered

are the ages, stellar masses, redshifts, and dust properties of $z \sim 7$ galaxies. The z-dropout candidates were drawn from the very large selection of such galaxies from $\sim$80 arcmin^2 of deep NICMOS data by (Bouwens et al. 2010a). Essential to this analysis is the availability of deep *Spitzer*/IRAC mid-IR data that give us deep coverage of these sources at rest-frame optical wavelengths and hence permit us to estimate the stellar mass. The stellar population modeling was performed with the Bruzual & Charlot (2003) spectral synthesis modeling code with a Salpeter IMF and assuming solar metallicity. We have quantified how our best-fit properties would change as a function of the assumed IMF and metallicity.

Our conclusions are as follows:

- Photometric redshifts place the candidates at $6.2 < z < 8.0$ with the mean redshift of the sample at 7.2. The uncertainties in the redshift for individual candidates are typically $\Delta z \sim 0.5$ and have been taken into account in the derivation of the confidence intervals for the rest of the properties (see Section 2.5 and Figure 2.2).

- We use the results of of Bouwens et al. (2009) regarding the low extinctions expected at high redshifts to help us better constrain the individual ages of the sources. Our CSF model fits yield SFRs that are consistent with simple conversion based on the L_{1500} luminosities. The best-fit ages allow enough time to assemble their masses by the redshift of observation. This does not seem to be the case for the most massive sources in the work by Yan et al. (2006). We argue that this is not likely an effect of large extinctions but rather that these sources are the result of some other more complicated history probably involving mergers (Section 2.9.2).

- The star formation history weighted ages of the observed stellar population we derive are in the range of $170 - 420$ Myr with a mean of 300 Myr (there is an outlier with ~ 20 Myr). These ages are consistent with previous works that place the formation of the most massive galaxies at very early epochs. In particular, the bulk of the stars in some of these

sources seem to have formed as early as $z \sim 10$ (see Section 2.6 and Table 2.3).

- The stellar masses we estimate for individual $z \sim 7$ z-dropouts in our sample range from 0.2×10^9 $M_\odot$ to 12×10^9 $M_\odot$, with a mean for the sample of 5.1×10^9 $M_\odot$. The masses we estimate are much more well constrained than other quantities – like the age – but are nevertheless still uncertain at the factor of 2 level (Section 2.6 and Table 2.3).

- We find that the specific SFRs (SFR/Mass) of the sources in the sample range from 1.8 Gyr^{-1} to 25 Gyr^{-1}, with a biweight mean value of 2.4±0.6 Gyr^{-1}. We observe that at comparable masses, the specific SFR is surprisingly close to all the values in the literature between $z \sim 2$ and $z \sim 6$ (Reddy et al. 2006, Papovich et al. 2001, Daddi et al. 2007, Stark et al. 2009). The constancy of this quantity between $z \sim 2 - 7$, in contrast with its fast decline at $z \lesssim 2$ (Noeske et al. 2007), suggests that star formation proceeds in different ways in these two regimes (see Section 2.6.3 and Figure 2.5).

- Utilizing the estimated selection volumes for the Bouwens et al. (2010a) z-dropout search, we derive the stellar mass density at $z = 7$ using an approach that randomly samples the M/L of the galaxies with the most reliable IRAC photometry. We find $6.6^{+5.4}_{-3.3} \times 10^5$ $M_\odot$ Mpc^{-3}. The random M/L approach is preferred as it is less affected by possible systematic errors in photometry. We tested other approaches, including averaging the direct fits, yielding very similar answers. Our estimate of the global stellar mass assembled is consistent with the growth expected based on the SFRD measured between $6 < z < 7$ and the SMD measured to similar depths at $z \sim 6$ (Section 2.7.2).

- Combining the estimated ages and total assembled mass we can derive an average SFR between $z \sim 10$ and $z \sim 7$ of 1.1×10^{-3} $M_\odot$ yr^{-1} Mpc^{-3}. SSP models provide us with minimum age estimates that in combination with the masses allow us to place an upper limit to the SFRD at $z \sim 8$. This estimate is still a factor 50 below the necessary value to reionize the universe at this redshift (following the Madau et al. 1999 prescription with

$f_{esc} = 0.1$ and $C = 30$, eq. 1), in agreement with previous works. We emphasize that this estimate is only based on the most luminous sources and is probably missing most of the UV light, which is being produced by sources in the faint end of the LF (e.g., Bouwens et al. 2007, Reddy & Steidel 2009, Yan & Windhorst 2004).

The Bouwens et al. (2010a) search based on a large area of high quality optical to NIR data has provided us with the first sizable sample of candidate sources at $z \sim$7, a step of 200 Myr with respect to the previous efforts (but see also new work by Oesch et al. 2010b, Bouwens et al. 2010b, McLure et al. 2010, Bunker et al. 2010, Ouchi et al. 2009). By complementing these data with very deep mid-IR *Spitzer*/IRAC imaging, we have been able to fit BC03 SSP models to estimate the masses and ages of galaxies at $z \sim 7$. Our results suggest that these galaxies had been forming stars for $\gtrsim$ 200 Myr and as soon as $z \sim 9 - 10$, well into the reionization epoch. We expect to substantially improve upon these results taking advantage of the deep near-IR data soon to become available over the HUDF and CDF-South GOODS field as a result of the new WFC3 instrument on*HST*. Not only will we substantially increase the number of $z \sim 7 - 8$ galaxies known, but the deeper data and improved set of near-IR filters (Y, J, H) will enable us to perform much more accurate stellar population modeling on individual sources.

Chapter 3

Star Formation Rates and Stellar Masses of $z = 7 - 8$ Galaxies from IRAC Observations of the WFC3/IR ERS and the HUDF Fields

3.1 Introduction

Until recently, only a modest number of relatively bright $z \gtrsim 7$ galaxies were known, mostly from wide-area NICMOS (Bouwens et al. 2008, Oesch et al. 2009; R. J. Bouwens et al. in preparation) and ground-based searches(Ouchi et al. 2009, Castellano et al. 2010a, Hickey et al. 2010). The arrival of WFC3/IR aboard *H*ubble Space Telescope (*HST*) has

dramatically improved the situation by identifying large numbers of $z \gtrsim 7$ galaxies by their redshifted UV light. Here we report on $z \gtrsim 7$ galaxies selected from the WFC3/IR Early Release Science (ERS) observations over the GOODS-South field (Wilkins et al. 2010, Bouwens et al. 2011c), complemented with candidates from the recent ultradeep survey with WFC3/IR over the HUDF09 field (Oesch et al. 2010b, Bouwens et al. 2010b; see also McLure et al. 2010, Bunker et al. 2010, Yan et al. 2010).

Little is known about the stellar masses, metal production, and the contribution of star formation to reionization in these galaxies. Mid-infrared observations with the InfraRed Array Camera (IRAC; Fazio et al. 2004) on *Spitzer* constrain the stellar masses and ages, which has led to the surprising discovery of quite massive $\sim 10^{10} M_{\odot}$ galaxies at $z \gtrsim 6$ (Eyles et al. 2005, Yan et al. 2006, Stark et al. 2009) and appreciable ages ($200 - 300$Myr) and M/Ls as early as $z \sim 7$ (Egami et al. 2005, Labbé et al. 2006, González et al. 2010). The overall results suggest the galaxies formed substantial amounts of stars at even earlier times, well into the epoch of reionization (Stark et al. 2007b, Yan et al. 2006, Labbé et al. 2010b).

In this Letter, we study the stellar populations of the largest sample of $z \gtrsim 7$ galaxies with IRAC measurements to date, focusing on correlations with luminosity and stellar mass, and implications for the mass density at $z \sim 8$. We adopt an $\Omega_M = 0.3, \Omega_\Lambda = 0.7$ cosmology with $H_0 = 70$ km s^{-1}Mpc^{-1}. Magnitudes are in the AB photometric system (Oke & Gunn 1983).

3.2 Observations and Stellar Population Modeling

Our sample consists of sources derived from the ultradeep WFC3/IR HUDF, the deep WFC3/IR ERS, and wide-area NICMOS over the CDF-S and CDF-N. Candidates were selected using the $z \sim 7$ $z_{850}-$dropouts and $z \sim 8$ $Y_{098}-$dropouts, as used in Oesch et al. (2010b), Bouwens et al. (2010c), and González et al. (2010) (see also R. J. Bouwens et al. in preparation).

We now briefly discuss the IRAC photometry from the new ERS sample.

The Spitzer/IRAC data over the WFC3/ERS area in the CDF-S ($\approx$ 23.3 hours integration time) were obtained from the Great Observatories Origins Deep Survey (GOODS; M. Dickinson et al. in preparation)[1]. The IRAC depths in the 3.6 and 4.5 bands are 27.1 and 26.5 magnitude (1σ, total, point source), respectively. Obtaining reliable IRAC fluxes of the candidates is challenging because of the contamination from the extended PSF wings of nearby foreground sources. We remove contaminating flux by modeling the candidates and nearby sources using their isolated flux profiles and positions in the deep WFC3/IR maps as templates. We convolve the templates to match the IRAC PSF, simultaneously fit them to the IRAC map leaving only the fluxes as free parameters, and subtract the best-fit models to the foreground sources (see Labbé et al. 2006, Wuyts et al. 2007, González et al. 2010, de Santis et al. 2007). After cleaning the IRAC images, we perform conventional aperture photometry in the 3.6 and 4.5 bands in $2\farcs5$ diameter apertures on 15 of the original 18 $z_{850}-$dropout galaxies over the WFC3/IR ERS. Three were too close to bright sources for reliable measurement. Fluxes were corrected by a factor $\times 1.8$ to account for light outside the aperture (consistent with point source profiles). Six of the 15 galaxies are undetected in IRAC ([3.6] $<$ 26.5,2σ). Errors include the uncertainty in the best-fit confusion correction, added in quadrature.

We complete the sample with 21 $z \sim 7$ galaxies with IRAC measurements from the HUDF (Oesch et al. 2010b, Labbé et al. 2010b) and from the recent wide-area NICMOS search Bouwens et al. (2010a), González et al. (2010). The total sample consists of 36 $z \sim 7$ galaxies spanning 4 magnitudes in H_{160}. To investigate trends with magnitude, we stacked the flux densities of the galaxies in three $\sim 1-$magnitude bins centered on $H_{160} \approx 26, 27$ and 28, containing 11, 15, and 10 galaxies respectively. The uncertainties are determined by bootstrapping. Stacking increases the SNR, in particular for faint galaxies, where the uncertainty in the mass is driven by the SNR in IRAC (see Labbé et al. 2010b).

[1]This paper uses data release DR2 of epoch 2, available from http://data.spitzer.caltech.edu/popular/goods/

We derive stellar masses and redshifts by fitting stellar population synthesis models to the average SED fluxes using the χ^2-fitting code FAST (Kriek et al. 2009). We adopt Bruzual & Charlot (2003; BC03) models with a Salpeter (1955) initial mass function (IMF) between $0.1 - 100\ M_{\odot}$. We explore several SFHs and the effects of metallicity and dust. The differences with more recent models (e.g., Maraston 2005, Charlot & Bruzual, in preparation) are small and will not be considered in detail (see Labbé et al. 2010b). We fit models smoothed to a resolution of 100 Å rest-frame, corresponding to the approximate width of the dropout selection windows. Adopting a Kroupa (2001) IMF reduces the stellar masses and SFRs by 0.2 dex but does not change other parameters or the quality of fit. The typical uncertainties in the derived average stellar masses, SFRs, age, and A_V for the stacked SEDs are 0.15 dex, 0.25 dex, 0.3 dex, and 0.1 mag, respectively. The photometry and best-fit model parameters are presented in Table 3.1.

3.3 Stellar populations and Star Formation Histories at $z \sim 7$

Figure 1 (*left panel*) shows the broadband SEDs of the $z \sim 7$ $z_{850}-$dropout galaxies in the three magnitude bins, with the best-fit BC03 stellar population models. The overall SED shapes are remarkably similar, with a pronounced jump between H_{160} and [3.6] (or rest-frame $(U - V) \approx 0.5$) indicative of a modest Balmer break and evolved stellar populations (> 100Myr). Focusing on the far-UV continuum, we find the slope $f_\lambda \propto \lambda^\beta$ (traced by the $J_{125} - H_{160}$ color) to be very blue, and decreasing from $\beta \sim -2$ at $H_{160} \sim 26$ to $\beta \sim -3.0$ at $H_{160} \sim 28$. As discussed by Bouwens et al. (2010c), such extremely blue slopes require low dust content $A_V < 0.1$, very low metallicities and/or very young ages. Small 0.04 mag changes in the WFC3/IR zeropoints (e.g., McLure et al. (2010)) would cause changes of $\beta \approx 0.17$, comparable to the random uncertainties. The red $H_{160} - [3.6]$ color, however, implies more evolved stellar populations (> 100Myr), leaving the models seemingly unable to match the entire SED.

Table 3.1: Summary of Photometry and Modeling of $z \sim 7-8$ Dropout Galaxies

SEDs of $z \sim 7$ z_{850}-dropouts										
Object	B_{435}	V_{606}	i_{775}	z_{850}	Y	J_{125}	H_{160}	K	[3.6]	[4.5]
ERS-2056344288	4.0(7.1)	1.2(5.0)	6.8(8.6)	13.5(9)	40.9(11)	48.6(8)	61.3(10)	—(—)	223.1(51)	134.7(89)
ERS-2068244221	-1.6(6.9)	2.4(5.5)	4.6(9.4)	26.4(10)	80.5(11)	78.3(15)	56.4(10)	—(—)	158.8(51)	-5.5(89)
ERS-2111644168	6.8(6.2)	1.5(4.7)	7.4(7.5)	4.9(8)	20.1(8)	54.8(10)	43.1(8)	—(—)	142.8(83)	-54.0(89)
ERS-2150242362	6.1(8.5)	0.9(7.5)	-3.5(12.5)	14.3(15)	33.4(15)	49.0(10)	68.7(14)	—(—)	154.4(58)	98.9(106)
ERS-2150943417	5.2(6.7)	4.7(6.0)	4.4(9.9)	9.2(12)	34.4(16)	87.7(17)	79.7(15)	—(—)	132.4(63)	197.3(120)
ERS-2154043286	-0.1(5.0)	-1.4(4.3)	4.8(7.4)	17.7(8)	45.3(9)	45.0(11)	36.5(9)	—(—)	11.5(62)	-13.5(100)
ERS-2160041591	-6.0(9.9)	-12.8(7.9)	4.7(13.5)	24.2(16)	68.2(15)	89.8(16)	74.7(14)	—(—)	271.0(87)	293.9(134)
ERS-2161941498	-0.8(7.1)	-1.4(5.7)	-3.2(9.8)	8.4(12)	25.7(10)	42.9(10)	41.6(10)	—(—)	64.4(51)	83.2(89)
ERS-2202443342	7.2(8.8)	-3.0(7.2)	5.6(10.3)	25.4(11)	42.5(11)	55.2(12)	50.4(11)	—(—)	145.9(51)	111.1(89)
ERS-2225241173	1.8(5.6)	-2.0(4.4)	-11.2(7.6)	15.3(8)	37.7(9)	40.6(8)	43.1(8)	—(—)	89.0(51)	128.2(89)
ERS-2226543006	-2.5(9.8)	-8.7(7.6)	7.8(12.5)	48.6(14)	113.3(15)	125.1(9)	182.5(13)	—(—)	462.9(94)	276.5(152)
ERS-2229344099	-0.6(8.3)	-0.6(7.0)	6.2(10.3)	18.8(11)	49.8(13)	47.0(8)	64.4(11)	—(—)	216.3(51)	110.8(89)
ERS-2295342044	-0.2(7.8)	1.4(5.7)	3.7(10.2)	14.5(12)	54.8(13)	70.9(13)	67.1(12)	—(—)	124.7(51)	82.3(89)
ERS-2352941047	-3.7(6.0)	4.1(4.6)	4.9(7.6)	8.6(9)	19.7(7)	28.9(6)	31.9(7)	—(—)	34.4(51)	54.4(89)
ERS-2354442550	3.7(6.2)	-0.7(4.6)	0.7(7.9)	15.1(9)	46.7(12)	117.4(12)	106.5(11)	—(—)	317.6(53)	21.5(101)
$25 < H_{160} < 26.5$	-3.2(2.3)	2.8(2.3)	-7.4(4.7)	23.5(5.4)	63.7(7.7)	129.7(16)	128.2(17)	101(12)	262(28)	181(37)
$26.5 < H_{160} < 27.5$	-2.4(0.8)	-0.8(0.6)	2.2(1.8)	14.6(2.3)	49.1(4.3)	64.8(4.1)	57.0(3.4)	24.5(24)	107(16)	83.8(25)
$H_{160} > 27.5$	1.2(0.8)	0.4(0.5)	-0.1(0.7)	5.6(1.1)	27.2(1.8)	29.6(2.0)	24.5(1.6)	22.9(14)	45.1(9.5)	39.3(17)
SEDs of $z \sim 8$ Y_{098}-dropouts										
	B_{435}	V_{606}	i_{775}	z_{850}	Y_{098}	J_{125}	H_{160}	K	[3.6]	[4.5]
ERSy-2354441327	-2.5(6.1)	-2.3(4.7)	-1.4(7.6)	-8.3(9)	1.6(8)	40.7(8)	37.3(7)	—(—)	29.9(52)	61.7(89)
ERSy-2376440061	-4.7(8.3)	2.6(5.5)	0.8(10.6)	15.0(11)	6.2(13)	46.5(12)	49.2(13)	—(—)	134.1(51)	143.6(89)
ERSy-2251641574	0.4(9.4)	-3.5(6.0)	2.1(9.9)	9.3(11)	5.9(14)	59.3(11)	69.6(13)	—(—)	103.1(51)	38.9(89)
$H_{160} \sim 27$	-1.9(4.6)	-1.3(3.1)	0.9(5.4)	6.9(6)	5.0(7)	50.8(6)	55.5(6)	—(—)	95.4(26)	77.4(49)

Average colors of $z \sim 7$ z_{850}-dropouts				SFRs and stellar masses of $z \sim 7$ z_{850}-dropouts			
	H_{160} [AB mag]	$J_{125}-H_{160}$ (AB mag)	$H_{160}-[3.6]$ (AB mag)		SFR$_{1500}$ ($M_\odot$ yr^{-1})	M^* ($M_\odot$)	sSFR (yr^{-1})
$25 < H_{160} < 26.6$	26.13(0.14)	0.03(0.06)	0.89(0.19)	$\log$SFR > 1.0	$1.17^{+0.05}_{+0.04}$	$9.92^{+0.06}_{+0.11}$	$-8.75^{+0.14}_{-0.08}$
$26.6 < H_{160} < 27.5$	26.98(0.05)	-0.09(0.06)	0.78(0.17)	$1.0 < \log$SFR < 0.6	$0.85^{+0.02}_{-0.02}$	$9.55^{+0.08}_{-0.07}$	$-8.70^{+0.12}_{-0.09}$
$H_{160} > 27.5$	27.92(0.10)	-0.20(0.05)	0.59(0.28)	$\log$SFR < 0.6	$0.39^{+0.05}_{-0.07}$	$9.08^{+0.12}_{-0.30}$	$-8.70^{+0.11}_{-0.07}$

Notes. The optical–to–near-IR fluxes are measured in 0.″4 diameter apertures. Spitzer/IRAC fluxes are measured on the confusion-corrected maps in 2.″5 diameter apertures. Fluxes are corrected to total assuming point source profiles. Units are nanoJy for the SEDs and AB magnitudes for the average colors. The total sample consists of 15 new sources from the WFC3/ERS sample (Bouwens et al., in preparation), 9 sources from the NICMOS sample (UDF-1417,964,GNS-1,2,3,4,5,CDFS-4627,HDFN-1216; Gonzalez et al. 2010), and 12 from the WFC3/UDF sample (UDFz-4471,4257,3955, 3958,3722,4314,3677,3744,4056,3638,3973,3853; Oesch et al. 2010, Labbé et al. 2010). The stacked $Y-$band of the $z \sim 7$ galaxies is a combination of the Y_{105} and Y_{098} bands. SFR$_{1500}$ is the SFR derived from the 1500 Å monochromatic luminosity using the prescription of Madau et al. (1998) and corrected for dust using the best-fit A_V (mean $< A_V >= 0.13$ mag). The stellar masses are based on BC03 $0.2\,Z_\odot$ models using exponentially declining SFHs with $8 < \log\tau < 11$ and reddening $A_V < 0.3$. Uncertainties are determined by bootstrapping.

To explore the mismatch further we consider in more detail the effects of metallicity, SFH, and nebular emission. Fig. 1 (*right panel*) shows the $J_{125}-H_{160}$ versus $H_{160}-[3.6]$ colors of the observed stacked SEDs. The lines show predictions of 0.2 $Z_\odot$ BC03 models for various continuous SFHs (rising, constant, declining). Generally, evolved models are able to reproduce the joint $J_{125}-H_{160}$ versus $H_{160}-[3.6]$ colors of the more luminous $z=7$ galaxies, but not the colors of the faintest, bluest galaxies. The arrows show the effect of changes in model assumptions, which we will discuss now:

1) Metallicities: Low metallicities (e.g., 0.2 $Z_\odot$) do a decent job of producing much bluer β than Solar at a given $H_{160}-[3.6]$ color. Very low metallicities (1/50 Solar) produce

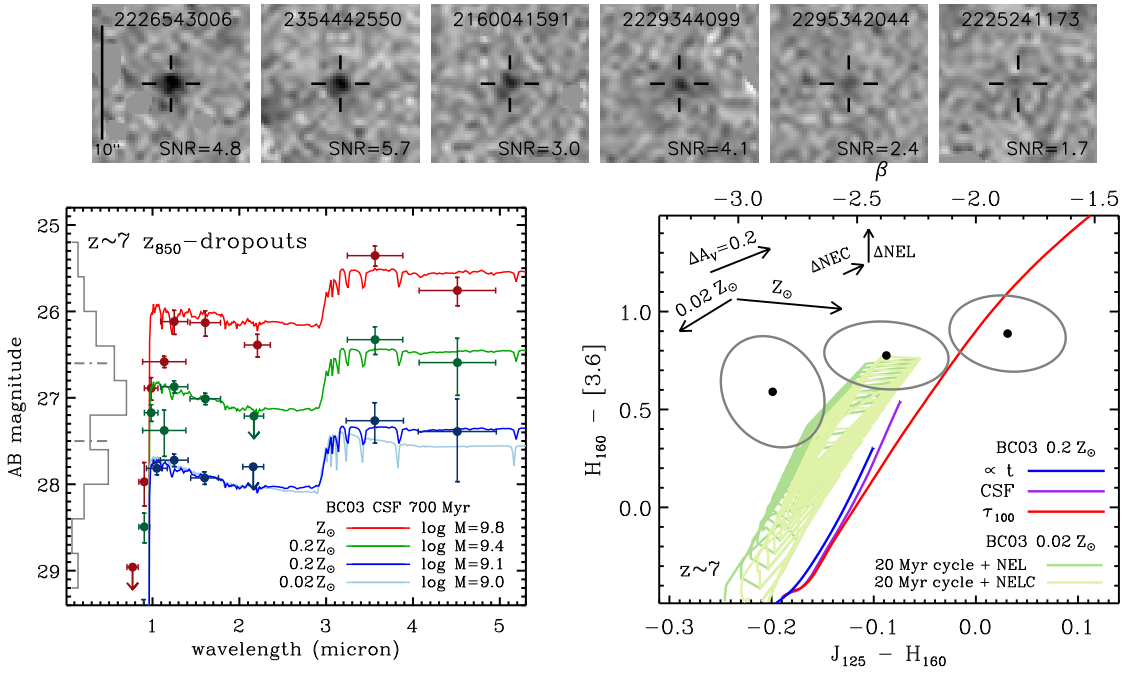

Figure 3.1: (*Top panels*) Representative IRAC [3.6] image stamps of WFC3/ERS $z \sim 7$ $z_{850}-$dropouts (sorted by magnitude) after subtracting neighbors. Brighter sources may have lower SNR after accounting for confusion. (*left panel*) Stacked broadband SEDs from the combined NICMOS, WFC3/UDF and WFC3/ERS samples, averaged in $\sim 1-$mag bins centered on $H_{160} \approx 26, 27$ and 28. The data include *HST*/ACS, NICMOS, and WFC3/IR, groundbased K, and IRAC [3.6] and [4.5]. Upper limits are 2σ. ACS optical measurements are non-detections fainter than 29.4 mag. The gray histogram shows the H_{160}-band magnitude distribution (the peak is 9 sources). The best-fit BC03 stellar population models at $z = 6.9$ are shown. The overall SED shapes are similar with a break between H_{160} and [3.6], expected for evolved stellar populations (> 100Myr). The far-UV slope (traced by $J_{125} - H_{160}$) bluens towards fainter H_{160} magnitude (as found Bouwens et al. 2010c). (*right panel*) Comparison of the observed average $J_{125} - H_{160}$ versus $H_{160} - [3.6]$ color (*filled circles*) with predictions of 0.2 $Z_\odot$ BC03 models for various SFHs (*solid lines*). Ellipsoids show 1σ uncertainties. The SFHs are linearly increasing with time (*blue*), CSF (*purple*), episodic (*light green*) with a 50% dutycyle and 40Myr duration, and exponentially declining (*red*) with $\tau = 100$Myr. Also shown are the effects on the model colors of metallicity, reddening (Calzetti et al. 2000), nebular continuum emission (NEC) (Schaerer 2002), and line emission (NEL) (Erb et al. 2006a, Brinchmann et al. 2008). The episodic model is shown twice, once only with the effect of line emission (+ NEL) and once with both line and nebular continuum emission (+ NELC). The lines terminate at 750 Myr.

even bluer β's, but also bluen $H_{160} - 3.6$. Metallicity alone appears not enough to fully resolve the discrepancy.

2) Nebular Emission: Nebular emission lines (NEL) likely contribute to the IRAC fluxes, reddening the $H_{160} - [3.6]$ color. Empirical estimates of [OIII]5007 emission at $z > 2$ are scarce, but we can infer the possible effect from the observed strength of Hα at $z \sim 2.2$ (Erb et al. 2006a). Assuming $\mathrm{W}_{\mathrm{H}\alpha} = 200$Å and $\mathrm{W}_{[\mathrm{OIII}]4959,5007+\mathrm{H}\beta} = 2.5 \times W_{\mathrm{H}\alpha}$, appropriate for 0.2 $Z_{\odot}$ galaxies at $z > 2$ (Erb et al. 2006a, Brinchmann et al. 2008), and adopting a redshift distribution of $z = 6.9 \pm 0.5$ (Oesch et al. 2010b) we calculate a contribution of 0.18 mag to [3.6] and 0.14 mag at [4.5] (see Fig 1). Note however, that no measurements of nebular lines at $z \sim 7$ exist. A second possible effect is nebular continuum emission (NEC), which would cause a reddening of both β and $H_{160} - [3.6]$ (shown are the models of Schaerer 2002 with $Z = 1/50\ Z_{\odot}$, $t = 300$ Myr CSF, and 0% escape fraction). Both would reduce the discrepancy between models and data by allowing the models to extend to redder $H_{160} - [3.6]$ at a given β. Note that the extremely blue β may require high escape fractions $f_{esc} \gtrsim 0.3$ (e.g., Bouwens et al. 2010c), which would reduce the contribution of nebular emission.

3) Star Formation Histories: Declining SFHs can match the colors of the most luminous, redder galaxies, but their far-UV continua are too red for lower luminosity galaxies. In contrast, strongly rising SFRs (SFR$\propto\ t^{\alpha}$, $\alpha > 1$) exhibit blue β but never reach red $H_{160} - [3.6]$ in a Hubble time ($z = 7$) and are formally excluded at 95% confidence. CSF is a compromise, providing red $H_{160} - [3.6]$ colors generated by on-going assembly of stellar mass, and blue far-UV continua from on-going star formation. Finally, episodic SFH with a 50% duty cyle and 40 Myr duration (i.e., 20 Myr "on", 20 Myr "off") is found to have an interesting mix of properties. The luminous active phase of the cycle produces a bluer far-UV continuum for a given $H_{160} - [3.6]$ color than CSF. The reverse is true in the dimmer passive state. The net result for a steep UV LF function is that the luminosity weighted average of cycling galaxies displays bluer far-UV at a given $H_{160} - 3.6$ than CSF, also reducing the discrepancy.

In summary, the model colors match the observations of luminous $z \sim 7$ galaxies reasonably except for the lowest luminosity galaxies, where the blue $\beta \sim -3$ and the red $H_{160} - [3.6] \sim 0.6$ colors remain challenging to fit. Low metallicity CSF models come close, but a contribution from nebular line emission to the [3.6]−band and/or episodic SFHs is likely needed to resolve the mismatch.

3.4 Star Formation Rate versus Stellar Mass at $z \sim 7$

Independent constraints on the SFHs can be obtained from the relation between SFR and stellar mass, as shown in Figure 3.2. The SFRs are calculated from the monochromatic 1500 Å luminosity following the prescription of Madau et al. (1998) and corrected for dust using the best-fit A_V. The galaxies are grouped in bins of SFR (or M_{1500}) centered on $\log \mathrm{SFR} \approx 0.4, 0.8, 1.2$.

The stellar masses of our $z \sim 7$ sample correlate strongly with SFR, producing $\log M^* = 8.70(\pm 0.09) + 1.06(\pm 0.10) \log \mathrm{SFR}$ and corresponding to a constant $M/L_V \approx 0.20$.[2] The derived stellar mass with emission lines (see Section 3.3) would be lower by ≈ 0.17 dex. The scatter around the relation is fairly low ≈ 0.3 dex, but that does not exclude significant short-term SFR variation, e.g., the episodic model (Section 3.3) predicts $\log M^* = 8.45 + 1.0 \log \mathrm{SFR}_{1500}$ and a scatter of ~ 0.3 dex. We find no galaxies with SFRs much lower or higher than the past averaged SFR (i.e., strongly bursting or suppressed. Such galaxies would have satisfied our dropout criteria and would lie in the upper left or lower right corner in Fig. 2. Their absence suggests that that the typical star formation timescales are probably a substantial fraction of the Hubble time. Instead we find that only 4/22 sources with $\log \mathrm{SFR} > 0.7$ are undetected at [3.6] and no galaxies in the sample have SFRs substantially less than M^*/t_{Hubble}.

To illustrate the diagnostic power of the $M^* - \mathrm{SFR}$ diagram, we show in the inset in

[2]The M/L also be calculated from the individual galaxies, yielding the same answer (González et al. 2010).

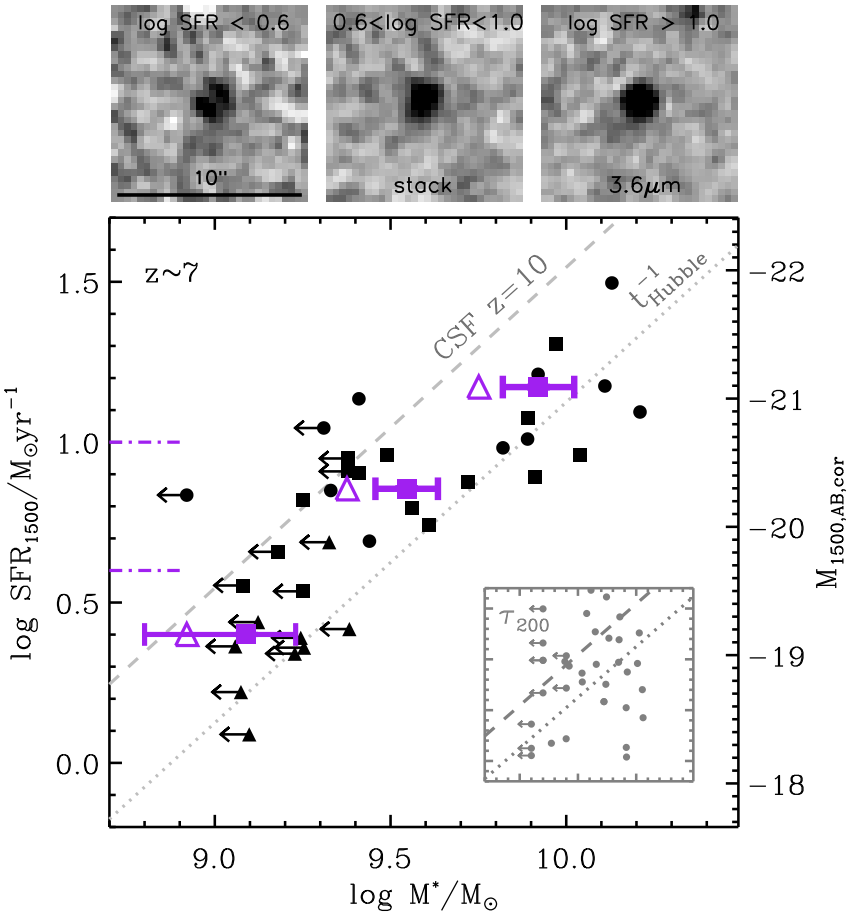

Figure 3.2: Average UV-derived, dust-corrected SFR versus stellar mass for $z \sim 7$ galaxies. Black symbols denote galaxies from the NICMOS (*circles*), WFC3/IR ERS (*squares*) and WFC3/IR HUDF sample (*trangles*). The purple squares show the average stellar mass in bins of SFR centered on $\log \mathrm{SFR} \approx 0.4, 0.8, 1.2$. The purple triangles assume ≈ 0.2 and 0.15 mag contribution by emission lines to the [3.6] and [4.5] bands. The scatter in M^* in bins of M_{1500} is ~ 0.3 dex. The diagonal lines show the maximum stellar mass CSF stellar population that can form in a Hubble time (*dotted*) or since $z = 10$ (*dashed*). Galaxies with strongly increasing/declining SFRs would lie well above/below the lines, respectively, but few such systems are found. The inset shows simulated galaxies with random formation times and exponentially declining $\tau = 200$ Myr SFHs, showing a different distribution with larger scatter. (*Top panels*) Stacked images in the [3.6] band in bins of SFR.

Fig. 2 a simulation of galaxies with random formation times and exponentially declining SFRs ($\tau = 200$ Myr) to the same selection limits as our observed sample. The distribution is clearly different, with no correlation between M^* and SFR, suggesting that star formation timescales for $z \sim 7$ galaxies are probably longer than that.

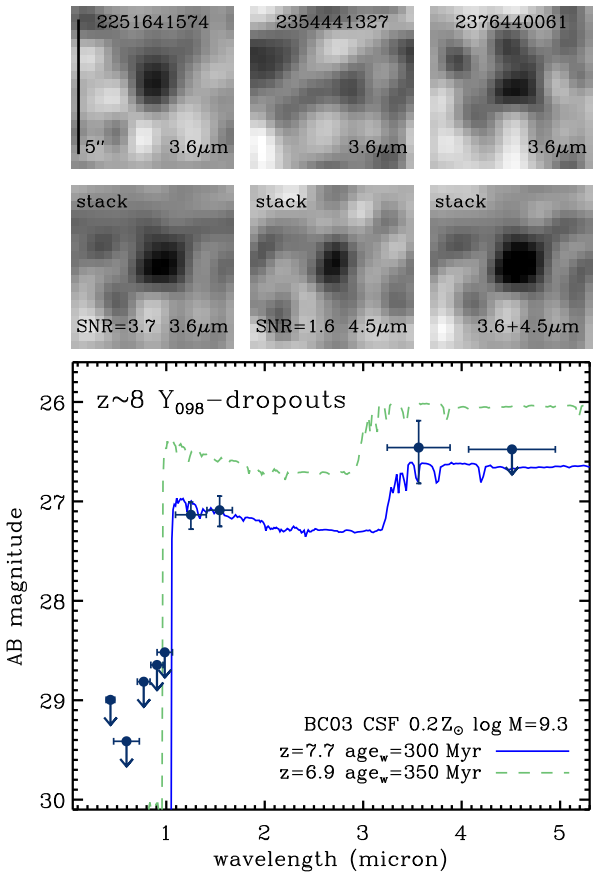

Figure 3.3: (*top panels*) Individual and stacked images of the 3 $z \sim 8$ $Y_{098}-$dropout galaxies in our WFC3/ERS sample, shown in inverted grayscale. Two of the 3 sources are individually detected in the IRAC [3.6]−band. (*bottom panel*) The average broadband SED of the 3 $z \sim 8$ galaxies and the best-fit stellar population model (*solid blue line*). For comparison, we show the best-fit model to $z = 6.9$ z_{850} dropouts of similar H_{160} magnitude (*dashed green line*), shifted by -0.5 mag. The overall shapes are similar, with the $z \sim 8$ galaxies being slightly bluer in $H_{160} - [3.6]$ compared to $z \sim 7$ galaxies. Upper limits are 2σ.

3.5 The stellar mass density at $z \sim 8$

The detection of $z \sim 8$ galaxies with IRAC is enticing as it enables us to place stronger constraints on the stellar masses of the highest redshift galaxies than possible from the far-UV alone. Recent studies in the HUDF have found no detection (individual or stacked) for $z \sim 8$ galaxy candidates (Labbé et al. 2010b), leaving estimates of the stellar mass density at these redshifts highly uncertain.

Here we perform photometry on the 3 $z \sim 8$ $Y_{098}-$dropout galaxies in the WFC3/ERS sample of R. J. Bouwens et al. (in preparation). These candidates are brighter than found in the HUDF ($H \approx 27$ versus $H \approx 28$). Two galaxies are detected at [3.6][3] and we calculate an average $SNR = 3.7$ in [3.6] and $SNR = 1.6$ in [4.5] for the stack of all three (see Fig 3, top panels). The best fits are $z = 7.7^{+0.18}_{-0.15}$, high stellar age $age_w = 300^{+50}_{-210}$ Myr[4], mass-to-light ratios $M/L_V = 0.15$ and $M/L_{1500} = 0.1$, and $\log \mathrm{sSFR} = -8.7$. Overall these properties are comparable to $H \approx 27$ $z \sim 7$ $z_{850}-$dropouts, suggesting modest evolution in the M/L between $z = 8$ and $z = 7$.

Following the approach of González et al. (2010) and Labbé et al. (2010b), we derive integrated stellar mass densities at $z \sim 8$ by multiplying the UV-luminosity densities integrated to $M_{\mathrm{UV,AB}} = -18$ (Bouwens et al. 2010b) by the mean M/L derived for the $z \sim 7.7$ galaxies, yielding $\rho^*(z = 8) = 1.8^{+0.7}_{-1.0} \times 10^6$ $M_\odot$ Mpc^{-3}. We also recompute the $z \sim 8$ stellar mass density of Labbé et al. (2010b) using the same M/L. Figure 4 shows the evolution of the stellar mass density from $z = 3$ to $z = 8$. The evolution over $3 < z < 8$ is well approximated by $\log \rho^*(z) = 10.6(\pm 0.6) - 4.4(\pm 0.7) \log(1 + z)$ [$M_\odot$ Mpc^{-3}] over $3 < z < 8$.

[3]We caution that source ERSy-2376440061 at [3.6] is close to pixels that are affected by "Muxbleed", which we subtracted using a 3rd order polynomial fit to the $20'' \times 20''$ background before performing photometry.

[4]Following Labbé et al. (2006) we report SFH-weighted age$_w$, where age$_w = t/2$ for CSF and t is the time elapsed since the start of star formation.

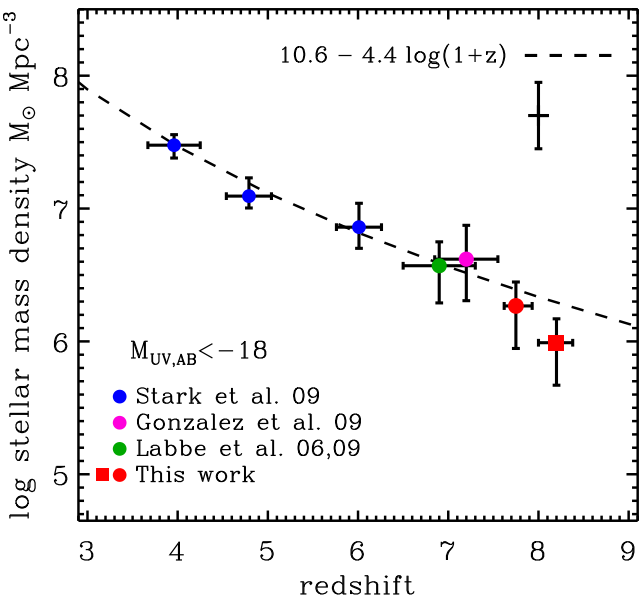

Figure 3.4: The evolution of the integrated stellar mass density. The red circle shows the $z \approx 7.7$ mass density, derived from the integrated UV-luminosity density of (Bouwens et al., in preparation) and the mean M/L derived here. All data are converted to a common limit $M_{\rm UV,AB} < -18$, using the UV LFs of Bouwens et al. (2010b). The WFC3/ERS data are corrected by +0.42 dex. The $z = 3-7$ luminous samples ($M_{\rm UV,AB} < -20$) from the literature (Stark et al. 2009 *blue circles*, González et al. (2010), *magenta circle*) are corrected by +0.38, +0.46, +0.57, and +0.75 dex at z=4, 5, 6, and 7, respectively. The HUDF requires no correction (Labbé et al. 2010b, *green circle*). The red square shows the $z \approx 8.2$ sample of (Bouwens et al. 2010b), but using the M/L derived here for the $z \approx 7.7$ sources. The dashed line shows a $\propto (1+z)^{-4.4}$ evolution. The floating error bar indicates the expected cosmic variance for the $z \sim 8$ sample.

3.6 Summary

Using a large sample of 36 $z_{850}-$dropout galaxies based on deep/wide-area WFC3/IR data from the Early Release Science, ultradeep data from the HUDF09, and wide-area NICMOS programs, we investigate the stellar population properties at extreme redshifts $z \gtrsim 7$. The main results are:

- The average rest-frame far-UV slope at $z \sim 7$ becomes bluer with decreasing luminosity, from $\beta \sim -2.0$ ($L^*_{z=3}$) to $\beta \sim -3.0$ (0.1 $L^*_{z=3}$), as reported by Bouwens et al. (2010c). The rest-frame $U-V$ becomes bluer as well, but is still moderately red $U-V \approx 0.3$ at

0.1 $L^*_{z=3}$, apparently excluding extremely young ages < 100Myr. If the ages inferred from the simple model fits are correct, galaxies started forming stars very early-on, perhaps as high as $z > 10$. The blue far-UV slope and red $U - V$ colors remain a challenge to fit, however, even for sub-solar metallicity models. Episodic SFHs with periods of activity and quiescence and/or a (~ 0.2 mag) contribution of emission lines to the [3.6]−band may be required to resolve the mismatch.

- The derived stellar masses correlate with the SFRs at $z \sim 7$ according to $\log M^* = 8.70(\pm0.09) + 1.06(\pm0.10) \log \mathrm{SFR}$, with relatively low scatter ~ 0.25 dex. Emission line contributions of ≈ 0.2 mag to both [3.6] and [4.5] would shift the relation by ≈ -0.2 dex in mass. The absence of galaxies with SFRs much lower or higher than the past averaged SFR (i.e., strongly bursting or suppressed) suggests that that the typical star formation timescales are probably a substantial fraction of the Hubble time. Note that instantaneously quenched galaxies may fade too quickly to be selected as dropout galaxies.

- The first Spitzer/IRAC detection of $z = 8$ galaxies and their red average $H_{160}-[3.6] \approx 0.55$ suggest that luminous early galaxies may have substantial $M/L_V \approx 0.15$, similar to $z = 7$ galaxies. The derived stellar mass density then increases gradually with time following $\log \rho^*(z) = 10.6(\pm0.6) - 4.4(\pm0.7) \log(1 + z)$ [$M_\odot$ Mpc^{-3}] over $3 < z < 8$.

Deeper IRAC data on $z > 7$ galaxies are needed to bolster these results. More nebular emission line measurements of $z > 2$ galaxies would help to understand the possible contribution to the broadband fluxes. Additional modeling of the distribution of SFR versus M^* is needed to decipher the SFHs of $z \sim 7$ galaxies. Larger samples would enable a more secure assessment of the mass density evolution beyond $z = 8$.

Chapter 4

Evolution of Galaxy Stellar Mass Functions, Mass Densities, and Mass to Light Ratios from $z \sim 7$ to $z \sim 4$

4.1 Introduction

Measurements of the stellar mass ($\mathcal{M}_{\rm star}$) of high-redshift galaxies ($z \gtrsim 4$) provide important constraints on scenarios of galaxy formation and early evolution. Recent deep near-IR WFC3/IR observations over the ERS field (Windhorst et al. 2011) combined with pre-existing deep GOODS IRAC data provide access to the rest-frame UV and optical wavelengths of $4 < z < 7$ star forming galaxies and hence reasonably accurate estimates of their $\mathcal{M}_{\rm star}/L_{\rm UV}$ ratios and stellar masses. The substantial samples detected with WFC3/IR span a range in

$\mathcal{M}_{\rm star}$, allowing, in principle, the derivation of mass functions (MFs).

MFs are a fundamental characteristic of the galaxy population but in practice, they are difficult to compute directly, especially at high-redshift because of selection effects, incompleteness, and contamination by interlopers. A simple alternative approach to derive the MF is to start with the well-determined UV Luminosity Functions (UV-LFs) at these redshifts and convert them to MFs using an *average* $\mathcal{M}/L_{\rm UV}$ (e.g., McLure et al. 2009). The main advantage is that LFs are corrected for all selection effects in the data and reach very faint limits. It requires, however, the *average* $\mathcal{M}/L_{\rm UV}$ to be independent of luminosity. The existence at high-z of a relatively tight relation between UV luminosity and $\mathcal{M}_{\rm star}$ (Stark et al. 2009) allows us to improve over this approach. We robustly re-derive this relation over a wide range of UV luminosities and combine it with published UV LFs to estimate improved MFs at $4 < z < 7$. Considering the scatter in the $\mathcal{M}_{\rm star}/L_{\rm UV}$ also allows us to correct for incompleteness at low $\mathcal{M}_{\rm star}$.

We adopt a $(H_0,\, \Omega_M,\, \Omega_\Lambda) = (70\,{\rm km\,s^{-1}\,Mpc^{-1}},\, 0.3,\, 0.7)$ cosmology. All magnitudes are in the AB system (Oke & Gunn 1983)[1].

4.2 Galaxy Sample from *HST* and *Spitzer* Data

The sources used here for determinations of the $\mathcal{M}/L$ ratios and $z = 4-6$ MFs were found in the recent Hubble-WFC3/IR observations of the ERS field. Both the GOODS ACS optical ($B_{435}V_{606}i_{775}z_{850}$) and the WFC3/IR ($Y_{098}J_{110}H_{160}$) data reach depths of $\sim$28 mag (5σ, $0\farcs35$-diameter apertures, see Bouwens et al. 2011c, Giavalisco et al. 2004). All sources have *Spitzer*/IRAC coverage with depths of 27.8 and 27.1 in the [3.6] and [4.5] channels, respectively (1σ in $2\farcs5$ apertures). The $z \sim 7$ sample is taken from (Labbé et al. 2010a).

The $z \sim 4,\ 5,\ 6$ sample totals 679 objects, consisting of $524\,B, 123\,V,$ and $32\,i$-dropouts

[1] All magnitudes/fluxes are in the observed frame except $M_{\rm UV,1500}$ and $L_{\rm UV,1500}$.

that were selected as in Bouwens et al. (2007).

$z \sim 4$ B-dropouts:

$$(B_{435} - V_{606} > 1.1) \ \wedge \ [B_{435} - V_{606} > (V_{606} - z_{850}) + 1.1]$$

$$\wedge \ (V_{606} - z_{850} < 1.6).$$

$z \sim 5$ V-dropouts:

$$\{[V_{606} - i_{775} > 0.9(i_{775} - z_{850}) + 1.5] \ \vee \ (V_{606} - i_{775} > 2)\}$$

$$\wedge \ (V_{606} - i_{775} > 1.2) \ \wedge \ (i_{775} - z_{850} < 1.3).$$

$z \sim 6$ i-dropouts[2]:

$$(i_{775} - z_{850} > 1.3) \ \wedge \ (z_{850} - J_{125} < 0.8).$$

The rest-frame optical photometry from *Spitzer*/IRAC is well suited for deriving stellar masses at these redshifts (e.g., Papovich et al. 2001, Yan et al. 2005, Eyles et al. 2005, Labbé et al. 2010a). A challenge is that the broad IRAC PSF usually results in these faint sources being contaminated by foreground neighbors. To obtain reliable IRAC fluxes we use the deblending method of Labbé et al. (2006, see also González et al. 2010, Labbé et al. 2010b;a, Wuyts et al. 2007, de Santis et al. 2007). Briefly, this method uses the higher-resolution *Hubble Space Telescope* (*HST*) images to create models of both the foreground neighbors and the source itself. We convolve each model image with a kernel to simulate the IRAC observations. We fit for all the sources simultaneously (with independent normalization factors) and subtract the best fits for the neighbors. In the clean image of each dropout we are able to perform standard aperture photometry. We use $2\farcs5$-diameter apertures and correct the fluxes to total assuming stellar profiles ($1.8\times$ in both channels).

As expected, this cleaning procedure does not work for every source. We restrict our sample to the 60% of sources with the best χ^2 residuals. This reduces the number of non-optimal

[2]Slightly modified from Bouwens et al. (2007).

subtractions to $< 8\%$. The final sample suitable for deriving masses from the *HST+Spitzer* data totals 401 sources: 299 $z \sim 4$, 78 $z \sim 5$, and 24 at $z \sim 6$. We do not expect this selection step to introduce any important biases since it depends on the distribution of the non-associated neighbors of the source. Of the remaining sources, $\sim 50\%$ have low IRAC signal-to-noise ratio ($< 2\sigma$ in [3.6]).

4.3 Stellar Mass Estimates from SED Fits

We use the FAST SED-fitting code (Kriek et al. 2009) to derive $\mathcal{M}_{\rm star}$ for the 401 $z \sim 4-6$ sources. We fit their SEDs with the full suite of fitted parameters. For all sources we fit the broadband ACS+WFC3/IR+IRAC [3.6] and [4.5] fluxes using the Bruzual & Charlot (2003; BC03) models with a Salpeter (1955) initial mass function (IMF, $0.1 - 100\,M_{\odot}$) and assuming a $0.2\,Z_{\odot}$ metallicity. We also include the sample of $z \sim 7$ galaxies with similarly-determined masses from Labbé et al. (2010a).

The star formation history (SFH) cannot be uniquely determined from broadband SEDs due to well-known degeneracies between the star formation timescale, age, and dust extinction. We have assumed a SFH with a constant star formation rate (SFR). Different SFHs introduce systematic offsets to the mass determinations, largely independent of redshift (cf. Papovich et al. 2011). The systematic differences between masses based on declining, constant, or rising SFHs are typically $\lesssim 0.3\,$dex (Finlator et al. 2007).

Figure 4.1 (left) shows the FAST SED-fit $\mathcal{M}_{\rm star}$ (from *HST+Spitzer* data) versus UV-luminosity (bottom axis). While the scatter is large (RMS $\sim 0.5\,$dex), there is a clear trend of increasing mass with increasing UV-luminosity. The $\mathcal{M}_{\rm star} - L_{\rm UV,1500}$ relation at $z \sim 4$ is well-fit by $\log_{10}(\mathcal{M}) \propto 1.7(\pm 0.2)\log_{10}(L_{1500})$. The lower bound that appears at $\mathcal{M}_{\rm star} < 10^8\,M_{\odot}$ corresponds to the $\mathcal{M}/L$ of the youngest model we allow (10 Myrs). The existence of this limit is not critical since our inferred $\mathcal{M}/L$ trend slope (and its uncertainty) is insensitive to the

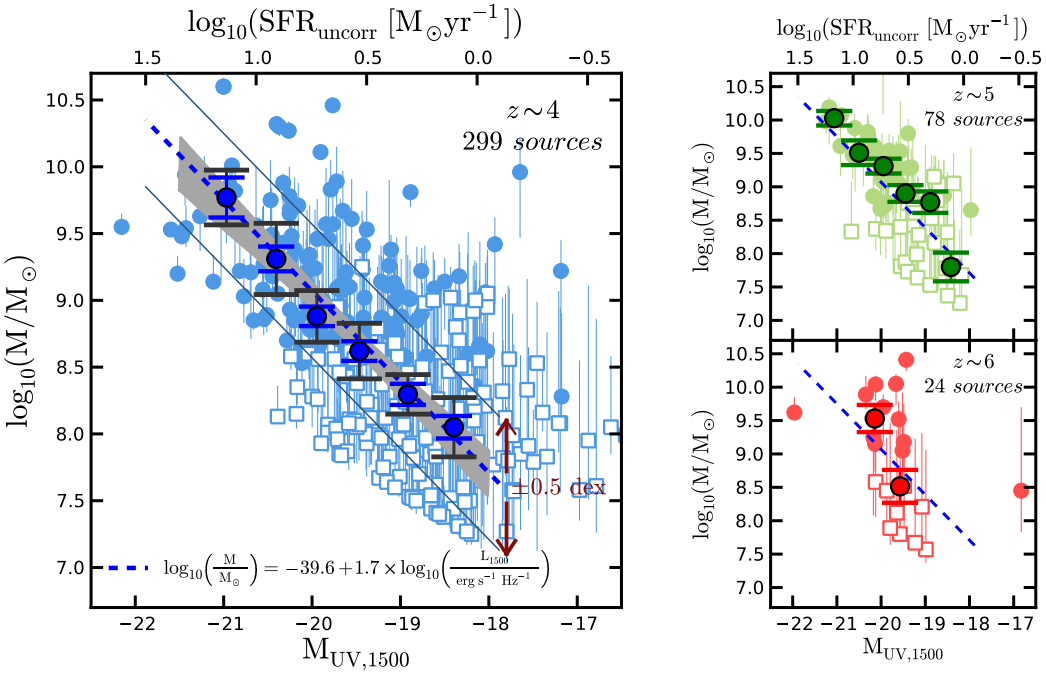

Figure 4.1: Stellar masses as a function of UV-Luminosity ($M_{\rm UV,1500} = 51.63 - 2.5 \times \log_{10}(L_{\rm UV,1500}[\rm erg\ s^{-1}\ Hz^{-1}])$) for the $z \sim 4$,5, and 6 samples. $\rm SFR_{uncorr}$ (top axis) is derived using the Madau et al. (1998) conversion formula (no extinction correction). The final sample of 401 sources with FAST SED-fit mass estimates is shown here. Open squares indicate low-S/N measurements ($< 2\sigma$ in [3.6]). The larger symbols in each panel represent the median mass of the sample ($\sim 0.5\,M_{\rm UV,1500}$ mag bins). The small error-bars represent the bootstrapped errors. The larger black error-bars include a conservative estimate of the systematics computed by comparing the estimated median mass at a given luminosity with the mass estimated from the stacked SEDs at the same luminosity. The dashed blue line (and shaded area, slope $= 1.7 \pm 0.2$) represents the median $\log_{10}\mathcal{M} - M_{\rm UV,1500}$ trend at $z \sim 4$. It is consistent with no evolution with redshift. The scatter at the luminous end (± 0.5 dex), where photometric errors are small, is intrinsic (see Figure 4.2).

cutoff. This is confirmed by a stacking analysis which shows significant IRAC detections in the faintest bins ($> 3\sigma$), and good agreement in the slopes (and uncertainties) derived. We remark that the broadband fluxes appear to be dominated by continuum light and not emission lines, as indicated by the similar median-stacked [3.6] and [4.5] IRAC fluxes. The $z \sim 4$ relation is consistent with the $z \sim 5$ sample, and, in zero-point, with the small $z \sim 6$ sample and the $z \sim 7$ sample presented in Labbé et al. (2010a).

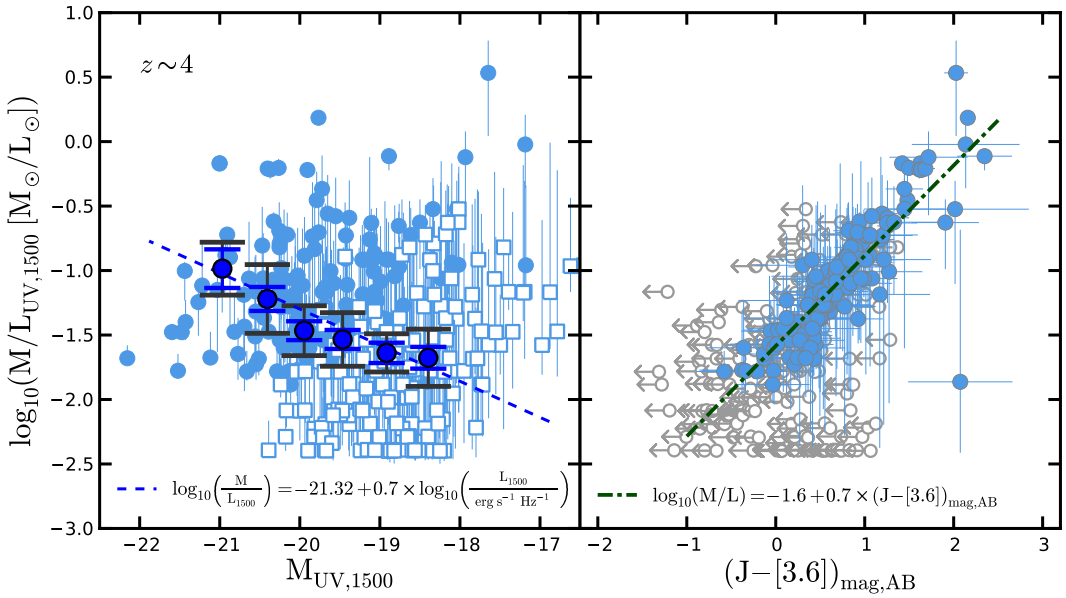

Figure 4.2: (*left*) $\mathcal{M}/L$ ratio as a function of UV-luminosity for the $z \sim 4$ sample. Symbols and error-bars as in Figure 4.1. The median $\mathcal{M}/L$ ratio changes by a factor $5\times$ in the luminosity range of our sample. (*right*) The correlation between the $\mathcal{M}/L$ and $J-[3.6]$ color. Arrows indicate 2σ upper limits. This tight relation suggests that the large scatter observed in the $\mathcal{M}/L$ (left panel) is largely due to intrinsic variations in the UV-to-optical colors. Photometric scatter can only account for $\lesssim 0.14$ dex at $M_{\mathrm{UV},1500} \sim -20$ (0.37 dex at -19).

Figure 4.2 explores the $z \sim 4$ $\mathcal{M}/L$ ratio trend in more detail, showing that $\mathcal{M}/L_{\mathrm{UV},1500}$ depends on luminosity; the $\mathcal{M}/L$ ratio is $\sim 5\times$ lower at $M_{\mathrm{UV},1500} = -18$ than at $M_{\mathrm{UV},1500} = -21$. This suggests that UV-faint galaxies contribute less to the global stellar mass density (SMD) than assumed in previous studies (Labbé et al. 2010b;a). Their contribution may still be significant at $z \gtrsim 7$ given the steeper faint-end slopes of the UV-LF (Bouwens et al. 2011c).

A striking aspect of the relation is the large scatter in $\mathcal{M}/L$. The observed sample variance (one standard deviation) for our sample is ~ 0.5 dex for $-21 < M_{\mathrm{UV},1500} < -18$. At the bright end $M_{\mathrm{UV},1500} < -20$ the scatter is largely intrinsic, whereas at the faint end $M_{\mathrm{UV},1500} > -19.5$ it is dominated by observational uncertainties. In particular, the $\mathcal{M}_{\mathrm{star}}$ of sources with IRAC detections are much better constrained than IRAC-undetected sources. We find that $\mathcal{M}/L$ ratio is tightly correlated with the $J-[3.6]$ color (standard deviation 0.18 dex,

Figure 4.2, right), suggesting that the variation is real and not an artifact of the modeling. Photometric uncertainties contribute ~ 0.14 dex to the scatter at $M_{\rm UV,1500} \sim -20$ (0.37 dex at -19).

The relation in Figure 4.2 (right) also allows us to estimate the possible effect of contamination by emission lines (not included in our models). At $z \sim 4$, a 20% contribution of Hα to [3.6] would result in redder $J - [3.6]$ colors and hence overestimates of the $\mathcal{M}/L$ and of the masses by 30%. This would affect the SMDs at all redshifts because they all rely on our $z \sim 4$ $\mathcal{M}/L$ ratio estimates (see Section 4).

4.4 Stellar Mass Functions at $z \sim 4,\ 5,\ 6,$ and 7.

Since UV-LFs have been derived from large samples to very faint limits and carefully corrected for a wide range of potential biases, they constitute an excellent basis for determining MFs. However, a meaningful transformation from UV-luminosity into stellar mass is not expected in general. Nevertheless, the calibration of $\log(\mathcal{M}_{\rm star})$ versus $M_{\rm UV,1500}$ in Figures 4.1 and 4.2 demonstrates that, for star-forming galaxies at $z \sim 4-7$, such meaningful transformation does exist.

However, the scatter about the mean $\mathcal{M} - M_{\rm UV,1500}$ relation is so large that ignoring it would produce significant errors. Galaxies with relatively low luminosity but high $\mathcal{M}/L$ ratios, for example, contribute significantly at the high mass end of the MFs[3]. Hence, we take care to determine the average $\mathcal{M} - M_{\rm UV,1500}$ relation in a robust way, we characterize its scatter at high masses and use this estimate of the scatter at lower masses/luminosities where the observational uncertainties dominate.

We use two approaches to create the MFs. First, we use the individual best-fit values in Figure 4.1 (small circles and squares) as representative of the $\mathcal{M} - M_{\rm UV,1500}$ distribution by

[3]Massive UV-faint, passively evolving red galaxies may be missing from our sample. Given the young age of the universe, their numbers are expected to be low.

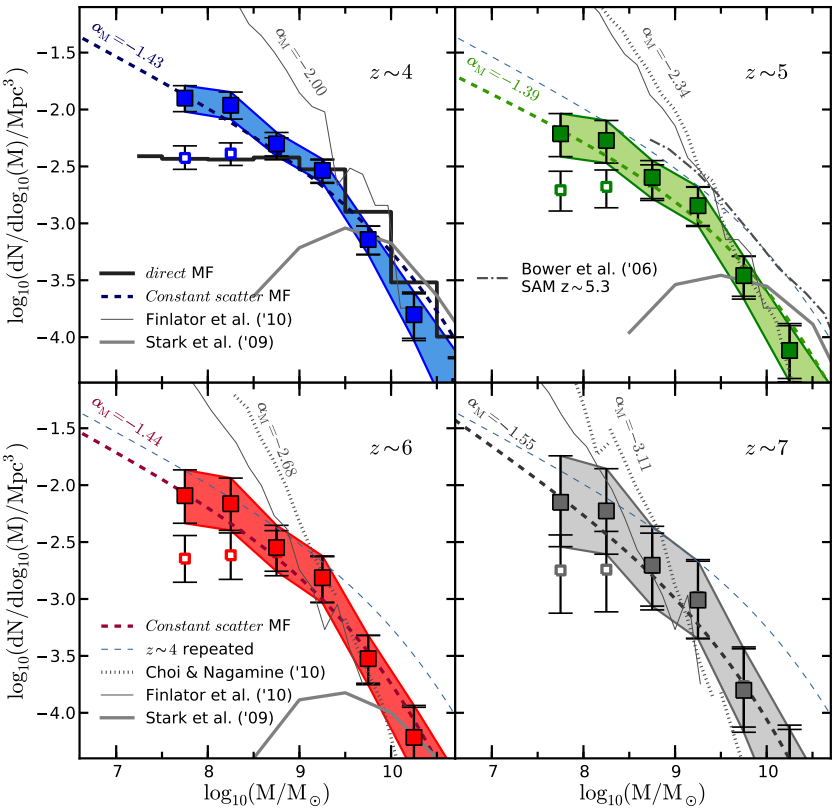

Figure 4.3: Stellar mass functions at $z \sim 4,\ 5,\ 6$, and 7 derived from the $\log(\mathcal{M}) - M_{\mathrm{UV},1500}$ distribution for the $z \sim 4$ B-dropouts (Figure 4.1), and the Bouwens et al. (2007; 2011c) UV-LFs at $z \sim 4 - 7$. The points are derived from the "bootstrap" approach (see text). Errors reflect uncertainties in the LF and the ~ 0.5 dex 1σ scatter of the $\mathcal{M} - M_{\mathrm{UV},1500}$ relation (Figure 4.1). Completeness-corrected values are estimated assuming that the $\mathcal{M} - M_{\mathrm{UV},1500}$ relation extends to fainter limits with similar scatter about the extrapolated mean trend ($M_{\mathrm{UV},1500} < -18$ uncorrected: open; corrected: filled; dark band is at 1σ around the corrected values). The *direct* MF at $z \sim 4$ (thick histogram) is in good agreement with the uncorrected MF (see text). For masses $> 10^{9.5}\,M_\odot$, the uncorrected $z < 7$ MFs are in rough agreement with the determinations of Stark et al. (2009) and of McLure et al. (2009) at $z \sim 6$ and $\mathcal{M} > 10^{10}\,M_\odot$. The thick dashed curve in each panel represents the *constant scatter* MFs derived from an idealized $\mathcal{M} - M_{\mathrm{UV},1500}$ relation (see text Section 3.4). These MFs have low-mass slopes $\alpha_M \sim -1.4 - -1.6$, slightly flatter than the UV-LFs ($\alpha = -1.7 - -2.0$: Bouwens et al. 2011c). In turn, the assumed symmetric scatter of 0.5 dex flattens their slopes at the high-mass end. The $z \sim 4$ *constant scatter* MF is repeated in the other panels for comparison (thin dashed curve). The dotted and thin solid lines show the simulated MFs from Choi & Nagamine (2010) and Finlator et al. (in preparation). Our new results are corrected for incompleteness, yet the difference between our results and the simulations is already substantial by $\mathcal{M} = 10^9\,M_\odot$. The source of the disagreement is unclear. Tentatively flatter MFs are seen in some SAMs (e.g Bower et al. 2006 at $z \sim 5.3$).

bootstrap re-sampling them. We sample the best-fit values only because the scatter dominates the uncertainties. To correct for incompleteness we add faint sources to the distribution. This important step increases the low-mass slope of the MFs substantially. Second, we use the best-fit $\mathcal{M} - M_{\rm UV,1500}$ relation (Figure 4.1, blue dashed line) and an *idealized* model of its scatter to produce what we label as "constant scatter" versions of the MFs. We compare against other estimates as a cross-check.

Bootstrapped MFs: We start with the $z \sim 4-7$, UV-LFs of Bouwens et al. (2007; 2011c) and draw 40000 luminosities from each LF in the range $-21.5 < M_{\rm UV,1500} < -18$. We convert the UV-luminosities into $\mathcal{M}_{\rm star}$ by assigning $\mathcal{M}_{\rm star}/L_{\rm UV}$ ratios from the distribution of points at $z \sim 4$ (Figure 4.2) with similar UV-luminosity. We use the $z \sim 4$ $\log(\mathcal{M}/{\rm L}) - {\rm M}_{\rm UV,1500}$ distribution at all redshifts because it is well-defined over a wide range of luminosities and is consistent with the relations at other redshifts (including the $z \sim 7$ relation in Labbé et al. 2010a). To account for the uncertainties in the LFs we perturb their Schechter parametrizations within the uncertainties and repeat 5000 times. This "bootstrap" process results in the uncorrected MFs (Figure 4.3 open squares and error bars).

As a crosscheck we also derived a histogram MF at $z \sim 4$ directly from the masses of the $z \sim 4$ sample using the search volume for the B-dropouts. This straightforward process gives a MF that is identified in Figure 4.3 as the "direct MF" for comparison with the uncorrected "bootstrap MF".

To correct the MFs for incompleteness at $\mathcal{M}_{\rm star} < 10^{8.5}\,M_{\odot}$, we assume that the observed $\log(\mathcal{M}) - M_{\rm UV,1500}$ relation extends to UV-luminosities below that observed and that the low-luminosity scatter is similar to the scatter around $M_{\rm UV,1500} \sim -18.5$. We use this assumption to populate the $-18 < M_{\rm UV,1500} < -15$ range of the $\log(\mathcal{M}) - M_{\rm UV,1500}$ relation. We re-derive the MFs with these *fake* sources added. The resulting errors on the corrected points include an added uncertainty that is typically about 30–40%. This accounts for the LFs uncertainties (specially the faint-end slope) and the large scatter about the relations. Other

sources of uncertainty may remain but further assessment is needed to fully evaluate them. Regardless, the current corrections must make these corrected MFs a better estimate of the true MFs. Applying the completeness corrections is a crucial step and significantly changes the slope of the MF at lower mass. The corrected MFs are shown in Figure 4.3 by the solid points and the solid color band, and are referred to as the *bootstrap* MFs.

Constant Scatter MFs: Now we combine the same LFs as above with an idealized version of the $\mathcal{M} - M_{\rm UV,1500}$ relation based on the best-fit: $\mathcal{M} \propto L_{\rm UV,1500}^{1.7(\pm0.2)}$. Since the scatter is important to reproduce the shape of the MF at the massive end, we generate a slightly more realistic approximation by assuming an idealized log-normal distribution with a constant standard deviation of 0.5 dex around the best-fit relation. The resulting relation, normalized by the LF, is integrated over L to get the *constant scatter* MFs.

At low masses, the MF slope, α_M, is set by the faint-end slope of the UV-LF, α_L, and the slope, b, of the $\log(\mathcal{M}) - \log(L_{\rm UV,1500})$ relation:

$$\alpha_M = \frac{\alpha_L - b + 1}{b},$$

found by extrapolating the $\mathcal{M} - L_{\rm UV,1500}$ relation to lower luminosities. We find MFs with steep low-mass slopes of $-1.43(\pm0.11)$, $-1.39(\pm0.11)$, $-1.44(\pm0.15)$, and $-1.55(\pm0.21)$ at $z \sim 4,\ 5,\ 6,$ and 7. These MF slopes are slightly flatter than the UV-LF slopes ($\alpha = -1.7 - -2$: Bouwens et al. 2011c). They are in good agreement with our completeness-corrected *bootstrap* MFs, and so provide a useful "sanity check" on those results. The standard deviation of 0.5 dex in the $\log(\mathcal{M}) - M_{\rm UV,1500}$ relation results in a slightly enhanced number density at the high-mass end compared to a case with no scatter. Our corrected MFs are considerably steeper than other MF determinations at high redshift (Stark et al. 2009) that do not apply completeness corrections. Truncating the constant scatter $\mathcal{M} - M_{\rm UV,1500}$ relation at $M_{1500} < -18$ (to represent survey incompleteness) results in MFs that are in good agreement with the non-corrected *bootstrap* MFs at low masses.

Table 4.1: Summary of Results

Quantity	$< z >= 3.8$	$< z >= 5.0$	$< z >= 5.9$	$< z >= 6.8$	$< z >= 8.0$
Completeness-corrected Mass Functions					
$\log_{10}(\mathcal{M}/M_\odot)$	$\log_{10}(d\,N/d\log_{10}(\mathcal{M}/M_\odot)/\mathrm{Mpc}^3)$				
[7.5 - 8.0]	$-1.90(^{+.11}_{-.12})$	$-2.21(^{+.18}_{-.20})$	$-2.09(^{+.23}_{-.24})$	$-2.15(^{+.41}_{-.39})$	...
[8.0 - 8.5]	$-1.96(^{+.12}_{-.12})$	$-2.27(^{+.18}_{-.20})$	$-2.16(^{+.23}_{-.23})$	$-2.23(^{+.37}_{-.38})$	...
[8.5 - 9.0]	$-2.30(^{+.10}_{-.11})$	$-2.60(^{+.15}_{-.19})$	$-2.55(^{+.20}_{-.21})$	$-2.70(^{+.34}_{-.36})$	...
[9.0 - 9.5]	$-2.53(^{+.10}_{-.11})$	$-2.84(^{+.17}_{-.17})$	$-2.81(^{+.19}_{-.22})$	$-3.01(^{+.34}_{-.34})$	...
[9.5 - 10.0]	$-3.14(^{+.12}_{-.13})$	$-3.46(^{+.17}_{-.21})$	$-3.52(^{+.21}_{-.23})$	$-3.80(^{+.36}_{-.37})$	...
[10.0 - 10.5]	$-3.80(^{+.20}_{-.23})$	$-4.12(^{+.22}_{-.27})$	$-4.22(^{+.28}_{-.31})$	$-4.53(^{+.39}_{-.61})$	...
[10.5 - 11.0]	$-4.43(^{+.26}_{-.46})$	$-4.81(^{+.33}_{-.45})$	$-4.97(^{+.38}_{-.70})$	...	...
SMD ($\mathcal{M} > 10^8\,M_\odot$) $[10^6\,M_\odot]$	$19.27(^{+2.88}_{-2.62})$	$9.64(^{+1.88}_{-1.78})$	$9.76(^{+2.30}_{-1.91})$	$6.98(^{+2.57}_{-2.26})$	...
SMD ($\mathrm{M}_{1500} < -18$) $[10^6\,M_\odot]$	$18.96(^{+1.94}_{-1.90})$	$9.52(^{+1.27}_{-1.58})$	$8.79(^{+2.11}_{-1.91})$	$4.08(^{+1.59}_{-1.19})$	$1.8(^{+0.7}_{-1.0})$
Best Fit	$\log_{10}(\mathrm{SMD}(z)/[M_\odot\,\mathrm{Mpc}^{-3}]) = 7.00(^{+0.04}_{-0.05}) - 3.35(^{+0.82}_{-0.94}) \times \log_{10}(\frac{1+z}{6})$				

Comparisons to simulated MFs: The MFs derived here are substantially steeper at low masses than what has been found in the past at these redshifts. This is not unexpected given that it has not been typical to correct for incompleteness. While the corrections are uncertain in magnitude the sign of the correction is not. Interestingly, even with the corrected and steeper slopes, the observed MFs are quite different from what is seen in recent hydrodynamical simulations (e.g. Choi & Nagamine 2010, Jaacks et al. 2011; Finlator et al. in preparation). The simulated MFs are steeper, with many more low-mass sources than we find. Tentatively, flatter MFs are seen in Semi Analytic Models (SAMs) (e.g Bower et al. 2006).

4.5 Stellar Mass Density at $z \sim 4,\ 5,\ 6,$ and 7

The MFs can be integrated to determine the SMD of the universe at high redshift. First, we integrate the (uncorrected) bootstrap MFs to determine the SMD at $z = 4,\ 5,\ 6,$ and 7 to faint-luminosity limits ($M_{1500} < -18$ – Table 4.1; Figure 4.4 left). Fitting the SEDs using the

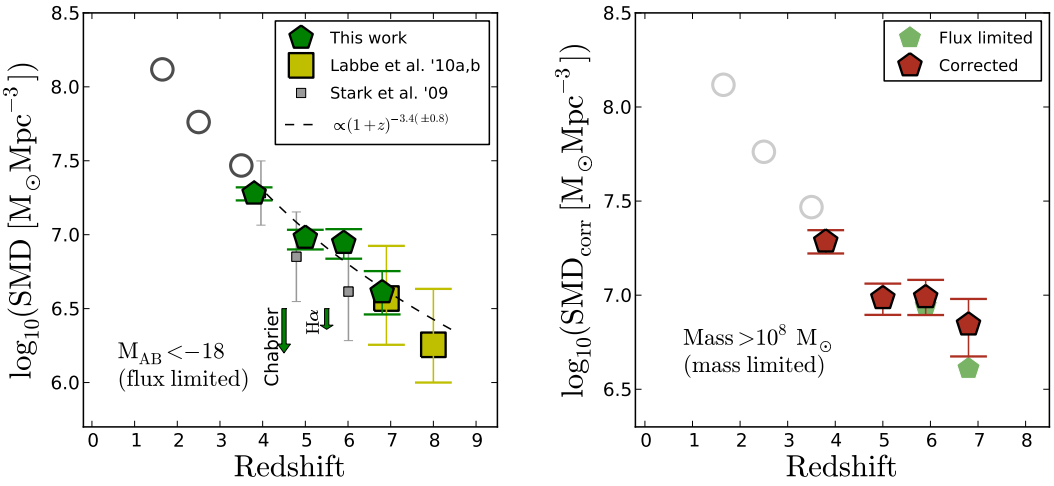

Figure 4.4: (*left*) Stellar Mass Density vs. redshift for sources brighter than $M_{\mathrm{UV,1500,AB}} = -18$. These SMD values are derived by integrating the uncorrected *bootstrap* MFs in Figure 4.3 to the faint luminosity limit $M_{\mathrm{UV,1500}} = -18$ at $z = 4,\ 5,\ 6,$ and 7. For comparison, we show the SMD determinations from Stark et al. (2009) corrected from their original $M_{\mathrm{UV,1500}} = -20$ limit to our $M_{\mathrm{UV,1500}} = -18$ limit (see text). The $z \sim 6$ estimate is also in good agreement with Yan et al. (2006) and Eyles et al. (2007). The low-redshift open circles were derived by integrating the Marchesini et al. (2009) MFs between $8.3 < \log_{10}(\mathcal{M}/\mathrm{M}_\odot) < 13$ and multiplying by 1.6 to match the Salpeter IMF. A constant SFH and $0.2\,Z_\odot$ metallicity was assumed to derive the masses at $z \gtrsim 4$. The effect of a possible 20% correction due to contamination by Hα is shown, as is the effect of using a different IMF. Our derived SMD growth with cosmic time is well fit by $\log_{10}(\mathrm{SMD}) \propto (1+z)^{-3.4\pm0.8}$. (*right*) As for the left panel but now to a fixed $\mathcal{M}_{\mathrm{star}}$ limit $> 10^8\,M_\odot$. The mass limited SMD is compared to the flux limited values from the left panel. The differences are relatively small (see text). Nonetheless, the importance of utilizing the completeness-corrected MFs will increase as improved, deeper data becomes available and we can push to lower masses and higher redshifts.

observed fluxes rather than upper limits allows us to reach lower limits than those of Stark et al. (2009) at $z = 4 - 6$. To compare to those results, we correct their original $M_{1500} = -20$ limit to our $M_{1500} = -18$ limit by adding 0.18, 0.22, and 0.32 dex at $z \sim 4,\ 5,$ and 6 respectively. We derive a SMD growth across cosmic time that is well fit by the function $\log_{10}(\mathrm{SMD}) \propto (1+z)^{-3.4\pm0.8}$. The effect of a different IMF and of a potential contamination by 20% Hα at $z \sim 5 - 6$ is also shown in Figure 4.4.

A major result of this paper is the derivation of MFs corrected for incompleteness at low masses. To utilize the (more representative and accurate) corrected MFs in deriving the

SMD of the universe at high redshift we need to integrate to a fixed mass limit. We choose $\mathcal{M} > 10^8\,M_\odot$ to extend to the limit of our corrected data. The right panel of Figure 4.4 shows these results, and compares them with the estimates to a fixed luminosity limit (see also Table 4.1).

The differences are relatively small due to the fact that the SMD is dominated by bright/massive sources already included in the flux limited ($M_{\rm AB} < -18$) samples. This depends somewhat on the exact slope of the $\mathcal{M} - L_{\rm UV}$ relation but is consistent with the results from the MFs of, e.g. Marchesini et al. (2009) at $3 < z < 4$. Nonetheless, the corrections become more important at higher redshift where the same $M_{\rm AB} < -18$ limit is applied to a galaxy population with fainter a L^* and steeper LFs. These corrections will become increasingly important as we push our MF estimates to lower masses and higher redshifts.

4.6 Key Results

We derive stellar masses from SED fits to *HST*+*Spitzer* data for over 400 $z \sim 4-7$ galaxies. We determine the $\mathcal{M} - L_{\rm UV}$ relation and find it to be steep ($\log(\mathcal{M}) \propto 1.7(\pm0.2)\log(L_{\rm UV})$) with large intrinsic scatter; the sample variance is ~ 0.5 dex at the bright end. We derive mass functions by combining the $\mathcal{M}$/L results with published deep UV-LFs at $z \sim 4-7$, and correct them for incompleteness. The corrected mass functions are steeper ($\alpha \sim -1.4$ to -1.6) than found previously, but still far less steep than those from recent hydrodynamical simulations. The integrated stellar mass density of the universe is derived at $z \sim 4,\ 5,\ 6$, and 7 to $\mathcal{M} \sim 10^8\,M_\odot$.

Chapter 5

The Rest Frame UV to Optical Colors and SEDs of $z \sim 4-7$ Galaxies.

5.1 Introduction

As a result of the installation of the WFC3/IR camera on the *Hubble Space Telescope* (*HST*), it is now possible to obtain extremely deep, high resolution observations in the near infrared. These observations match the exquisite optical data provided by the ACS camera over deep and ultra-deep fields like the GOODS and the HUDF (Giavalisco et al. 2004, Bouwens et al. 2007). The upgrade has enabled several teams to extend their searches for Lyman Break Galaxies (LBGs) to very high redshifts (e.g., Bouwens et al. 2010b, Oesch et al. 2010b; 2012, McLure et al. 2010, Yan et al. 2010, Bunker et al. 2010, Finkelstein et al. 2010). In combination, these two cameras have allowed for high S/N measurements of the rest-frame UV light of high redshift galaxies over a wide wavelength baseline.

As a result of these new observations, the UV LFs at $z \gtrsim 4$ are known to high accuracy. Another direct result from these observations is the determination of the UV slope of the SEDs, generally characterized by the parameter β ($f_\lambda \propto \lambda^\beta$, e.g., Meurer et al. 1999, Bouwens et al. 2009). This slope has been shown to become steeper (bluer colors) both with decreasing luminosity and with increasing redshift (Bouwens et al. 2009; 2011b, Wilkins et al. 2011, but see Dunlop et al. 2012, Finkelstein et al. 2011). For a mid-aged (100 Myr) stellar population, this slope generally depends most strongly on the dust reddening so this has been interpreted as an increase in the dust content of galaxies with cosmic time and as galaxies increase in luminosity (Bouwens et al. 2011b, Finkelstein et al. 2011).

Since the rest-frame UV light primarily probes young short-lived stellar populations (mostly O and B stars), it is interesting to extend these observations to longer wavelengths and study the relative importance of more evolved stellar populations. This is very challenging though and is now only possible thanks to the incredible sensitivity of the IRAC camera on the *Spitzer* Space Telescope. Some of the first observations of rest-frame optical light from $z \gtrsim 4$ galaxies showed quite red UV-to-optical colors (Eyles et al. 2005, Yan et al. 2005). Under the usual assumption of smooth, exponentially declining star formation histories (SFHs), these colors were interpreted as indicative of an evolved stellar population (ages $\gtrsim 100$ Myr) in combination with the younger populations probed by the UV-light. Follow-up work on $z \sim 4-7$ galaxies continued to reveal systems with moderate UV-to-optical breaks (e.g., Eyles et al. 2007, Yan et al. 2006, Labbé et al. 2006, Stark et al. 2009, González et al. 2010), even possibly to $z \sim 8$ (Labbé et al. 2010a). However interesting, these studies are only possible for the brightest $z > 4$ galaxies, due to the extreme depths required.

Some alternative explanations have been proposed for the red UV-to-optical colors observed in $z > 6$ galaxies. For example, for young star-froming galaxies, one might expect strong line emission. At the right redshift, these lines could contaminate the 3.6 and 4.5 μm IRAC fluxes, resulting in red UV-to-optical colors similar to those produced by the Balmer

break (Schaerer & de Barros 2009; 2010). For emission lines to be strong enough to dominate the rest-frame optical fluxes, extremely young ages ($\sim 6\,$Myr) are required. Such models have ages shorter than the dynamical times of these high$-z$ sources and are also somewhat uncertain. It would be surprising if the majority of these galaxies, which are selected over a redshift range that spans $\gtrsim 200\,$Myr, had such young ages. Even if rest-frame optical emission nebular emission lines do not dominate the measured IRAC fluxes, it is expected that they will contribute some of the flux measured in the mid-IR, but the exact contribution currently remains hard to establish at these high redshifts.

It has been routine, then, to compare the colors of these high redshift galaxies with synthetic stellar population (SSP) models of relatively evolved galaxies with smooth SFHs to derive physical properties from the observations. By studying LBG samples at different redshifts in the aforementioned way, one intriguing result has emerged. At a given intrinsic luminosity, the specific Star Formation Rate (SFR) of galaxies seems to remain remarkably constant with redshift (Stark et al. 2009, González et al. 2010; 2011, McLure et al. 2011; slightly modified to account for the latest dust corrections by Bouwens et al. 2011b). This result has called the attention of theorists and has proved very hard to reproduce in simulations (e.g., Weinmann et al. 2011, Khochfar & Silk 2011). The assumptions used to derive these results vary somewhat from group to group. In this work, we present the basic observations that lead to such a result, namely the observed SEDs of galaxies at $z \sim 4 - 7$.

In the present work we study the observational properties of the typical high redshift galaxy. We do this by splitting our large sample in both redshift and UV-luminosity bins and constructing mean SEDs. The large number of galaxies allows us to study the typical colors at high S/N but also extend our measurements to faint limits that are currently inaccessible on an individual basis with the current data. Although the scatter about the typical properties is also highly interesting, we defer their study to a future work which relies on even deeper *Spitzer* observations. In Section 4.2 we present the data and in Section 4.3 the sample selection and

Table 5.1: Sample Summary

Field	$z \sim 4$	$z \sim 5$	$z \sim 6$	$z \sim 7$[a]
ERS	270 / 524	77 / 123	20 / 32	15 / 18
HUDF	137 / 205	41 / 55	38 / 51	21
TOTAL	407 / 729	118 / 178	58 / 83	36

Notes. Summary of the number of sources in the sample. IRAC photometry of these sources requires fitting and subtraction of the flux from surrounding foreground neighbors. This is not possible in all the cases. The table shows the number of sources with clean IRAC photometry / total number of sources found in the field.
[a] We adopt the sample presented in Labbé et al. 2010a.

photometry. Section 4.4 describes the stacking procedure and we discuss the stacked SEDs and colors in Section 4.5. A summary is presented in Section 4.6.

Throughout, we use a $(H_0, \Omega_M, \Omega_\Lambda) = (70\,\mathrm{km\ s^{-1}}, 0.3, 0.7)$ cosmology when necessary and we quote all magnitudes in the AB system (Oke & Gunn 1983).

5.2 Data

In this paper, we make use of the large number of $z \gtrsim 4$ galaxies found in the ultra-deep HUDF data and wide-area ERS data to construct median SEDs for star-forming galaxies at $z \sim 4-7$. The deep optical, near-IR, and deep IRAC coverage over these fields allow us to create SEDs that cover both the rest-frame UV and the rest-frame optical down to very faint fluxes.

5.2.1 *HST* ACS and WFC3/IR

In constructing our median SEDs, we make use of the deep optical and near-IR *HST* data from ACS (GOODS program, Giavalisco et al. (2004)) and WFC3/IR (e.g., Bouwens et al. 2011b). Over the ERS field (Windhorst et al. 2011), both the ACS optical ($B_{435}V_{606}i_{775}z_{850}$) and the WFC3/IR ($Y_{098}J_{125}H_{160}$) images from *HST* reach depths of ~ 28 mag ($5\,\sigma$ measured on $0\farcs35$-diameter apertures). In the HUDF field, the ACS optical data ($BViz$) are $1.5-2$ mags

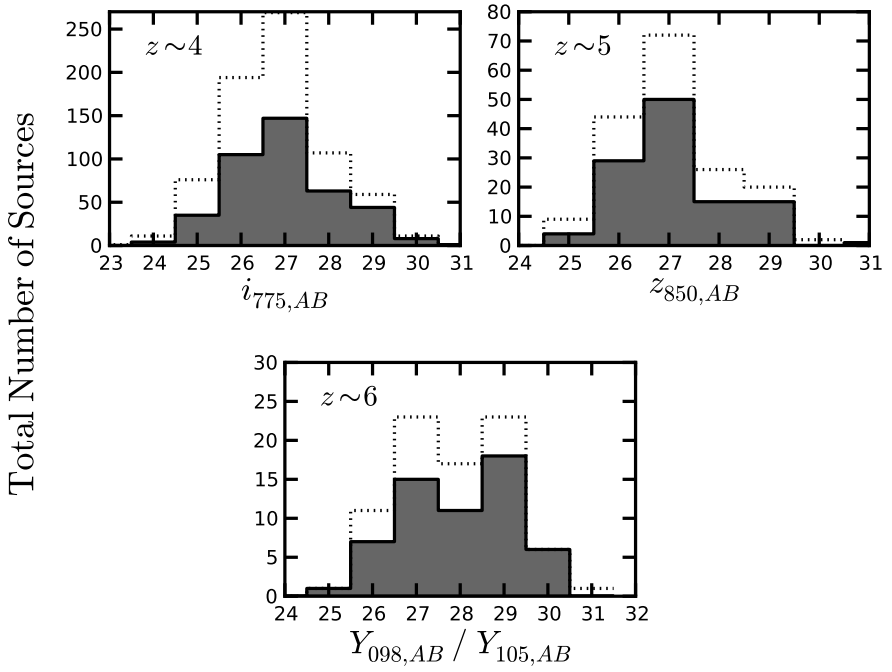

Figure 5.1: The observed magnitude distribution of the sample. The reference filters for each redshift sub-sample have been chosen to be close to rest-frame $\lambda = 1500$ Å. For the $z \sim 6$ sources in the ERS we used the Y_{098} filter whereas the Y_{105} filter was used for the sources in the HUDF. The open histograms include all the sources and the gray filled histograms include only the sources with clean IRAC photometry. This selection does not introduce biases relevant to the determination of the mean rest-frame optical colors of these sources.

deeper, and the WFC/IR data ($Y_{105}J_{125}H_{160}$) are 1.5 times deeper than the ERS. The HUDF was observed with the Y_{105} filter instead of the Y_{098} filter used in the ERS.

5.2.2 Spitzer/IRAC

Because these fields are located inside the GOODS-S field, they both have deep *Spitzer*/IRAC coverage that amounts to ~ 23.3 hr over the ERS and twice that for the HUDF which was observed to the same depths but in two different epochs with the IRAC camera rotated by 180° (Giavalisco et al. 2004). For IRAC channel 1 images ($\lambda_\circ = 3.6\ \mu m$), each single epoch reaches depths of 27.8 mags, measured over 2.″5-diameter apertures (1σ). For channel 2 ($\lambda_\circ = 4.5 \mu m$)

this limit corresponds to 27.2 mags.

5.3 Sample Selection and Basic Photometry

The criteria used to identify high redshift star forming galaxies have already been presented in numerous previous works. For details on the selection procedure and discussion of sample contamination please see Bouwens et al. (2007; 2011c). In short, the selection criteria used to find the sources presented here is as follows:

$z \sim 4$ B-dropouts:

$$(B_{435} - V_{606} > 1.1) \ \wedge \ [B_{435} - V_{606} > (V_{606} - z_{850}) + 1.1]$$

$$\wedge \ (V_{606} - z_{850} < 1.6).$$

$z \sim 5$ V-dropouts:

$$\{[V_{606} - i_{775} > 0.9(i_{775} - z_{850}) + 1.5] \ \vee \ (V_{606} - i_{775} > 2)\}$$

$$\wedge \ (V_{606} - i_{775} > 1.2) \ \wedge \ (i_{775} - z_{850} < 1.3).$$

$z \sim 6$ i-dropouts:

$$(i_{775} - z_{850} > 1.3) \ \wedge \ (z_{850} - J_{125} < 0.8).$$

The combined samples contain a total of 729 sources at $z \sim 4$, 178 at $z \sim 5$, and 83 at $z \sim 6$ (see Table 5.1).

We complement the $z \sim 4$, 5, and 6 samples with the sample of 36 $z \sim 7$ sources presented by Labbé et al. (2010a). We have adopted the $z \sim 7$ stacks presented in that work.

At these depths, the *Spitzer*/IRAC images are fairly crowded due to the size and shape of its PSF. As a consequence, standard aperture photometry of the sources generally results in fluxes that are contaminated by flux coming from unrelated sources that are nearby in the sky. We are able to de-blend the fluxes from the different sources by making use of

the higher resolution information available through the *HST* images. Our method has been explained in previous works by our group (e.g Labbé et al. 2006; 2010b, González et al. 2010; 2011) but we give a short description here. We start by registering the IRAC images to the higher resolution *HST* image that will be used as a light profile template. In this case we use the WFC3/IR H_{160}-band image as our template because it is the closest in wavelength and has high signal to noise. We use the SExtractor software (Bertin & Arnouts 1996) to create segmentation maps. We isolate all the sources in a small area around each galaxy in our sample using these segmentation maps. We then convolve them with a kernel derived from the PSFs of the *HST* and the IRAC images. We fit for the normalization fluxes of all sources (including the source we are trying to clean) simultaneously. Finally we remove the flux from the unrelated sources to obtain a clean image of the galaxies in our sample. Later we use these cleaned images to produce median stacks.

The procedure described above does not always produce acceptable results. The reasons why it can fail vary but the most common is the presence of a source that is too bright, extended, and close to our region of interest. In these cases the amount of flux subtracted off our source of interest is large and more uncertain and in most cases results in large residuals. We have carefully inspected the residual images (all sources subtracted, including the one in our sample) and the cleaned images (only unrelated neighbors subtracted) of each of the sources in the original sample and come up with a sub-sample of sources with clean IRAC photometry. This "by eye" inspection criterion generally results in good agreement with a criterion that selects only the images with the lowest χ^2 residuals but allows us to also remove sources that, even though have moderate χ^2 values, present mild to strong residuals located very close to the source. Overall, this reduces the sample to 60% of the original (see Table 5.1). Since the criterion adopted here depends on the complexity of the unrelated sources, it is not expected that it should introduce any biases that would be relevant in the determination of the mean rest-frame optical colors (see Figure 5.1).

5.4 Stacked Photometry and Median SEDs

It has been shown that in star forming galaxies the total SFR appears to correlate with stellar mass, the so called main sequence of star forming galaxies (Noeske et al. 2007). This sequence has been observed at high-redshifts ($z \gtrsim 4$) but, contrary to what has been observed at $z < 2$, the normalization of the relation at fixed stellar mass does not seem to evolve over $2 < z < 7$ (Stark et al. 2009, González et al. 2011). The lack of deeper rest-frame optical from *Spitzer*/IRAC for these sources is one of the big limitations to study this sequence to fainter magnitudes. In terms of the bulk of the population, however, progress can be made by stacking large numbers of sources to study their mean properties. In this section we seek to construct the median SEDs of galaxies at $z \gtrsim 4$.

Due to the nature of the dropout search and the filters available, our full sample is naturally divided in redshift bins centered at $\langle z \rangle = 3.8, 5.0, 5.9$ plus the $\langle z \rangle = 6.9$ sample from Labbé et al. (2010a). In this section, we further split each redshift sub-sample based on observed rest-frame UV-luminosity. The filters used as reference UV-luminosity are the i_{775} filter for the $z \sim 4$ sources; the z_{850} for the $z \sim 5$ sources; the Y_{098} for the $z \sim 6$ sources in the ERS and the Y_{105} for the $z \sim 6$ sources in the HUDF; and finally, the J_{125} filter the $z \sim 7$ sources. These filters were chosen to be close to rest-frame 1500 Å at the different redshifts and make the splitting criterion fairly uniform across redshifts. These bins are presented in Figure 5.1.

In the case of the *HST* ACS and WFC3 imaging, the fluxes utilized correspond to the MAG_AUTO values determined using the SExtractor code plus an additional correction to account for the flux outside the MAG_AUTO aperture. This corrections, which are estimated assuming stellar profiles, are generally in the range $0.1-0.3$ mags and are larger for fainter sources (because they generally have smaller apertures). In each UV-luminosity bin, the median flux corresponds to the median of the individual measurements. Only sources with reliable IRAC fluxes were included in the median. The uncertainty in the median was estimated through

bootstrap resampling simulations performed as follows. These simulations involved creating a large number of realizations of the sample, by drawing, with replacement, N_{bin} fluxes (from the total N_{bin} values available). The fluxes are perturbed within their individual uncertainties before estimating the median of the realization. The uncertainties on individual sources are generally quite small, given the very high signal to noise of the images. There are however, systematic uncertainties in the absolute calibration of the different bands and instruments across the SED. These uncertainties are typically no smaller than 5%, so we adopt this value as our minimum allowed uncertainty for any given flux.

In the case of the IRAC imaging, most sources are too faint to be individually detected even in these deep $\sim$ 23.3 hr integration images. Instead of using individual fluxes, we first median combine (pixel by pixel) the cleaned stamps of the sources within a bin that have clean residuals from our IRAC cleaning procedure. The pixel by pixel median also removes any bad residuals that we may have overlooked in our inspection. We perform standard aperture photometry on the stacked images using a circular aperture of $2\farcs5$-diameter and correct the fluxes to total assuming PSF profiles. This amounts to a factor 1.8 in both the [3.6] and the [4.5] IRAC filters. The local background is estimated from the stacks, in a ring between $6''$and $10''$diameters around the stamp center, where the source is expected to be, and then subtracted off the image.

It is important to note that this procedure is very different to the way the *HST* stacking is done. We have checked that this does not impose large biases in the measurement by implementing the same procedure described for the IRAC stacks, in the $H_{160}-$band stacks. We have first masked out the neighboring sources and then convolved the H_{160} image with a kernel to degrade it to the resolution of the IRAC images. We have median combined these images and performed simple aperture photometry in the same way that we did for the IRAC bands, using $2\farcs5$-diameter apertures and correcting to total assuming stellar profiles (factor 1.8). We find that the $H_{160}-$IRAC colors measured with the two methods are in excellent agreement,

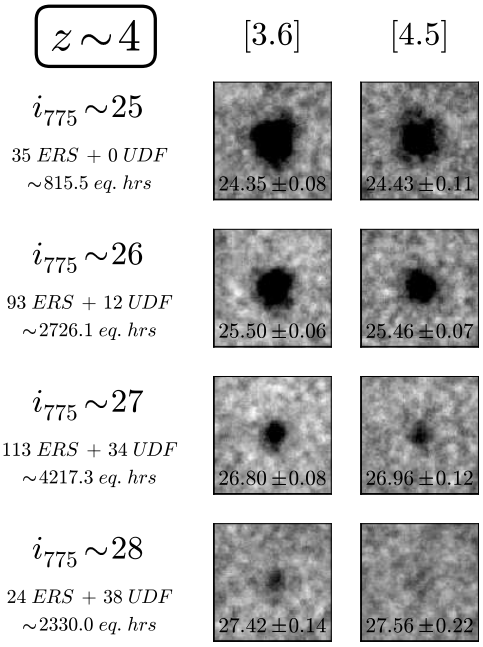

Figure 5.2: Median stacked images of the $z \sim 4$ sources. The sample has been split according to $i_{775,\mathrm{AB}}$ magnitude (approx. rest frame 1500 Å) in bins of 1 mag. The stamps are $10''$on a side. The number of sources stacked along with the total equivalent integration time has been included to the left of the stamps. The magnitudes included in the stamps were measured using circular apertures of $2\farcs5$ in diameter and corrected to total assuming stellar profiles which amounts to ~ -0.6 mags in both the [3.6] and the [4.5] channels. The background was estimated from the stacks and subtracted off the images. To estimate the uncertainties on the fluxes measured we created 200 random realizations of the stack. In each realization, sources were drawn with replacement and then median stacked pixel by pixel.

indicating that we are not introducing any significant bias in the estimates of the UV-to-optical colors.

To estimate the uncertainty in the IRAC stacks, we also create bootstrap realizations. We treat the two epochs of IRAC data over the HUDF as independent stamps in the stack, thereby effectively weighting with exposure time, i.e., $N_{bin} = N_{ERS} + 2N_{HUDF}$. In each bootstrap draw, then, we draw with replacement $N_{ERS} + 2N_{HUDF}$ such stamps, and estimate fluxes as described above. The image noise in each stack is dominated by the background noise (shot noise from the sources will contribute less than 2% even for the brightest sources in the sample). This image noise is expected to decrease with the total equivalent exposure time approximately

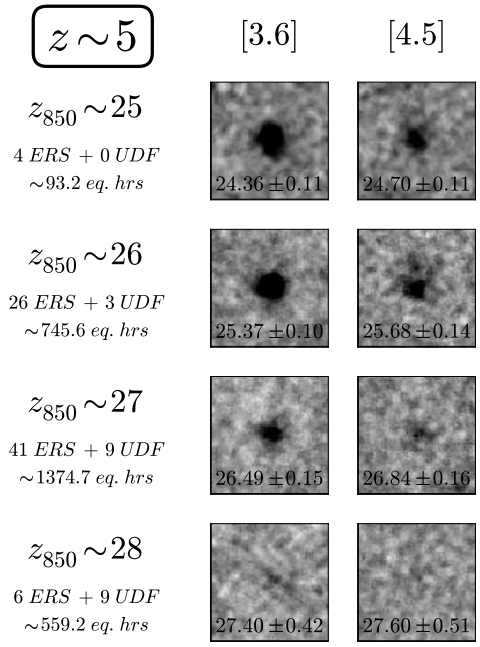

Figure 5.3: As in Figure 5.2 but for the $z \sim 5$ sample. In this case the sample was split according to z_{850} magnitude to approximate rest-frame 1500 Å. The faintest bin shows a weak detection in IRAC, making the colors derived less robust.

as $1/\sqrt{t_{\rm exp,eq}}$ ($t_{\rm exp,eq} = (N_{ERS} + 2N_{HUDF}) \times 23.3\,{\rm hr}$). The actual photometric uncertainties that we derive are always greater than this because they also include the intrinsic scatter in the fluxes of the sources that have been stacked together (see Appendix A). Stamps for all the IRAC median stacks along with the derived magnitudes and uncertainties are presented in Figures 5.2, 5.3, and 5.4. Table 5.2 is a compilation of all the stacked photometry including the Labbé et al. (2010a) stacks and information on the number of sources that go in each stack. It can be seen in the figures that even for sources as faint as 27 mag, the stacks show good detections in both IRAC bands.

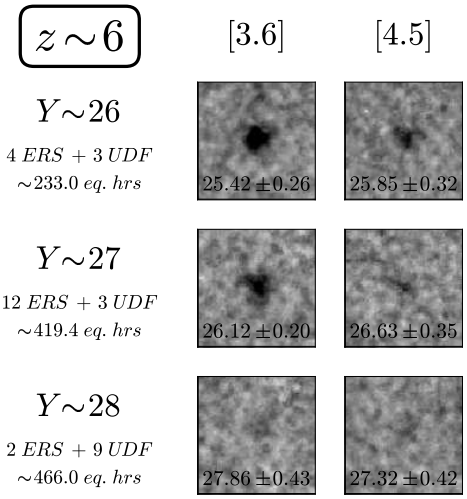

Figure 5.4: As in Figure 5.2 but for the $z \sim 6$ sample. In this case the sample was split according to Y_{098} magnitude in the case of the ERS sources and Y_{105} for the HUDF sources (approximately rest-frame 1500 Å). As in the faintest bin in Figure 5.2, the faintest bin at this redshift also shows a rather weak detection in IRAC.

5.5 Rest-Frame UV-to-optical Colors of high-z Star-Forming Galaxies.

The observed colors of galaxies can give us important information about the stellar populations that compose them. Usually, this is accomplished by comparing their colors with those of synthetic stellar population (SSP) models. In this work, we chiefly explore the observed UV-to-optical colors and what can be learned from them and from their dependence on luminosity and redshift. When models are invoked, we use the Bruzual & Charlot (2003; BC03) models and we assume a Salpeter (1955) IMF, constant SFH, and $0.2\,Z_{\odot}$ metallicity, as these quantities cannot be constrained from our data. To derive best fits we use the SED fitting code FAST (Kriek et al. 2009).

The rest-frame UV-to-optical color is of particular interest at high redshifts. Several studies have detected significant rest-frame UV-to-optical colors ($\gtrsim 0.5$ mag) in $z \gtrsim 4$ galaxies (Eyles et al. 2005; 2007, Yan et al. 2005, Stark et al. 2009, González et al. 2010; 2011, Labbé

et al. 2006; 2010a, McLure et al. 2011). The usual interpretation is that these colors derive from large Balmer breaks which are associated with evolved stellar populations with ages $\gtrsim 200$ Myr. This is surprising given how young the universe is at the time these galaxies are being observed. The main limitation for field studies is the depth of the *Spitzer*/IRAC imaging available, which constrains these studies to the brightest LBGs. Searches behind clusters provide an alternative to probe the fainter populations (see, e.g., Ellis et al. 2001, Bradley et al. 2008, Richard et al. 2008, Laporte et al. 2011, and the recent tentative determination of a 1.5 mag Balmer break in a $z \sim 6$ galaxy by Richard et al. 2011) but the number of sources amenable to such studies, remain low. We work around this limitation by stacking large numbers of sources, which allows us to estimate the typical rest-frame UV-to-optical colors of faint $z \gtrsim 4$ sources.

We start by presenting the results found at $z \sim 4$ where the similar and complementary work of Lee et al. (2011a) allows us to study this colors over an unprecedentedly large range of UV-luminosities.

5.5.1 The UV-to-Optical Colors at $z \sim 4$.

Our sample of $B-$dropouts has a mean redshift of $\langle z \rangle = 3.8 \pm 0.3$. We divide this sample based on their i_{775} luminosity (which approximately corresponds to rest-frame 1500 Å) in four bins of $\Delta i_{775} = 1$ mag. These are the same bins as shown in the histogram in Figure 5.1. The bins at $i_{775} > 28$ mag are too faint to be detected in *Spitzer*/IRAC and will not be included in the analysis. Assuming the mean redshift of the sample, these bins correspond approximately to $M_{1500} = -21, -20, -19$, and -18, which covers the moderately bright to faint end of the population ($M^*_{1600,z=4} = -20.24$, Bouwens et al. 2007).

In a recent study, Lee et al. (2011a) focus on the median SEDs of the brightest $z \sim 4$ galaxies found in the ground-based NOAO Deep Wide-Field Survey. Their sample has a mean redshift $\langle z \rangle = 3.7 \pm 0.4$, and their SEDs also sample the rest-frame UV and optical using a combination of optical filters: B_W, R, I (Mosaic Camera), near-IR filters: J, H, K_s

(NEWFIRM Camera), and the *Spitzer*/IRAC mid-IR channels 1 through 4[1]. Similar to the present work, they divide their sample according to the I–band luminosity, although with uneven bins. Their sources are intrinsically brighter than in this work, corresponding to $L > L^*_{z=4}$ sources roughly covering the range $-23 \lesssim M_{1500} \lesssim -21$.

The combination of the Lee et al. (2011a) sample with our data spans the UV-luminosity range: $-23 \lesssim M_{1500} \lesssim -17.5$. This represents an unprecedented dataset to study the SEDs, and especially the UV-to-optical colors, of $z \sim 4$ galaxies over a large range of luminosities. The SEDs from both works are presented in Figure 5.5. In this figure the H_{160} is shown with open symbols since it is likely biased and should be ignored, as explained in detail later. An overall trend to bluer colors (both in the rest-frame UV and the rest-frame UV-to-optical colors) towards fainter luminosities is already apparent in this figure.

We quantify the UV-to-optical colors by estimating the interpolated rest-frame $(U_n - V_n)$ colors for the median-stacked SEDs in both sets. Figure 5.6 shows a systematic trend of redder $(U_n - V_n)_{\rm rest}$ colors as a function of increasing UV-luminosity.

The interpolated $(U_n - V_n)$ colors were determined from the best fits to the full observed SED, where the fits correspond to a linear combination of a set of template SEDs. These SEDs correspond to the default template set from the photometric code EAZY (Brammer et al. 2008). This template set was constructed and calibrated empirically to determine accurate photometric redshifts of galaxies of various types from very blue starbursts to red ellipticals and has been shown to work well up to $z \sim 5 - 6$ (Brammer et al. 2008). For the U_n and V_n filters we have assumed narrow ideal filters that correspond to step functions of width 100 Åcentered at 3500 Å and 5500 Å for U_n and V_n respectively. The colors were calculated from the best fit combination of templates using the filters described above. To estimate the uncertainty in the $(U_n - V_n)_{\rm rest}$

[1]Although relatively deep IRAC channels 3 & 4 data (sampling 5.8 μm and 8.0 μm respectively) is available for our sample in the GOODS-S, this data is still $\gtrsim 0.5$ mag shallower than the channel 1 & 2. It is, therefore, much harder to obtain reliable stacked photometry in those bands, especially considering that our sample is much smaller and intrinsically fainter than the Lee et al. (2011a) sample. We have not included these bands in the median-stacked SEDs presented in this work.

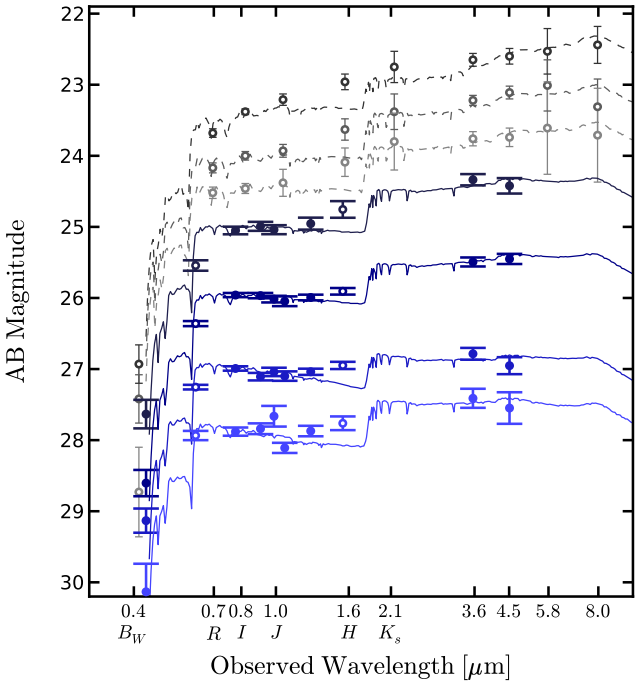

Figure 5.5: Stacked SEDs of $z \sim 4$ galaxies in 7 bins of UV-luminosity. The faintest SEDs (blue solid symbols and lines) correspond to the SEDs derived from our sample. This sample has a mean redshift of $\langle z \rangle = 3.8 \pm 0.3$ and was split in bins of observed $\Delta i_{775} = 1$ mag, approximately covering the UV-luminosity range $-21 \lesssim M_{1500} \lesssim -18$. The brightest stacks (gray open symbols and dashed lines) correspond to the median SEDs presented in Lee et al. (2011a), for a sample of galaxies with mean redshift $\langle z \rangle = 3.7 \pm 0.4$. These SEDs allow us to extend the luminosity range to brighter luminosities up to $M_{1500} \sim -23$. In Lee et al. (2011a) the sources were split in six bins according to observed I-band luminosity. For clarity, we only show every other bin but all are considered in Figure 5.6. The x-axis shows wavelength and the approximate position of the set of filters used in the Lee et al. (2011a) study ($B_W RIJHK_S$[3.6][4.5][5.8][8.0]: see their Figure 4). Best fit BC03 models are included for references (the H and K_s-band fluxes were excluded from the fits because they are likely biased – see text, Section 4.5.1). A trend of bluer UV-slopes and smaller Balmer breaks at fainter luminosities is observed.

estimates, we perturbed the photometry and the redshift of each median-stacked SED within the allowed uncertainty, and a new fit was obtained. A new set of colors was measured from this best fit and the procedure was repeated a large number of times to derive the confidence intervals. A similar procedure was used to derive rest-frame M_{1500} magnitudes for an ideal filter centered at 1500 Å and with a width of 100 Å.

For the data-point at $M_{1500} \sim -19$, only an upper limit can be obtained due to the limitations of the template set used here. The EAZY default template set only includes SEDs

with $(U_n - V_n)_{\rm rest} \gtrsim 0.3$. The SED at $M_{1500} \sim -19$ is likely to have a $(U_n - V_n)_{\rm rest}$ color of ~ 0.3 mag, so no reliable lower limit can be obtained. We choose to show a 2σ upper limit. Other more sophisticated algorithms to determine interpolated rest-frame colors for an observed SED yield very similar results (e.g., the InterRest code, Taylor et al. 2009, which implements the algorithm described in Rudnick et al. 2003). However, such algorithms also depend on the template set resulting in similar limitations.

It is important to note that, when deriving this color from best fits, we have ignored the $H_{160}-$band in our stacks and the H and K_s-bands in the Lee et al. (2011a) stacks. Given the redshift distribution of the sample it is expected that for some fraction of the sources (the ones at the lowest redshifts) the $H-$band fluxes measured will include some rest-frame optical light. As a result, the estimated median rest-frame UV flux, will be biased towards larger values. To attempt a correction for this would require us knowing the exact redshift distribution of the sample, but even then a correction would be highly uncertain, so we opt to remove these photometric points from all fits.

In recent works, Bouwens et al. (2009; 2011b) accurately determine the UV-slope of LBGs at $z > 3$ as a function of UV-luminosity and redshift. For a star-forming stellar population, the UV-slope, parametrized by β ($f_\lambda \propto \lambda^\beta$), is most sensitive to the dust content of the galaxy. In consequence, the authors argue that the dependence of β on UV-luminosity can be fully explained by an increase in the amount of dust that these galaxies contain as they become brighter. If this is the case, a trend of redder $(U_n - V_n)_{\rm rest}$ colors for UV-brighter sources like the one observed here is also expected, since this color is also affected by dust extinction. The bottom panel of Figure 5.6 shows the $(U_n - V_n)_{\rm rest}$ colors corrected for dust extinction. These were derived as in Bouwens et al. (2009), from the mean β vs. UV-luminosity trend and the classic Meurer et al. (1999) relation that relates the dust content with the UV-slope β according to:

$$A_{1600} = 4.43 + 1.99 \times \beta \tag{5.1}$$

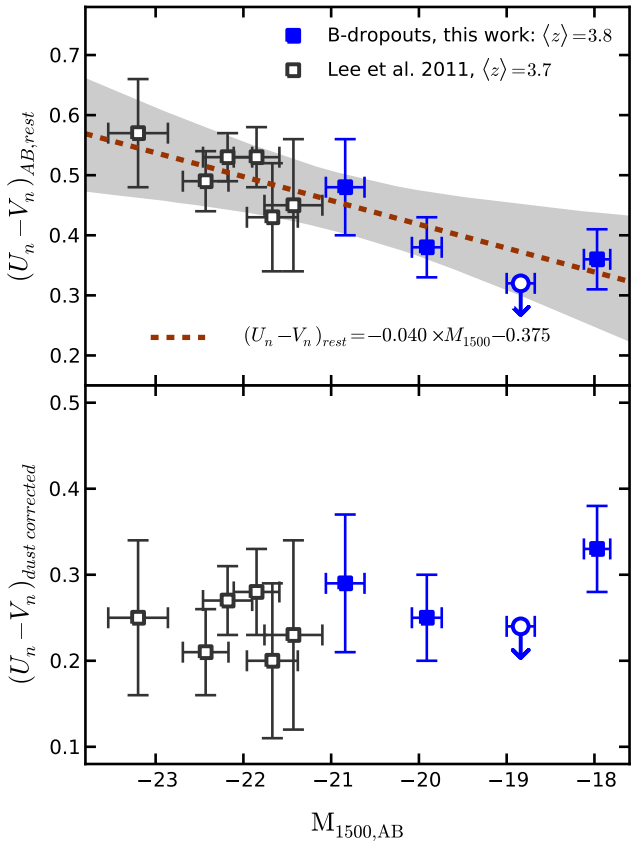

Figure 5.6: *Top:* Interpolated rest frame $(U_n - V_n)$ color as a function of M_{1500} for the $z \sim 4$ sources. Blue solid symbols and errorbars correspond to the colors derived for the new SEDs in this work. Similarly, we have derived interpolated $(U_n - V_n)_{\rm rest}$ colors for the SEDs presented in Lee et al. (2011a), dark open symbols and errorbars. A systematic trend to bluer $(U_n - V_n)_{\rm rest}$ colors with decreasing UV-luminosity is observed. The best fit trend of $(U_n - V_n)_{rest} = -0.040(\pm0.014) \times M_{1500} - 0.069(\pm0.293)$ is shown by the dashed line and the 95% confidence interval is shown by the gray area. The rest-frame $(U_n - V_n)$ colors were determined from best fits to the observed data based on the default template set from the code EAZY (Brammer et al. 2008). We have used ideal narrow band U_n and V_n filters that correspond to step functions of 100 Å width, centered at rest-frame 3500 Å and 5500 Å respectively. The upper limit ($2\,\sigma$), arises from the limitations of the template set which only includes $(U_n - V_n) > 0.3$ mags. The color of this SED is likely very close to this limit. *Bottom:* The same $(U_n - V_n)_{\rm rest}$ colors after being corrected for dust extinction. The corrections were derived from the median UV-slope β trends from Bouwens et al. (2009; 2011b) and the local Meurer et al. (1999) relation between β and dust extinction. The corrected colors of both samples show flat trends with luminosity.

where A_{1600} is the extinction in magnitudes at 1600 Å. A Calzetti et al. (2000) extinction curve is used to estimate the extinction at other wavelengths.

Table 5.2: Photometry Summary of Stacked SED

Ref. mag	N_{ERS}	N_{HUDF}	B_{435}	V_{606}	i_{775}	z_{850}	Y_{098}	Y_{105}	J_{125}	H_{160}	[3.6]	[4.5]
i_{775}						$z \sim 4$ $B-$dropouts						
25	35 / 72	0 / 4	33.0 ± 6.1	226.3 ± 15.3	356.2 ± 17.6	375.9 ± 21.9	359.9 ± 21.0	...	389.3 ± 30.2	467.9 ± 50.4	687.5 ± 50.2	635.4 ± 63.6
26	93 / 176	12 / 18	13.5 ± 2.3	106.6 ± 3.5	154.3 ± 4.2	153.2 ± 5.3	146.4 ± 6.3	142.4 ± 9.0	149.5 ± 5.5	162.0 ± 6.9	236.9 ± 13.8	246.4 ± 16.2
27	113 / 218	34 / 51	8.3 ± 1.3	46.8 ± 1.4	59.6 ± 1.7	53.6 ± 2.6	57.0 ± 3.1	54.0 ± 3.3	57.1 ± 2.3	62.0 ± 2.9	72.1 ± 5.5	61.8 ± 6.8
28	24 / 44	38 / 62	3.3 ± 1.2	25.0 ± 1.5	26.3 ± 1.4	27.3 ± 1.9	32.1 ± 4.3	21.3 ± 1.4	26.5 ± 1.8	29.3 ± 2.6	40.5 ± 5.0	35.7 ± 7.3
z_{850}						$z \sim 5$ $V-$dropouts						
25	4 / 9	0 / 0	-10.1 ± 11.7	47.2 ± 8.6	249.5 ± 49.4	305.1 ± 25.1	309.2 ± 25.2	...	315.6 ± 20.9	288.7 ± 21.4	681.9 ± 67.1	498.8 ± 50.2
26	26 / 40	3 / 4	-3.6 ± 3.6	17.0 ± 3.6	114.5 ± 11.1	130.5 ± 7.7	129.3 ± 11.3	126.7 ± 15.3	132.2 ± 7.5	140.2 ± 11.0	268.8 ± 26.0	202.3 ± 26.2
27	41 / 62	9 / 10	-1.1 ± 2.1	8.5 ± 1.4	58.7 ± 4.1	65.5 ± 3.5	69.1 ± 5.6	56.5 ± 9.4	67.4 ± 5.0	62.4 ± 5.2	95.7 ± 12.9	69.2 ± 10.4
28	6 / 12	9 / 14	-2.3 ± 2.1	2.6 ± 1.5	25.9 ± 4.2	25.2 ± 2.9	21.0 ± 10.4	22.0 ± 4.2	24.9 ± 3.3	27.7 ± 4.9	41.3 ± 15.9	34.2 ± 16.0
Y						$z \sim 6$ $i-$dropouts						
26	4 / 8	3 / 3	0.0 ± 3.9	-3.3 ± 3.6	10.4 ± 7.0	97.8 ± 15.5	116.9 ± 12.8	157.3 ± 24.1	124.9 ± 16.7	148.8 ± 26.3	255.4 ± 61.2	172.5 ± 51.6
27	12 / 17	3 / 6	-0.6 ± 3.5	0.8 ± 2.6	11.7 ± 6.6	71.2 ± 7.0	64.7 ± 7.4	49.9 ± 5.4	71.2 ± 6.4	72.3 ± 9.1	134.8 ± 24.6	84.2 ± 27.4
28	2 / 3	9 / 14	-2.7 ± 2.5	1.8 ± 2.0	2.6 ± 2.7	28.2 ± 4.7	29.7 ± 14.0	21.6 ± 2.9	27.5 ± 4.1	21.2 ± 3.9	27.1 ± 10.7	44.6 ± 17.3
H_{160}						$z \sim 7$ $z-$dropouts						
26	...	...	-3.2 ± 2.3	2.8 ± 2.3	-7.4 ± 4.7	23.5 ± 5.4	63.7 ± 7.7	...	129.7 ± 16.0	128.2 ± 17.0	262.0 ± 28.0	181.0 ± 37.0
27	...	...	-2.4 ± 0.8	-0.8 ± 0.6	2.2 ± 1.8	14.6 ± 2.3	49.1 ± 4.3	...	64.8 ± 4.1	57.0 ± 3.4	107.0 ± 16.0	83.8 ± 25.0
28	...	...	1.2 ± 0.8	0.4 ± 0.5	-0.1 ± 0.7	5.6 ± 1.1	27.2 ± 1.8	...	29.6 ± 2.0	24.5 ± 1.6	45.1 ± 9.5	39.3 ± 17.0

Notes. The median SEDs of high$-z$ galaxies in bins of observed UV-luminosity. The fluxes are in units of nJy. N_{HUDF} and N_{ERS} are the numbers of sources with reliable IRAC photometry over the total available in the given bin. The effective number of stacked images in a bin corresponds to $N_{ERS} + 2N_{HUDF}$. Only the ones with reliable photometry were considered in the stack. The $z \sim 7$ stacks were taken directly from Labbé et al. (2010a).

As can be seen from the figure, the dust corrected $(U_n - V_n)$ color is essentially constant with UV-luminosity. This again suggests that the main origin for the correlation of β with the UV-luminosity is an increasing dust content at brighter magnitudes. Otherwise we would expect some residual trend in the dust corrected color. This would be the case for example, if a strong age trend existed with UV-luminosity. As will be shown later, a similar flattening of the corrected colors is observed at all redshifts in the $-21 < M_{1500} < -18$ range.

5.5.2 The UV-to-optical Colors at Higher Redshift

We now extend our determination of the SED of high-z galaxies to $z \sim 5$ and $z \sim 6$, and combine our determinations with the stacked SEDs of sources at $z \sim 7$ recently presented in Labbé et al. (2010a). Figure 5.7 shows the SEDs at $4 \lesssim z \lesssim 7$. The expected mean redshifts of these samples correspond to $\langle z \rangle = 3.8, \langle z \rangle = 5.0, \langle z \rangle = 5.9$, and $\langle z \rangle = 6.9$, with typical spread in redshift of $\Delta z \pm 0.3$. The samples at each redshift have been split in bins of 1 mag, using as reference the observed magnitude in the band closest to 1500 Å (Table 5.2 contains the SEDs and information about the samples in each bin). Best fit BC03 models with CSF and $0.2\,Z_{\odot}$ metallicity are overlaid for reference. As explained in the previous section, we have excluded from the fitting the bands that are potentially biased (marked by the open symbols). As can be seen in this Figure, all these SEDs are remarkably similar and show sizable UV-to-optical colors.

The similarity of the SEDs can also be appreciated in Figure 5.8, where the SEDs from the different redshift samples have been grouped according to their approximate M_{1500} luminosities. The SEDs in the three M_{1500} bins have been re-normalized according to their M_{1500} luminosity and combined to produce over-sampled SEDs, which take advantage of the fact that the different filters probe different rest-frame wavelengths at the different redshifts. The combined SEDs show the typical flat UV slopes, but also rather flat colors in the rest-frame optical, albeit with a relatively large scatter. This scatter can in part be a consequence of the

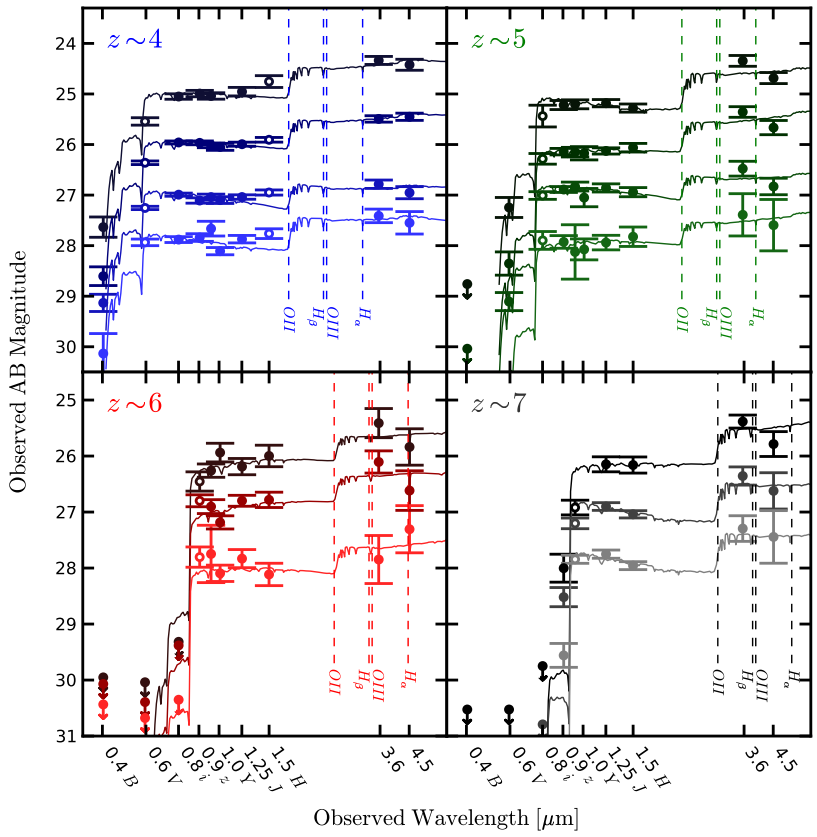

Figure 5.7: The stacked SEDs of galaxies in units of observed magnitudes (see also Table 5.2). The x-axis shows wavelength and the approximate filter that it corresponds to in our filter set for reference (notice that this filter set is different from the one in the x-axis of Figure 5.5). In the case of the optical bands, the errors were derived by bootstrap re-sampling the measured fluxes. The individual uncertainties were set to a minimum of 5% to account for systematic uncertainties in the filter to filter absolute calibrations. The errors in the IRAC bands were derived by bootstrap re-sampling the individual images and repeating the pixel by pixel median-stack process. In all cases, these errors on the median should include both the image noise and the uncertainty coming from variations within the population included in the stack. Simple best fit BC03 models with CSF are also included for reference. In the fitting process the redshifts were fixed to the median redshift of each sample, i.e.: $\langle z \rangle = 3.8$, $\langle z \rangle = 5.0$, $\langle z \rangle = 5.8$, and $\langle z \rangle = 6.9$ respectively. Due to the intrinsic redshift distribution of each sample, the median fluxes measured for bands near Lyman alpha or the Balmer break are likely biased and in consequence they were excluded from the fitting process (excluded bands are marked by the open symbols). The position of the most prominent possible emission lines in the rest-frame optical region of the SED are marked by the vertical dashed lines (assuming the mean redshift of each sample). At the different redshifts sampled here, different lines could be contaminating the continuum fluxes measured by the *Spitzer*/IRAC filters. The overall shape and UV-to-optical colors of the SEDs, however, remain remarkably constant with redshift. Some contribution of nebular emission lines is possibly hinted by the small relative excess of [3.6] over [4.5] fluxes observed in most SEDs at $z \gtrsim 5$ (the exception is the faintest bin at $z \sim 6$ which has very uncertain UV-to-optical colors due to the weak IRAC detections – see Figure 5.4).

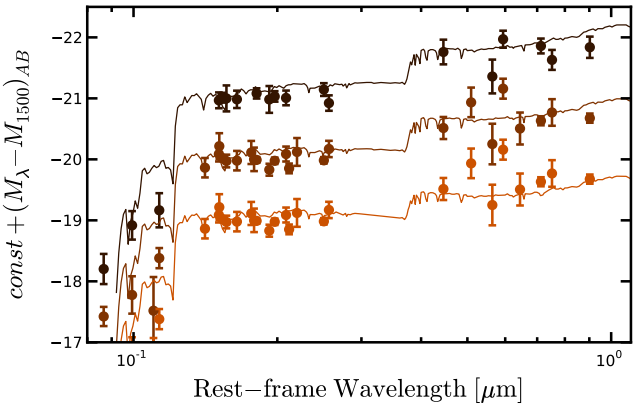

Figure 5.8: The SEDs of the combined samples in three bins of intrinsic UV-luminosity: $M_{1500} \sim -21, -20$, and -19. As seen in Figure 5.10, the UV-to-optical colors of the SEDs depend weakly on redshift. Here we perform the exercise of combining all the photometry from SEDs at different redshifts into a single SED. At different redshifts, our set of *HST*/ACS+WFC3/IR+*Spitzer*/IRAC filters probe different rest-frame wavelengths. The combined SEDs are plotted in terms of their magnitudes relative to M_{1500}, which is measured from the best power law fit to the UV continuum of each median SED. An offset magnitude of $-21, -20$, and -19 is added to reflect the approximate intrinsic magnitude of the SEDs that are being combined.

normalization which is done in the far UV, which effectively acts as the pivot point. Different emission lines that sometimes contribute flux in the IRAC bands, depending on the redshift, can also be contributing to this scatter.

Emission Lines in the Rest-frame Optical.

We first consider the implications if the sizable red $J_{125} - [3.6]$ colors that we observe are assumed to be exclusively measuring the stellar continuum in these high redshift galaxies. The red color would arise from large Balmer breaks, and would be indicative of evolved stellar populations. As can be seen in Figure 5.9a, the $J_{125} - [3.6]$ colors characteristic of these sources would then require fairly large ages of ~ 1 Gyr if no dust is allowed in the models (the model tracks in the Figure are CSF models). Allowing some reddening by dust (using in this case a Calzetti et al. 2000 law), reduces their ages considerably (Figure 5.9c). The amount of dust reddening is constrained however. Based on the UV continuum slopes typically observed in

Table 5.3: Rest Frame Magnitude and Colors

M_{1500}	$J_{125}-[3.6]$	$(U-V)_{\rm rest}$	$(U-V)_{dust-corr}$
	$z\sim4$ $B-$dropouts		
-20.84 ± 0.22	0.62 ± 0.12	0.48 ± 0.08	0.29
-19.91 ± 0.17	0.50 ± 0.07	0.38 ± 0.05	0.25
-18.84 ± 0.16	0.25 ± 0.09	>0.32	>0.24
-17.97 ± 0.15	0.46 ± 0.15	0.36 ± 0.05	0.33
	$z\sim5$ $V-$dropouts		
-21.14 ± 0.13	0.84 ± 0.13	0.48 ± 0.06	0.29
-20.21 ± 0.14	0.77 ± 0.12	0.46 ± 0.06	0.33
-19.46 ± 0.13	0.38 ± 0.17	0.31 ± 0.03	0.22
-18.39 ± 0.16	0.55 ± 0.44	0.42 ± 0.12	0.39
	$z\sim6$ $i-$dropouts		
-20.42 ± 0.19	0.78 ± 0.30	0.43 ± 0.12	0.37
-19.68 ± 0.13	0.69 ± 0.22	0.46 ± 0.10	0.43
-18.59 ± 0.14	-0.02 ± 0.46	0.40 ± 0.12	0.42
	$z\sim7$ $z-$dropouts		
-20.71 ± 0.20	0.76 ± 0.18	0.48 ± 0.11	0.35
-19.89 ± 0.12	0.54 ± 0.18	0.45 ± 0.12	0.40
-19.00 ± 0.12	0.46 ± 0.24	0.48 ± 0.16	0.53

Notes. Rest frame M_{1500} estimated from the best fit power-law to the rest-frame UV photometry. Possibly contaminated bands were ignored in the fit (see open points in Figure 5.7).

these galaxies (Bouwens et al. 2009), and using the $z=0$ Meurer et al. (1999) relation between this slope and the dust content, it has been shown that the reddening at $z\gtrsim4$ is typically $A_V\lesssim0.7$ mag. The reddening is likely to be even smaller at higher redshifts (Bouwens et al. 2009; 2011b). With this added constraint, the ages derived from SED fitting are generally estimated to be $300-400$ Myr (e.g., Yan et al. 2005, Eyles et al. 2005, Stark et al. 2009, González et al. 2010, Labbé et al. 2010a).

In our SEDs at $z\gtrsim5$ we also find that the $([3.6]-[4.5])$ color is consistently blue, with typical values of ~-0.3 mags (the only exception is the faintest $z\sim6$ bin but this color is very uncertain). This color is very hard to reproduce with a model with any star formation history that is based only on stellar continuum. The addition of dust only makes the comparison worse (Figure 5.9c,d). It should be noted, however, that the uncertainties in this color are considerable and that in most cases the observed color is formally consistent with the stellar continuum only

models.

It has been claimed (Schaerer & de Barros 2009; 2010) that, at some of these redshifts, particularly $z \sim 6$ and 7, the SEDs could be better fit by very young stellar population models ($\lesssim$ 10 Myr old) with moderate dust content and very strong nebular emission lines. These lines would dominate the rest-frame optical fluxes. As the galaxies are forming stars, it is likely that they have nebular emission lines, and so we have assessed whether emission lines could be influencing our fluxes and fits. The observed position of the most prominent optical nebular emission lines at each redshift is marked in Figure 5.7 by the dashed vertical lines (assuming the mean redshift of each sample). It can be seen that at the different redshifts involved, some of the rest-frame optical emission lines would lie within the IRAC [3.6] and [4.5] filters.

Atek et al. (2011) showed recently that at $z < 2.8$ there are sources that show emission lines with large enough equivalent widths to dominate the broadband fluxes in the optical. However, even for their sample of high-equivalent width sources, such objects are not very common. For the more typical cases, the lines that they find in their sample would have only moderate contributions to the IRAC broad bands, usually making them $0.2 - 0.3$ mags brighter. At higher redshifts, $3.8 \lesssim z \lesssim 5$, the work of Shim et al. (2011), based on spectroscopic redshifts and IRAC broadband photometry, finds similar results. They find that the sources in this redshift range show excess flux in [3.6] over [4.5], which the authors think can be explained by Hα emission. The majority of the sources in their sample have ([3.6] $-$ [4.5]) colors that are consistent with an Hα contribution of $0.2 - 0.3$ mags to the [3.6] filter, indicating moderate contributions from emission lines.

We consider the effects of a similar (moderate) contribution of emission lines to the colors of a 280 Myr old CSF model. For the purpose of this exercise we assume an Hα rest-frame equivalent width $\mathrm{EW_{rest}} = 300$ Å. At $z \sim 6$, this would increase the luminosity in the [4.5] filter by 0.23 mag. We only consider the strongest lines in the optical and assume the strength ratios presented by Anders & Fritze-v. Alvensleben (2003) for a $0.2\,Z_{\odot}$ metallicity

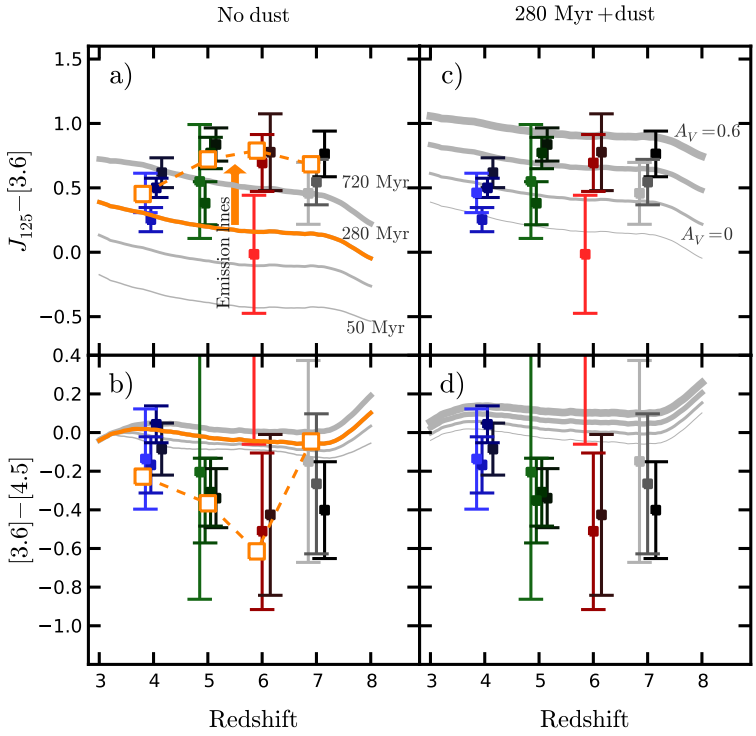

Figure 5.9: The observed colors of the median SEDs. Point colors correspond to Figure 5.7. The colors for the faintest bins at $z \sim 5$ and 6 are very uncertain due to the weak IRAC detections (see Figures 5.3 and 5.4). The measurements are slightly offset in redshift for clarity. a) Theoretical tracks for a BC03 CSF model without dust are included. The different lines correspond to ages: 50, 140, 280, and 720 Myr. The 280 Myr old track is highlighted. For these dust-free models, the $J_{125} - [3.6]$ color is more consistent with older galaxy populations in which there is a significant contribution of relatively evolved stars to the rest-frame optical light. The most likely age is lowered if flux from optical nebular emission lines is included in the appropriate IRAC band and redshift. As an example of the changes that can result from the inclusion of emission lines, the open squares (connected by the dashed line) show the effects of adding emission lines with $\mathrm{EW_{rest}}(\mathrm{OII}, \mathrm{H}\beta, \mathrm{OIII}, \mathrm{H}\alpha) = (189, 105, 670, 300)$ Å, respectively to the 280 Myr old track. b) Dust free tracks (for the same ages as in 9a) cannot reproduce the $[3.6] - [4.5] \sim -0.3$ colors observed at $z \gtrsim 5$. The inclusion of optical nebular emission lines, shown by the open squares connected by the dashed line can help reproduce such blue colors. c) As in a) but only the 280 Myr old track is shown with varying amounts of dust added. The tracks correspond, from bottom to top, to $A_V = 0.0, 0.2, 0.4$, and 0.6 mag using a Calzetti et al. (2000) extinction law. As expected, redder colors can be obtained for younger models if dust is allowed. Our independent analysis of the UV continuum slope (Bouwens et al. 2011b), constrains the amount of dust to $A_V < 0.7$ mag for $z \gtrsim 4$. With this added constraint, the ages of high-z galaxies are generally estimated to be $\gtrsim 400$ Myr when the emission line contribution is taken to be zero. d) As is clear here, the addition of dust makes it even harder for the stellar continuum only models to reproduce the blue $[3.6] - [4.5]$ colors observed in the SEDs. This suggests that an optical nebular emission line component to the total flux may be needed.

system. These correspond to $\mathrm{EW_{rest}(OII, H\beta, OIII)} = (189, 105, 670)$ Å, respectively. The open squares in Figure 5.9a,b, correspond to the median colors for a model like the one described (the median takes into account the expected redshift distribution of each sample).

As can be seen in Figure 5.9a, the main effect of the contribution from the emission lines is that it allows for significantly younger ages to reproduce the $J_{125}-[3.6]$ colors (by roughly a factor of two). Since this implies lower stellar continuum fluxes than previously assumed, this would also result in lower best fit stellar masses than previously estimated for galaxies at these redshifts (by a similar factor). Simultaneously, given the line ratios and the redshift distributions expected for these samples, a model like this can also help in reproducing the blue [3.6]-[4.5] colors of the SEDs at $z \gtrsim 5$ (Figure 5.9b). While formally models with just stellar continua can fit the data, given the current large uncertainties, such colors are hard to obtain with stellar continuum only models. It is more likely that some degree of contribution of emission lines provides a better solution.

The assessment presented here is necessarily very simplistic, given the current uncertainties, and is only meant to show the possible effects of emission lines on the colors of these galaxies. Better estimates of the contribution of these lines and its effects on the properties derived from SED fitting will depend on the actual strengths and ratios of the lines. Moderate improvement can be achieved if more precise redshifts were known for these sources; such data does not exist at this time for such faint high redshift galaxies and so this remains an open question until improved spectroscopic capability becomes available.

UV-to-optical color vs. luminosity.

The trend of redder UV-to-optical colors for brighter UV-luminosities presented in Figure 5.6 for the $z \sim 4$ sample can also be observed for the other samples. In fact, within the uncertainties in the color determination, the $J_{125} - [3.6]$ vs M_{1500} trend is roughly the same at $z \sim 5$ and 6 (Figure 5.10, *top*). This is particularly remarkable in view of the fact that this color

is an observed color, not a rest-frame color, and in consequence is probing different wavelengths for the different samples. This shows again how similar and flat these SEDs are. If all the SEDs are considered simultaneously, a trend of $J_{125} - [3.6] = -0.17(\pm 0.07) \times M_{1500,\mathrm{AB}} - 2.80(\pm 2.43)$, is found. For simple CSF models, this trend implies a variation in stellar M/L ratio. González et al. (2011) find that at $z \sim 4$, this variation is a factor $\sim \times 5$ between $M_{1500} = -18$ and $M_{1500} = -21$. So, despite the steep UV-luminosity functions characteristic at $z \gtrsim 4$, the contribution of the faintest sources to the total stellar mass density is more modest than their contribution to the star formation rate density.

Similar to the analysis performed at $z \sim 4$, we have derived rest-frame $(U_n - V_n)$ colors for the median SEDs at all redshifts. These colors are shown in Figure 5.10. The trend with UV-luminosity has large scatter and low significance but is systematic in the sense that brighter sources are redder in $(U_n - V_n)_{\mathrm{rest}}$. A fit to the rest-frame colors as a function of M_{1500} of all redshifts simultaneously, results in $(U_n - V_n) = -0.030(\pm 0.027) \times M_{1500} - 0.156(\pm 0.536)$, shown as the brown dashed line in Figure 5.10 (*center* panel). The $z \sim 4$ sample has already been shown to have this trend in the Section 4.5.1. We check that this trend in fact exists in the rest of the sample. A simultaneous fit to the rest of the sample, excluding the $z \sim 4$ points, results in a slightly flatter but consistent relation $(U_n - V_n) = -0.024(\pm 0.039) \times M_{1500} - 0.039(\pm 0.783)$. The slope derived for the full sample is in very good agreement with the -0.04 slope found for the $z \sim 4$ data only, also plotted for reference as the black dashed line in Figure 5.10. The latter trend included the bright sample of Lee et al. (2011a) and is consistent within the uncertainties with the fit to all the points.

In the bottom panel of Figure 5.10 we present an estimate of the reddening corrected $(U-V)$ colors. The reddening corrections are derived assuming a Calzetti et al. (2000) extinction curve and using the local Meurer et al. (1999) relation between dust reddening and the UV-slope β (Equation 6.1). The values of β are extracted from the best fit trends measured by Bouwens et al. (2011) at the corresponding luminosities. These corrected colors show large scatter around

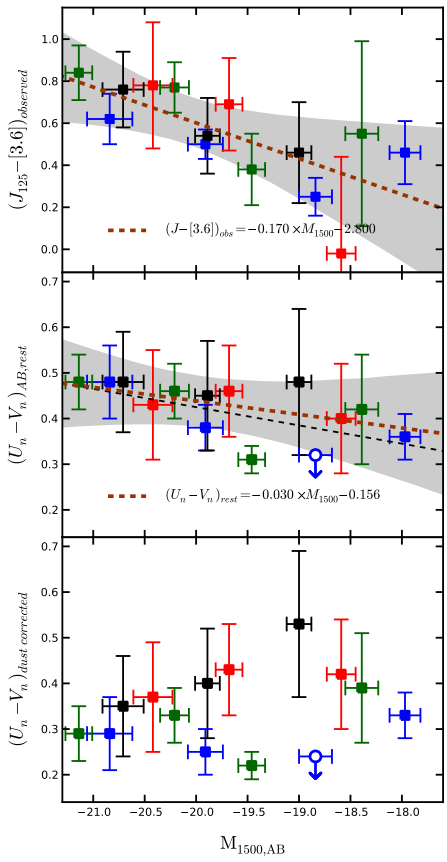

Figure 5.10: *Top:* UV-to-optical color as a function of M_{1500}. Blue symbols correspond to the $J-[3.6]$ colors of the $z\sim4$ SEDs; green: $z\sim5$; red: $z\sim6$; and black: $z\sim7$. Despite the sizable scatter, a systematic trend to redder UV-to-optical colors with increasing luminosity is observed at all redshifts. At the same time, there is no clear indication of a systematic trend with redshift. The dashed line is a best fit to all the points (all redshifts simultaneously): $J_{125}-[3.6]=-0.17(\pm0.07)\times M_{1500,\rm AB}-2.8(\pm1.43)$, and the gray area corresponds to the 95% confidence interval. This is different to Figure 5.6 in that this Figure shows the directly observed colors rather than interpolated rest-frame colors. In fact it is remarkable that this observed color, which samples different wavelength regions of the SED at the different redshift, remains fairly constant. This is probably an indication that the rest-frame optical colors measured by IRAC are fairly flat. *Center:* The interpolated rest frame (U_n-V_n) colors (Section 4.5.1). The best fit trend to all the data is shown by the brown dashed line (slope= -0.030 ± 0.027). If the $z\sim4$ sample is excluded from the fit, the trend is slightly shallower (slope= -0.024 ± 0.039). For comparison, the black dashed line shows the best fit to the $z\sim4$ data only, as shown in Figure 5.6, this trend is in very good agreement with the trend exhibited by the full sample. *Bottom:* The $(U_n-V_n)_{\rm rest}$ colors after being corrected by dust extinction following a simple prescription based on the UV-slopes and the local Meurer et al. (1999) relation. Except for the $z\sim7$ SEDs (which have a much steeper β vs. UV-luminosity relation), the dust corrected colors of all SEDs seem to show a flat trend (although the scatter is large). This indicates that a change in dust is enough to explain the change in colors, both in the UV and the UV-to-optical. In particular, no age dependence on luminosity seems to be required.

$(U-V)_{\rm rest,corrected} \sim 0.3$ but there is no indication of a residual trend with UV-luminosity except for the $z \sim 7$ sample (black symbols). This may indicate again that at $4 \lesssim z \lesssim 6$, the evolution can be fully explained by a change in dust content and there is no strong evolution in the ages of these sources as a function of UV-luminosity. This is consistent with the report by Stark et al. (2009) based on stellar population modeling of slightly brighter LBGs in this redshift range. It is also consistent with the predictions from the hydrodynamical simulations of Finlator et al. (2011), which show no trend of age with UV-luminosity.

At $z \sim 7$ there seems to be a residual trend in $(U_n - V_n)_{\rm rest,corrected} \sim 0.4$ vs. UV-luminosity in the sense that brighter sources have systematically bluer intrinsic $(U_n - V_n)$ colors. In principle, this could indicate that the brighter sources are actually younger than the fainter sources, which would be difficult to imagine. Alternatively, it is possible that the simple dust corrections (calibrated at $z = 0$) are not adequate at these high redshifts, due, for example, to changes in the IMF, metallicity, or escape fraction, all of which could alter the UV-slope β for a given dust content. It should also be noted that the β vs. UV-luminosity at $z \sim 7$ is considerably steeper than at the other redshifts (Bouwens et al. 2011b), and so the corrections to the $(U_n - V_n)_{\rm rest}$ vs. UV-luminosity trend are more extreme. Nevertheless, the uncertainties are sufficiently large that also the $z \sim 7$ trend is fully consistent with being constant.

5.6 Summary

Determining the rest-frame UV-to-optical colors of individual UV-faint galaxies at $z \gtrsim 4$ is challenging. At such redshifts the rest-frame optical lies at $\lambda > 2.5$ microns in the mid-IR and so it is hard to measure at the extremely faint magnitudes typical of galaxies in the first 1.5 Gyr. To gain insight into the typical spectral properties of $z \sim 4-6$ galaxies, we have taken advantage of the large samples of $z \sim 4-6$ sources found in the deep *HST* ACS and WFC3/IR images of the ERS and HUDF fields. The *HST* data give us rest-frame UV fluxes. We then

use *Spitzer*/IRAC [3.6] and [4.5] micron data from the deep GOODS survey of these fields to get rest-frame optical fluxes by stacking the IRAC images and determining median flux values. This allows us to determine the SEDs of these galaxies covering both the rest-frame UV and the optical. These SEDs represent a first comprehensive study of the rest-frame UV-to-optical properties of $z \gtrsim 4$ galaxies as a function of both redshift and UV-luminosity down to very faint limits.

At $z \gtrsim 4$ we have also combined our faint SEDs with the $L > L^*$ stacks presented in Lee et al. (2011a). This allows us to assess the colors of $z \gtrsim 4$ sources over an unprecedentedly large range of luminosities. Our main findings are as follow:

- At $z \gtrsim 4$ the $(U_n - V_n)$ rest-frame color (interpolated from the data using a fitted SED from a set of templates is of $(U_n - V_n) \sim 0.4$ mags. There is a shallow but systematic trend of redder colors for brighter UV-luminosities over the range $-23 \lesssim M_{1500,\mathrm{AB}} \lesssim -17.5$ (Figure 5.6, Section 4.5.1). A linear fit to this trend is $(U_n - V_n)_{\mathrm{rest}} = -0.04 \times M_{1500} - 0.38$

- The SEDs of star forming galaxies at $4 \lesssim z \lesssim 7$ are remarkably similar at all luminosities from $-23 \lesssim M_{1500,\mathrm{AB}} \lesssim -17.5$, showing fairly flat rest-frame UV and rest-frame optical colors (Section 4.5.2 and Figures 5.7, 5.8 and 5.10). At a given redshift, there are weak indications of a subtle trend for redder colors for brighter sources. A simple fit to the data at all redshifts simultaneously results in $(U_n - V_n)_{\mathrm{rest}} = -0.03 \times M_{1500} - 0.16$ (Figure 5.10 *center*, Section 4.5.2).

- The UV-to-optical color, as measured by the observed $J_{125} - [3.6]$, color remains fairly constant with redshift, despite the *Spitzer*/IRAC bands probing different wavelength regions of the SED (Figure 5.10 *top*). This suggests that the optical colors are fairly flat at all redshifts $z \sim 4-7$, although there is significant scatter, which can be caused by optical emission line contamination to the IRAC filters.

- The $z \gtrsim 5$ SEDs show consistently blue $[3.6]-[4.5] \sim -0.3$ colors. This is hard to reproduce

with models that only include stellar continuum, although it is still formally possible given the current uncertainties. Nonetheless, it is probably better explained with moderate flux contributions from optical nebular emission lines in the two IRAC bands. Including some contribution from emission lines leads to lower best fit ages and lower stellar masses than previously estimated for galaxies at these redshifts. Changes of a factor 2 could well result, but we would caution that detailed assessments are not yet possible with the current data.

- We derive dust-corrected $(U-V)$ colors using a simple dust correction based on the median UV-slope β vs. UV-luminosity relation from Bouwens et al. (2009; 2011b) and the Meurer et al. (1999) relation (Figure 5.10, *bottom*). The dust-corrected UV-to-optical colors at $4 \lesssim z \lesssim 6$ are $(U-V) \sim 0.3$ mags. They do not appear to depend on UV-luminosity. This may suggest that moderate changes in the dust content of galaxies can explain the color dependency observed both in the UV-slopes and the UV-to-optical colors. In particular, it seems that no age evolution is required to match this color dependency.

The recent deep and ultra-deep *HST* ACS and WFC3/IR imaging programs over the GOODS-S field have resulted in large samples of $z \sim 4$ galaxies. Taking advantage of these large samples, along with a careful stacking analysis, we present a first comprehensive study of the typical SEDs over the rest-frame UV and the rest-frame optical for faint star forming galaxies in the $4 \lesssim z \lesssim 7$ redshift range. The stacked SEDs allow us to study the UV-to-optical colors of high-z star forming galaxies down to very low luminosities. We find a mild trend to bluer color at fainter luminosities. Interestingly, these stacked SEDs also show a remarkable similarity across redshift in a period of considerable stellar mass growth from about 0.8 Gyr to 1.5 Gyr, suggesting a smooth self-similar mode of evolution at $z \sim 7-4$.

Chapter 6

The Specific Star Formation Rate at High-z

6.1 Introduction

Large samples of Lyman Break Galaxies (LBGs) have allowed for the study of the properties of high redshift galaxies up to $z \sim 8$ (e.g., Bouwens et al. 2011b;c, Dunlop et al. 2012, Finkelstein et al. 2011; 2010, González et al. 2010; 2011, Labbé et al. 2010a;b, Lee et al. 2011b, McLure et al. 2010; 2011, Oesch et al. 2010b; 2012, Papovich et al. 2011, Schaerer & de Barros 2010, Stark et al. 2009, Wilkins et al. 2011). These samples are the result of large investments on high quality *Hubble Space Telescope* (*HST*) data over deep fields like GOODS (Giavalisco et al. 2004) that have rich complementary multi-wavelength coverage. Several studies have explored the observed UV and optical colors of these galaxies. Through the standard technique of synthetic stellar population modeling of the observed SEDs, the physical properties of these galaxies, such as the stellar mass ($M_{\rm star}$), star formation rate (SFR), dust attenuation, age, etc, have also been explored (e.g., Yan et al. 2006, Eyles et al. 2005, Stark et al. 2009, González

et al. 2010; 2011, Papovich et al. 2011, Lee et al. 2011b, Bouwens et al. 2009; 2011b).

These studies have shown that, at rest-frame UV and optical wavelengths where LBGs are more amenable to observations, the SEDs show very similar colors with weak trends of bluer colors as a function of decreasing UV-luminosity and increasing redshift (Bouwens et al. 2009; 2011a, Wilkins et al. 2011, Finkelstein et al. 2011; but see also Dunlop et al. 2012). As a direct consequence of this, the physical properties estimated through SED fitting, using simple models, are also remarkably similar.

Particularly intriguing are the results that indicate that the specific star formation rate (sSFR) of sources with a given $M_{\rm star}$ remains approximately constant from $z \sim 2$ to $z \sim 7$ (Stark et al. 2009, González et al. 2010, McLure et al. 2011). In particular, González et al. (2010) shows that for sources with $\rm M_{star} = 5 \times 10^9\,M_{\odot}$, the sSFR shows no evidence for significant evolution ($\rm sSFR \sim 2\,Gyr^{-1}$) from $z \sim 7$ to $z \sim 2$. Such a result is at odds with the fairly generic theoretical expectation that the sSFR should decrease monotonically with cosmic time (e.g., Weinmann et al. 2011, Khochfar & Silk 2011).

From the stellar population modeling perspective, there are several uncertainties that can affect the determinations of the sSFR and it is not the intention of this paper to explore them all exhaustively. For example, a systematic variation of the IMF as a function of redshift, could mean that the approximately constant colors exhibited by the SEDs of LBGs derive from sources with varying ages, and in particular SFRs and stellar masses, indicating a varying sSFR as a function of redshift. Although it is interesting to investigate the effects of such changes, the study of the IMF at these high redshifts remains still far from our reach and the conclusions would be largely speculative. There are, in the meantime, some other more obvious consistency checks whose effects on the determination of the sSFR can and need to be studied.

The first of such checks regards the treatment of reddening by dust on the derived physical properties. In the original works that showed a plateau in the sSFR, the SFRs corresponded to values derived using the Madau et al. (1998) relation between UV-luminosity and SFR. The

dust corrections necessary to obtain the intrinsic UV-luminosities, however, were assumed to be negligible. The very blue UV-colors exhibited by $z > 4$ LBGs support such an assumption, since even trace amounts of dust would result in colors redder than observed. Further complicating the situation, the effects of age largely mimic the effects of dust at these wavelengths, making it hard to break the degeneracy. The assumption results justifiable in view of the complications and the evidence for low dust contents, but the inconsistency remains.

More recent determinations of the UV colors have indicated a somewhat steeper dependency of this color with UV-luminosity and redshift, suggesting that the dust corrections could be larger for the bright sources at $z \sim 4$. Bouwens et al. (2011b) derives a correction to the UV-luminosities based on these new UV color trends and this correction is later folded into the sSFR measurements. As a result, the sSFR at $z \sim 4$ is larger by ~ 0.4 dex, in principle showing a monotonically decreasing behavior from $z \sim 4$ to $z \sim 0$, in better agreement with simulations. At the same time, however, the same corrections are smaller at higher redshifts, now suggesting a possible turn over in the sSFR as a function of redshift.

In the meantime, the derivation of $M_{\rm star}$ for these sources, the other ingredient in the sSFR, is done from the SED fitting with dust reddening as a free parameter, not necessarily consistent with the assumptions of no-dust or with the later reddening corrections derived from the UV colors. This is, in principle, not expected to introduce huge differences, due to the fact that $M_{\rm star}$ from SED fitting depends only weakly on most modeling assumptions, including reddening, but the effect could be systematic and it is important to explore whether it can help bring to agreement the sSFR determinations derived from population modeling (observationally motivated) and the theoretical expectations from simulations.

Another source of tension in the assumptions made to derive $M_{\rm star}$ and the SFR is the choice of star formation history (SFH). As it is currently not possible to constrain the SFH of high-z LBGs from the observational data available, it has to be fixed to a reasonable function to create the grid of synthetic models. The generally assumed options are usually

smooth SFH histories, either with a constant star formation rate (SFR) or with a SFR that declines exponentially with time (characterized by timescale τ, i.e., SFH(t) $\propto e^{-t/\tau}$). Both these assumptions violate the observed evolution of the UV-luminosity function (UV-LF). Under the general assumption of smooth SFHs, the UV-luminosity of galaxies can be directly related to the SFR. Several studies agree now in that the characteristic luminosity (L^*) of the UV-LF increases monotonically with time from $z \sim 8$ to $z \sim 3$ (Bouwens et al. 2007; 2011a, Oesch et al. 2010b). Smit et al. (2012) recently show that the SFR function indicates larger mean SFR at later times, as expected from the increase in UV-luminosity. This evidence suggests a typical SFH which, if smooth, is better characterized by a rising SFR as a function of time, probably well represented by an exponential with a characteristic timescale $\tau \sim 500$Gyr (Papovich et al. 2011; Oesch et al, in preparation). Furthermore, this is in very good agreement with the predictions of numerical simulations (e.g., Finlator et al. 2011)

Other complications arise from the fact that the Madau et al. (1998) relation between SFR and UV-luminosity generally used to estimate SFR, assumes a constant star formation (CSF) history and ages above 100 Myr. This conversion may break down, particularly if a considerable number of sources exhibit ages below 100 Myr.

In this paper we attempt to bring the aforementioned issues into agreement, exploring the effect of dust reddening in the UV-colors, SFRs, and $M_{\rm star}$ measurements, as well as the effects of choosing a SFH that better matches the evolution of the UV-LF. The goal is to make estimates for the physical properties of $z > 4$ LBG that use empirically motivated assumptions that better match a larger range of observations. We plan to investigate whether this new set of assumptions still shows an approximate plateau in the sSFR at $z > 2$ or shows evidence for an increase toward high redshift as predicted by theory.

We now provide a brief plan for this paper. In Section 2, we briefly describe the observational data and selection criteria used here. In Section 3, we describe our approach to stellar population modeling, detailing the specific assumptions that we make and the effects

these assumptioins have on the physical properties we derive for LBGs. In Section 4 we present the new measurements of the sSFR at high-z. We discuss the results in 5, and summarize our findings in Section 6.

Throughout, we use a (H_0, Ω_M, Ω_Λ) = (70 km s^{-1}, 0.3, 0.7) cosmology when necessary and we quote all magnitudes in the AB system (Oke & Gunn 1983).

6.2 Data

This work is based on a large sample of star forming galaxies in the $z \sim 4-7$ redshift range found using the Lyman Break technique (Steidel et al. 1996) in the ultra-deep HUDF/WFC3 field (e.g., Oesch et al. 2010b) and the deep Early Release Science (ERS; Windhorst et al. 2011) fields. Both fields have deep *HST*/ACS (Giavalisco et al. 2004) and WFC3/IR imaging, as well as the 23 h *Spitzer*/IRAC data from the GOODS program (Giavalisco et al. 2004). The sample was already presented in González et al. (2011), Bouwens et al. (2007), and Bouwens et al. (2011b) but we provide a short summary here.

6.2.1 *HST* ACS and WFC3/IR photometry and sample selection

Over the ERS field, both the ACS optical ($B_{435}V_{606}i_{775}z_{850}$) and the WFC3/IR ($Y_{098}J_{125}H_{160}$) images from *HST* reach depths of $\sim$ 28 mag ($5\,\sigma$ measured on 0.″35-diameter apertures). In the HUDF field, the ACS optical data ($BViz$) are $1.5-2$ mags deeper, and the WFC/IR data ($Y_{105}J_{125}H_{160}$) are 1.5 times deeper than the ERS. The HUDF was observed with the Y_{105} filter instead of the Y_{098} filter used in the ERS.

The *HST* photometry for these sources was performed using the SExtractor code (Bertin & Arnouts 1996). The images were registered to a common frame and then PSF-matched to the H_{160}-band data. SExtractor was run in double-image mode with the detection image constructed from all images with coverage redward of the relevant Lyman break. Fluxes

Table 6.1: Sample Summary

Field	$z \sim 4$	$z \sim 5$	$z \sim 6$
ERS	270 / 524	77 / 123	20 / 32
HUDF	137 / 205	41 / 55	38 / 51
TOTAL	407 / 729	118 / 178	58 / 83

Notes. Number of sources in our $z \sim 4$, $z \sim 5$, and $z \sim 6$ samples. IRAC photometry of these sources requires fitting and subtraction of the flux from surrounding foreground neighbors. This is not possible in all the cases. The table shows the number of sources in our sample with clean IRAC photometry over the total number of sources in these samples.

are measured using Kron-style photometry. The criteria used to select sources are as follows (for details and contamination rates please refer to Bouwens et al. 2007): $z \sim 4$ B-dropouts:

$$(B_{435} - V_{606} > 1.1) \ \wedge \ [B_{435} - V_{606} > (V_{606} - z_{850}) + 1.1]$$

$$\wedge \ (V_{606} - z_{850} < 1.6).$$

$z \sim 5$ V-dropouts:

$$\{[V_{606} - i_{775} > 0.9(i_{775} - z_{850}) + 1.5] \ \vee \ (V_{606} - i_{775} > 2)\}$$

$$\wedge \ (V_{606} - i_{775} > 1.2) \ \wedge \ (i_{775} - z_{850} < 1.3).$$

$z \sim 6$ i-dropouts:

$$(i_{775} - z_{850} > 1.3) \ \wedge \ (z_{850} - J_{125} < 0.8).$$

The combined samples contain a total of 729 sources at $z \sim 4$, 178 at $z \sim 5$, and 83 at $z \sim 6$ (see Table 6.1).

6.2.2 *Spitzer*/IRAC photometry

While the *HST*/ACS and WFC3/IR data allow us to find LBGs at $z \gtrsim 4$ and to study their rest-frame UV light, data from the *Spitzer*/IRAC camera provides valuable constraints in the rest-frame optical regions of the SED of these galaxies. These constraints are very important to derive reliable stellar masses from SED fitting (Papovich et al. 2001, Labbé et al. 2010a).

The HUDF and the ERS fields were imaged with *Spitzer* in the four IRAC channels as part of the *Spitzer* GOODS program (Giavalisco et al. 2004). In this work we only make use of the two most sensitive channels centered at [3.6] and [4.5] μm respectively. The images have integrations of ~ 23.3 h (the HUDF was imaged twice). The depths of the images were measured dropping $2\farcs5$-diameter apertures in empty regions of the image and determining the RMS. After applying a $1.8\times$ flux correction to account for the light outside such aperture in the case of a point source, the depths correspond to 27.8 mag ($1\,\sigma$) for a single 23.3 h image in the [3.6] channel and 27.2 mag for the [4.5] channel.

The size of the IRAC PSF, however, is sufficiently broad that it is not appropriate to use standard photometric techniques on our sample of faint LBGs. The flux within an aperture is expected to be contaminated by flux from neighboring sources spilling over onto the same aperture. Many of the neighboring sources are in general brighter and the contaminating fluxes can be significant. The availability of higher resolution images of the sky (though at different wavelengths) with *HST* allows us to model the source and its neighbors and subtract off the expected contaminating flux in our apertures. This method has already been described in several previous works (Labbé et al. 2006; 2010a;b, González et al. 2010; 2011, Wuyts et al. 2007, de Santis et al. 2007). After the area around the source has been cleaned from the flux of neighbors, we perform standard aperture photometry using $2\farcs5$-diameter apertures. An aperture correction is derived from the higher resolution "*template*" image, in this case the WFC3/IR H_{160} image. This image is convolved to the resolution of IRAC and an aperture correction factor is estimated for a $2\farcs5$-diameter aperture. This correction factor is then applied to the fluxes measured with IRAC and involves multiplying the flux of sources (in $2\farcs5$-diameter apertures) by 1.8 in both the [3.6] and [4.5] IRAC channels, consistent with the correction one would apply to point sources.

The cleaning procedure cannot always produce acceptable models of the source and neighbors, resulting in poor subtractions for approximately 40% of the cases. The individual *cleaned* stamps were inspected by hand and those with poor subtractions were not included

in the subsequent analysis. This criteria mostly depends on the feasibility of modeling the neighboring sources, and as a consequence, it is not expected to introduce any significant biases.

6.3 Stellar Population Modeling

It has been customary to study the physical properties of high-z galaxies by comparing their observed UV and optical SEDs with synthetic stellar population (SSP) models. The quality of the flux constraints generally not the adequate to constrain all model parameters simultaneously. In particular, models with a variety of metallicities, initial mass functions, and star formation histories can all reproduce the flux constraints almost equally well. As a result, these model parameters must be constrained independently or fixed to reasonable values. In the following analysis we have assumed a Salpeter (1955) IMF with cutoffs at 0.1 and 100 $M_{\odot}$.

It is expected, that the metallicities of high-z galaxies be somewhat lower than that of local galaxies. For example, Maiolino et al. (2008), from a small sample of $z \sim 3.5$ galaxies determines gas metallicities of $\sim 0.2\,Z_{\odot}$. A number of other observational studies have found similar metallicities (e.g., Pettini et al. 2000), and $0.2\,Z_{\odot}$ is also expected in many cosmological hydrodynamical simulations (e.g., Finlator et al. 2011).

In our analysis we have assumed a fixed metallicity of $0.2\,Z_{\odot}$. The SFRs and stellar masses, which are the focus of this work, have only a weak dependency on this assumption.

For the SFHs, most early studies have generally assumed models with SFRs that decline exponentially as a function of time with a characteristic timescale τ left as a free parameter. The particular case $\tau \to \infty$, which corresponds to models with constant star formation (CSF), is sometimes used as the fiducial model. Because in a smooth SFH the UV-luminosity can be directly linked to the SFR, these SFHs would predict a UV-LF that shifts to brighter luminosities at increasing redshift (or one that remains constant in the CSF case), which is at odds with the current determinations of the UV-LF at $z > 4$ (Bouwens et al. 2007, McLure et al. 2009,

Oesch et al. 2010b, Bouwens et al. 2011b) . If the SFHs, are in fact smooth, then the observed overall dimming of the UV-LF predicts a mean SFH that is better characterized by a rising SFR (Papovich et al. 2011, Stark et al. 2009, Reddy et al. 2012). Oesch et al. (in preparation), shows that the evolution of the UV-LF can be well reproduced by an exponentially rising SFH with a characteristic timescale $\tau \sim 500\,\mathrm{Myr}$ (see also Papovich et al. 2011). In deriving the physical properties of galaxies in our samples, we will look in detail at the extent to which these parameters depend on whether we assume a constant or rising star formation (RSF) history. We particularly examine the effects on sSFR or the evolution of the sSFR with redshift.

6.3.1 Reddening

In addiction to the necessary simplifying assumptions described at the beginning of this section, other complications remain in the SED fitting process. In particular, it is known that the effects of reddening produced by dust and the reddening produced as a consequence of the aging of the population are degenerate. This does not have a large impact on the stellar masses, which generally remain constrained within $\sim 0.3\,\mathrm{dex}$ for a range of ages, but the varying dust corrections have a direct impact on the determination of the SFRs.

This degeneracy cannot be broken with the current data. The color dependencies observed as a function of luminosity for both the UV and the UV-to-optical colors, suggest that a simple relation between the UV color and the dust reddening like the Meurer et al. (1999) law may be appropriate.

Figures 6.1 and 6.2 show the observed colors of our $z \sim 4-6$ samples. The top panel of Figure 6.1 shows the observed $_{i775} - [3.6]$ color as a function of observed [3.6] mag. The different symbols are used to divide the IRAC detected ($2\,\sigma$, solid blue circles), the marginal detections ($1-2\,\sigma$, open squares), and the non-detections (open gray circles). The histogram shows the color distribution of the sample. The two solid horizontal lines show the minimum color (corresponding to a $> 10\,\mathrm{Myr}$ old population) and maximum color (set by the age of the

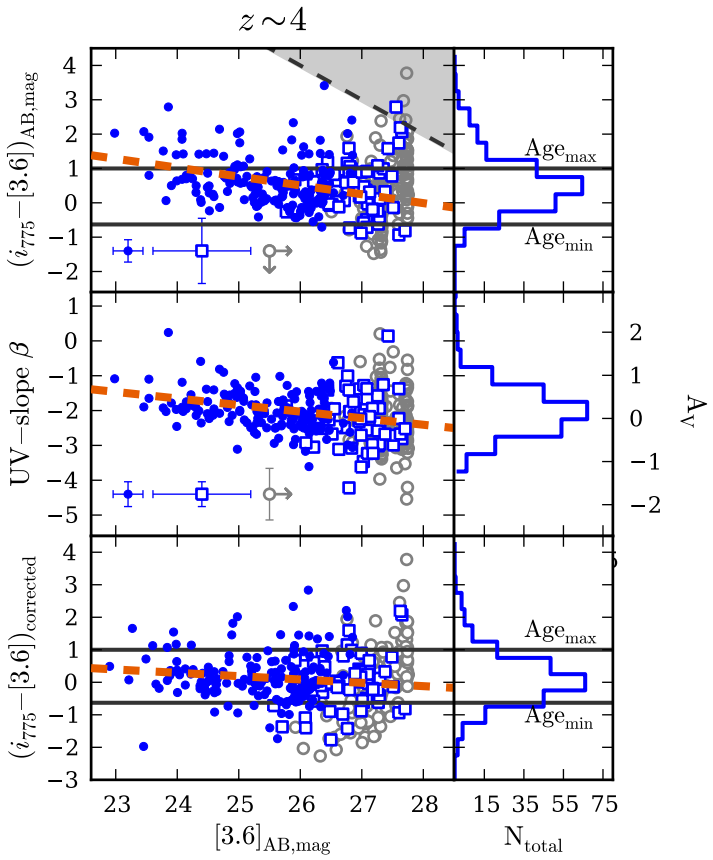

Figure 6.1: The observed colors of $z \sim 4$ LBGs. Only sources with reliable IRAC photometry are included (see text, section 2.2). In all panels the solid blue circles correspond to sources that are detected in IRAC [3.6] ($> 2\,\sigma$), open squares are used for marginally detected sources ($1-2\,\sigma$), and gray open symbols are for IRAC-undetected ($< 1\,\sigma$ limits) sources. The histograms in the right panels show the color distributions. *Top:* The $i_{775} - [3.6]$ color as a function of [3.6] mag. The dashed line in the top right corner corresponds to the limiting magnitudes probed by our *HST+Spitzer* observations. The three symbols in the lower left show the typical uncertainties. The solid horizontal lines show the minimum and maximum color for a dustless stellar population with a CSF history and ages between 10 Myr and the age of the universe at $z = 3.5$. The dashed thick line is a fit to the detected sources only and shows a trend of redder colors for brighter galaxies. *C*enter: The UV-slope β ($f_\lambda \propto \lambda^\beta$) determined from a linear fit to the available *HST* photometry of each source. This color also shows a trend of redder colors for brighter sources that is consistent with previous reports (e.g. Bouwens et al. 2011b). In our stellar population modeling we assume that this trend is caused exclusively by a varying amount of dust reddening (Meurer et al. (1999) relation, Eq. 6.1). *B*ottom : The $i_{775} - [3.6]$ color after dust reddening corrections are applied. These corrections are derived from the UV slope only. Much of the trend of redder colors for brighter sources disappears after this correction is applied, and most sources can be modeled without the addition of dust to the CSF models. The residual trend could be caused by a weak trend in age vs. luminosity.

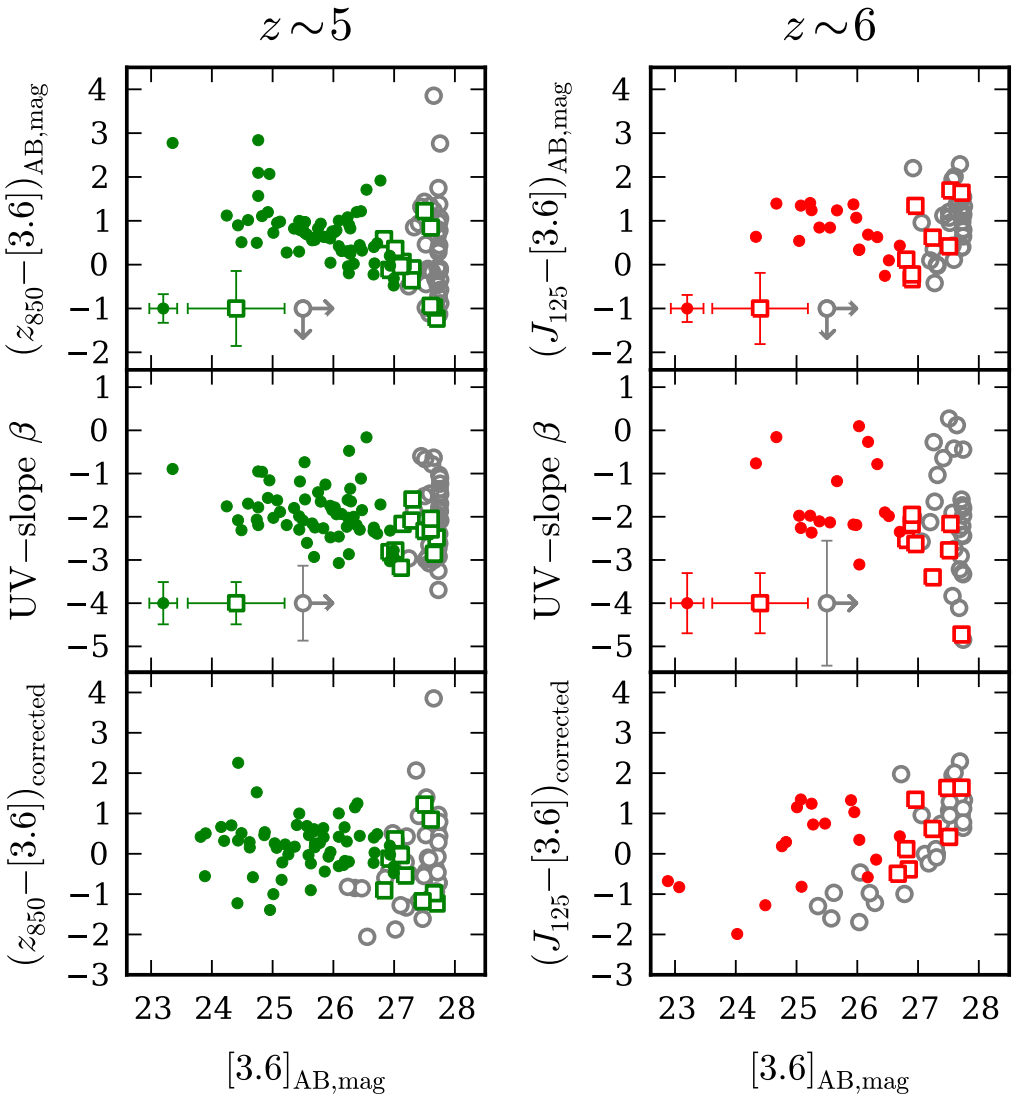

Figure 6.2: The observed colors of $z\sim5$ and 6 LBGs. *Left* column (green points) show the colors of the $V-$dropouts ($z\sim5$). *Right* column (red symbols) shows the colors of the $i-$dropouts ($z\sim6$). Symbols are as in Figure 6.1. The same trends of bluer colors (both the UV-slope and the UV-to-optical colors) for fainter sources are present at these redshifts.

.

universe at $z \sim 3.5$) of a CSF model in the absence of dust reddening. The dashed line on the top right corner shows our observational limits. The thick dashed line is a fit to the detected points only and shows a trend of redder UV-to-optical colors for brighter galaxies.

The middle panel of the figure shows the UV-slope characterized by β ($f_\lambda \propto \lambda^\beta$), as a function of [3.6] mag. A similar trend of redder colors for brighter sources is observed. The UV-slope beta was measured by fitting a power law to all the available*HST*/ACS and WFC3/IR photometric points for any given source.

Bouwens et al. (2011b) study the dependence of β with UV-luminosity and find a similar trend (see also, Finkelstein et al. 2011, McLure et al. 2011). As argued in that work, β can be affected by several factors, but it is most strongly dependent on the total dust content (which sets the normalization applied to the dust curve assumed). Assuming a Calzetti et al. (2000) extinction curve and a fiducial model with $\beta = -2.2$, it is possible to calibrate a relation between the reddening and the observed β (Meurer et al. 1999).

The bottom panel of Figure 6.1 shows the result of applying a dust reddening correction derived solely from the UV-slope (using the Meurer et al. 1999 relation) into the UV-to-optical color. The initial trend of redder color for brighter sources is weaker and most sources in the sample are in the color range that is covered by our dust-free CSF models. A remaining residual can be attributed to age variations such that sources that are brighter in the rest-frame optical are on average older. This is similar to the results shown in Labbé et al. (2007), who show that the UV and UV-to-optical color trends exhibited by star forming galaxies in the $z \sim 0.7 - 3.5$ range can largely be explained by the effects of dust reddening only, with a small contribution due to age. Figure 6.2 shows a very similar behavior at $z \sim 5$, and 6.

In view of this result, and to alleviate the difficulties produced by age-dust degeneracies, in the following modeling we establish the dust reddening normalization directly from the

observed UV slope β following the Meurer et al. (1999) relation:

$$A_{1600} = 4.43 + 1.99\beta \tag{6.1}$$

where A_{1600} is the attenuation in magnitudes at 1600 Å. The attenuations at other wavelengths are determined using a Calzetti et al. (2000) extinction curve. Sources with $\beta < -2.23$ are assigned $A_{1600} = 0$.

6.3.2 The Constant Star Formation model

We have used the FAST (Kriek et al. 2009) SED fitting code to fit the observed rest-frame UV + optical SEDs of the galaxies in our sample with a set of synthetic stellar population models (we use the Bruzual & Charlot 2003 models). In this section we present the results obtained when a smooth constant star formation (CSF) rate history is assumed. We have assumed a metallicity $Z = 0.2\,Z_{\odot}$ and a Salpeter (1955) IMF with cutoffs at 0.1 $M_{\odot}$ and 100 $M_{\odot}$. The set of models only include the stellar continuum fluxes and do not consider the effects of emission lines. These are explored in later sections.

Additionally, and as described in the previous section, we do not leave the reddening by dust as a free parameter but rather we have estimated it from the UV-slope β using Equation 6.1. This assumption alleviates the large uncertainties that arise from the dust–age degeneracy. For example, at $z \sim 4$, a model with zero dust reddening can produce SFRs that are lower by 1.8 dex, compared to a model with maximal dust reddening (minimal age). Meanwhile, the effect is much smaller for the determination of the stellar mass ($\lesssim 0.4$ dex).

The results of the SED fitting procedure are shown in Figure 6.3. The figure shows the SFR vs $M_{\rm star}$ for the $z \sim 4$ (top, blue), $z \sim 5$ (middle, green), and $z \sim 6$ (red) sources. The dashed lines show the minimum and maximum values of $M_{\rm star}$ at a given SFR that our models allow for. The distributions are very similar at all redshifts, suggesting little evolution of this relation, consistent with previous results that use similar assumptions (Stark et al. 2009,

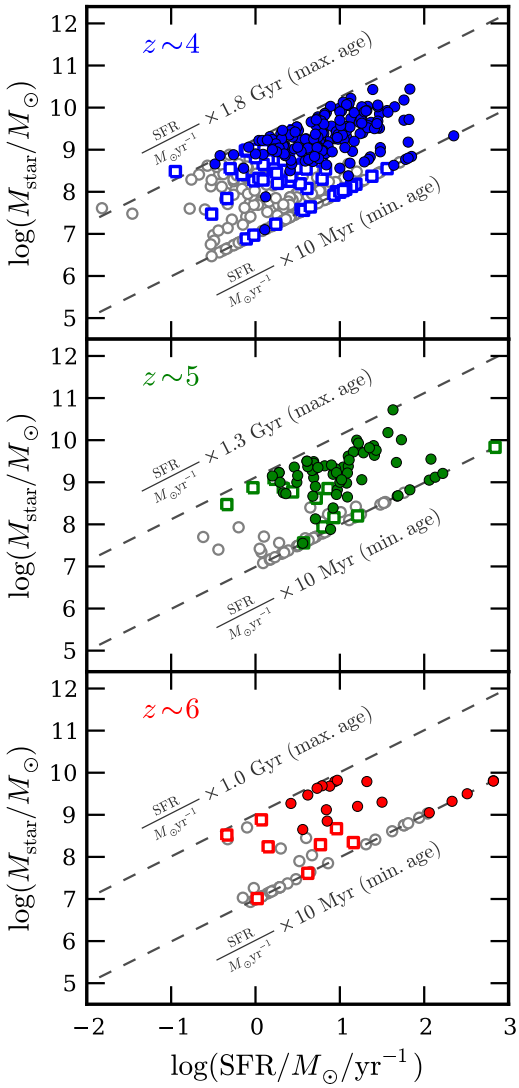

Figure 6.3: The SFR vs M_{star} relation for our samples at $z \sim 4$ (top, blue), $z \sim 5$ (middle, green), and $z \sim 6$ (botom, red). Only sources with reliable cleaned IRAC photometry are considered (see text Section 2.2). Stellar masses and SFRs were derived assuming a CSF history. The dust reddening in the model has been derived directly from the UV slopes β of each sources according to Equation 6.1. In all panels, solid circles indicate sources that are detected ($> 2\,sigma$) in the *Spitzer*/IRAC [3.6] channel and hence their masses can be more accurately estimated; open squares indicate marginal detections ($1 - 2\,sigma$); and open gray circles indicate IRAC undetected galaxies. The dashed lines indicate the minimum and maximum M_{star} that a galaxy can reach assuming that it has been forming stars at a constant rate, for the minimum age included in our models (10 Myr) and for the age of the universe at $z \sim 3.5, 4.5$, and 5.5 (from top to bottom).

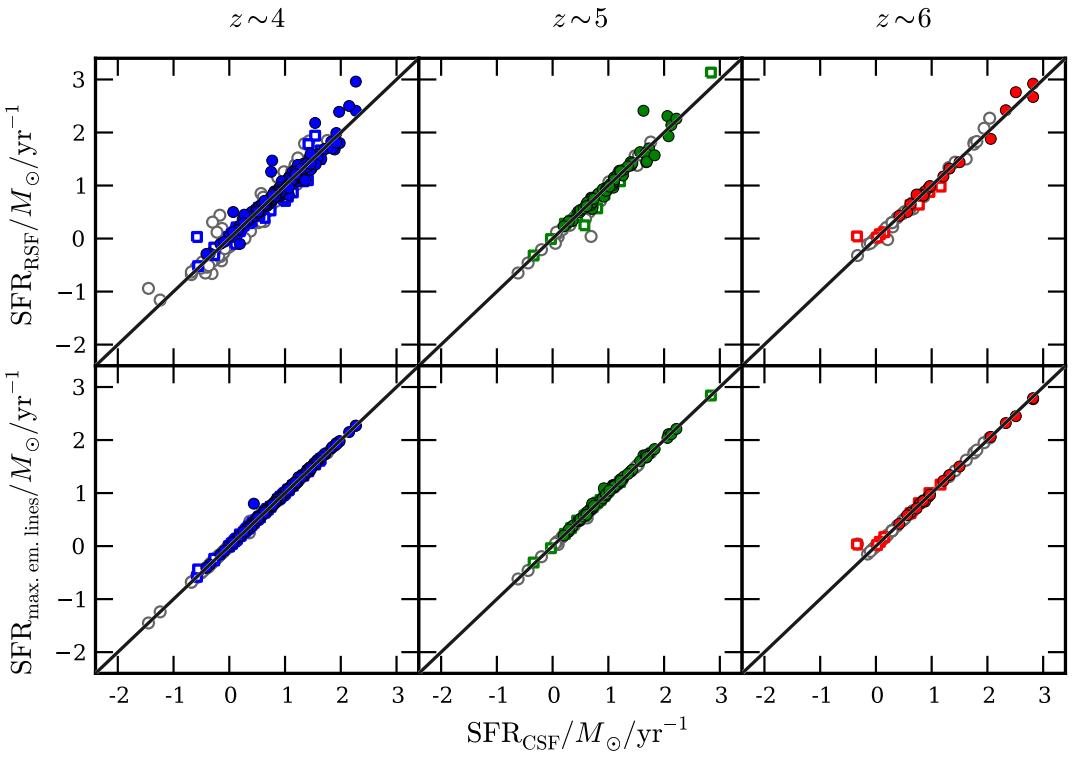

Figure 6.4: The SFR derived from different models. The top row shows the comparison between the rising star formation model based SFRs and the constant star formation models. The bottom row shows the effects of considering optical emission lines. For all the different models, the SFRs derived are very similar, with very little scatter.

González et al. 2010; 2011). It should be noted, however, that in previous works, the relation presented generally corresponds to SFRs that have not been corrected by dust extinction. Figure 6.3 shows the intrinsic SFRs, i.e., after corrections for dust reddening and dimming have been applied. The stellar masses have been derived from the same models used to derive the SFR. The fact that the relations still show little evolution is a consequence of the UV-to-optical colors being similar, implying similar properties of the galaxies as a function of redshift, including dust corrections.

A small fraction of the sample shows ages that are extremely young, crowding the 10 Myr dashed line. These sources are generally sources that are marginally detected or non-detected in the IRAC channels. The very blue UV-slopes of these sources dominate the fitting,

driving them to young ages. It is possible that they are indeed very young but this is hard to establish with the depths of the IRAC data used here. The analysis in this paper focuses on the more massive sources that are detected in *Spitzer*/IRAC, so this fraction of the population should not bias our main results.

In the following sections we study the effects of two important ingredients that have not been taken into account in the CSF models. We use the results from the CSF model as our base for comparison. The first consideration is the effect of assuming a SFH that better reproduces the evolution of the UV-LF at $z > 3$, i.e., an increasing SFH. The second, will explore the effects of emission lines (ignored in the previous analysis) on the derived physical parameters.

6.3.3 The Rising Star Formation Model

Under the assumption of a smooth star formation history, the UV-luminosity of galaxies is related to their SFR (e.g., the Madau relation; Madau et al. 1998; see also the SFR functions derived from the UV luminosity functions – Smit et al. 2012). The exact form of the relation does not change strongly between different smooth SFHs if the ages (time since onset of star formation) considered are older than ~ 100 Myr. Based on this relation, the previously presented model with a CSF history makes a clear prediction for the evolution of the UV-LF: it predicts a LF that does not change with redshift. This has been thoroughly ruled out using large samples of LBGs at $z > 4$ (e.g., Bouwens et al. 2007; 2011c, Oesch et al. 2010b).

The observed UV-LF evolves with cosmic time, showing a brighter characteristic magnitude at lower redshifts at least until $z \sim 3$. A model that better matches the observed evolution is one in which the average SFR of galaxies rises with time (Papovich et al. 2011), something that has also been predicted in several numerical simulations (e.g., Finlator et al. 2011, Jaacks et al. 2011).

By following sources at a constant cumulative number density $n(< M_{UV}) = 2 \times 10^{-4}\mathrm{Mpc}^{-3}$ as a function of redshift, Papovich et al. (2011) derive a best-fit exponentially

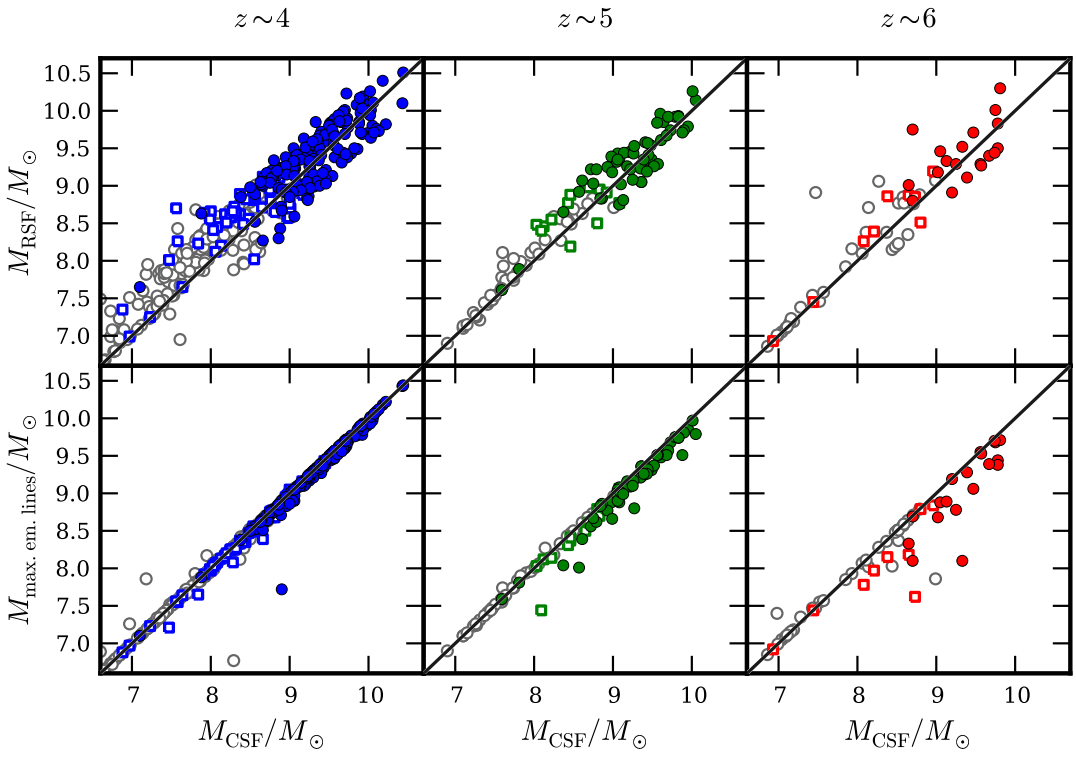

Figure 6.5: The stellar masses determined using our different model assumptions. The X-axis shows the stellar masses determined from the CSF model. The Y-axis in the top row shows the stellar masses derived from a model with exponentially rising star formation rate (SFR $\propto e^{(t-t_0)/\tau}$, where $t - t_0$ is the age, and $\tau = 500$ Myr). This model is tuned to reproduce the observed evolution of the UV-LF. Both $M_{\rm CSF}$ and $M_{\rm RSF}$ are derived from models with stellar continuum only. In all panels, the solid symbols represent sources that are detected ($> 2\sigma$) in IRAC [3.6], open squares show marginal detections ($1 - 2\sigma$), and open gray circles show IRAC undetected sources. The left column shows the $z \sim 4$ sample (blue), the middle is the $z \sim 5$ (green), and the right column shows the $z \sim 6$ sample. When only the detected sources are considered, the mean $\rm M_{CSF}$ and the $\rm M_{RSF}$ are consistent with each other, but with a scatter of ~ 0.25 dex. The IRAC undetected and marginal detections show a slightly larger mass for the RSF determinations. The Y-axis in the bottom row show the determinations of the stellar mass using a model that assumes strong optical emission lines which evolve with redshift (see Section 3.4). A CSF is assumed. The strength of the emission lines assumed can be seen in Figure 6.6. The effects on the stellar mass are larger at $z \sim 6$, where both IRAC channels present large contributions of flux from emission lines.

rising SFH of the form SFR $\propto \rm e^{(t-t_0)/\tau}$, with $\tau = 420$ Myr (they find a slightly better fit using a linear model but the differences are not large). A similar analysis at multiple values for the number density yields a similar result, with a best fit $\tau \sim 500$ Myr at all densities (Oesch et al. in preparation). The goal of the following analysis is to study the effects of such a model on the

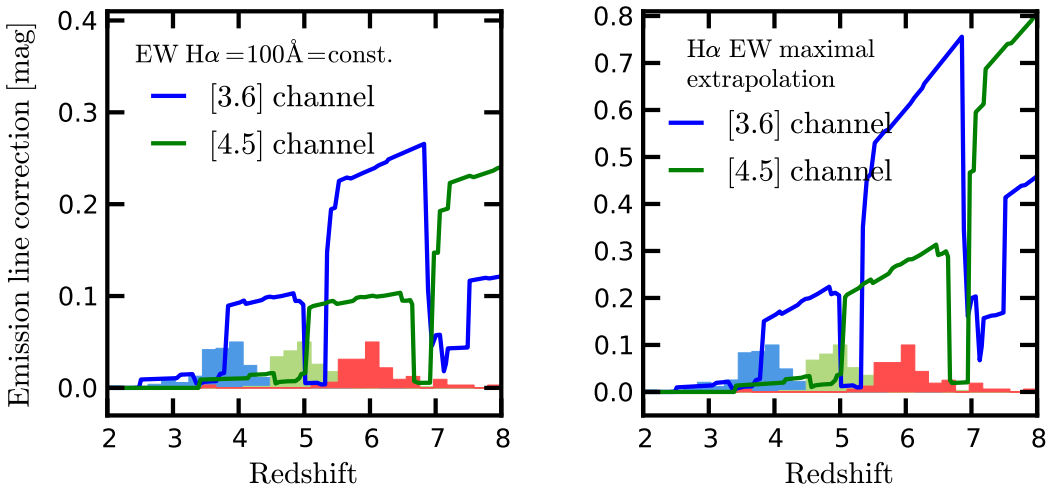

Figure 6.6: The possible effect of strong rest-frame optical emission lines on *Spitzer*/IRAC photometry. In both panels the blue curves show the corrections, in magnitudes, that need to be applied to the [3.6] photometry to remove the flux from emission lines. The green curve is the equivalent for the [4.5] photometry. In the *left* panel we conservatively assume a constant Hα rest-frame EW of 100 Å. To estimate the strength of the other lines we assume the flux ratios presented by Anders & Fritze-v. Alvensleben (2003), for a metallicity $Z = 0.2\,Z_{\odot}$. We also assume a flat underlying continuum (in F_{ν}). In the *right* panel the Hα EW is estimated from the trends observed as a function of redshift for sources with $\log(M_{star}) = 10 - 10.5$ (Fumagali et al., in prep.). This extrapolation is based on recent *HST* grism observations and predicts Hα $EW_0 \sim 300$ Å at $z \sim 6$. The light blue, light green, and light red, solid histograms (arbitrary normalization), show the redshift distribution of our sample. These corrections imply corrections to lower stellar masses but, in general, they do not affect the SFRs.

determination of the stellar masses and star formation rates. The details of the star formation history used are not important as long as they agree (or at least agree better than the CSF model) with the evolution of the UV-LF.

We have re-determined the SFRs and stellar masses for the galaxies in our sample using an exponentially rising star formation (RSF) model, as described before (SFR $\propto e^{(t-t_0)/\tau}$) , with $\tau = 500$ Myr. The parameter t_0 is free in our model. For the RSF and the CSF models, the SFR can be derived directly from the UV-luminosities (if the dust extinction is known – here we assume that it can be derived from the UV-slope). In fact, figure 6.4 shows that, as expected, the SFRs derived from the CSF and the RSF model are on average the same with little scatter. Since the final goal is to study the sSFR in our sample, we now focus on the effects

of the RSF model on the stellar masses, shown in Figure 6.5.

As can be seen in the top row, there is a significant scatter (~ 0.25 dex) in the comparison between the CSF and the RSF stellar masses. The mean value, however, does not change significantly when the IRAC detected sources are considered (solid circles). The IRAC undetected sources, meanwhile, show a slight bias towards larger RSF masses, but this could be attributed to the poor constraints in the rest-frame optical, which is very important to derive stellar masses. This is consistent with a recent report by Reddy et al. (2012), who also finds that the average $M_{\rm star}$ does not change between models with CSF and RSF for a sample of galaxies at $z \sim 3$. It is however, inconsistent with the reports of Papovich et al. (2011), who finds larger stellar masses when a RSF is assumed. In their analysis, however, the age is fixed with a formation redshift $z = 11$, artificially fixing the ages of the sources.

There is one important observation regarding the RSF models. A significant fraction of the sources that we have modeled result in ages that correspond to the maximal allowed in our set of models. This is a result of the fairly red UV-to-optical colors exhibited by these galaxies (even after dust reddening corrections). The models considered here only include stellar continuum light, and as a consequence, these red colors can only be interpreted as older ages. Two possible ways to alleviate this tension are: the presence of emission lines that would contribute to the flux measured with *Spitzer*/IRAC (Schaerer & de Barros 2010); or a non-smooth component to the SFH such that the SFH is rising on average but there is a characteristic duty cycle that makes the colors redder at any given age (see recent simulation results by, Jaacks et al. 2012). Since half of the sources that present maximal age at $z \sim 4$ are expected to be free of emission line contamination given their redshifts, the actual solution to the problem is probably a combination of both scenarios.

As has been shown, both the SFRs and the stellar masses obtained from the RSF models are on average the same as for the CSF models. In consequence, the average sSFR does not seem to be affected by this change in the modeling assumption. We turn now to the effect

of the possible contribution of emission lines to the rest-frame optical photometry. These lines are not expected to affect significantly the SFRs derived from SED fitting, but they can, in principle, have a strong effect on the values derived for the stellar masses.

6.3.4 The possible effect of optical emission lines.

It has been suggested (Schaerer & de Barros 2009; 2010) that a (possibly large) fraction of the flux detected with *Spitzer*/IRAC from galaxies at $z > 4.5$ could be coming from nebular regions associated with star formation in the form of emission lines. These emission lines, however, are currently inaccessible for spectroscopic confirmation for galaxies at $z > 4$ due to the very long wavelengths required for observation.

In a recent study, Shim et al. (2011) use a spectroscopic sample at $3.8 < z < 5.0$ to study the Hα EW from broad band photometry. In this redshift range, Hα falls in the IRAC [3.6] filter, contaminating that flux measurement. They find a median Hα EW of ~ 480 Å. This technique, however, is only sensitive to objects with large Hα EW (> 350 Å). This shows that there is a fraction of the population that shows strong emission lines, but it probably overestimates the average for the full population (see also Atek et al. 2011, an HST Grism study sensitive to the mos extreme line emitters).

Since the direct observation of emission lines at these redshifts is currently impossible, we need to make assumptions based on our understanding of these lines at lower redshift. At $z \sim 2 - 2.5$, for example, Erb et al. (2006b) find that the rest-frame EW of Hα for galaxies with $\log(M_{\rm star}/M_{\odot}) \sim 10.0 - 10.5$ is ~ 100 Å. The EW shows an increase with decreasing $M_{\rm star}$. Moreover, this EW also seems to increase with increasing redshift. In a study based on *HST* grism spectroscopy from the 3DHST survey (Brammer et al. 2012), Fumagalli et al. (in preparation) finds a best fit function:

$$\mathrm{EW}(z) \sim 15.76 \times (1+z)^{1.52} \text{Å}, \tag{6.2}$$

which is valid for sources with $\log(M_{star}) \sim 10.0 - 10.5$ in the $z \sim 0 - 2.5$ redshift range. Until future observations are made with JWST, it is unclear what is the typical strength of the optical emission lines at higher redshifts and lower masses. In the following, we estimate the effects that seem plausible based on these observations.

We take two different approaches. In a *conservative* approach, we will assume that the mean Hα EW observed in (Erb et al. 2006a) remains constant at 100 Å at all redshifts $z > 3$ and at all stellar masses. Given the trends of the EW described earlier with stellar mass and redshift, this is likely an underestimate of the strength exhibited by real galaxies at very high-z. A more extreme approach is to assume that the trends observed at $z \sim 0-2.5$ continue to higher redshifts following the same extrapolation (Equation 6.2). We call this the *maximal* emission line model. For each of the models (*conservative* and *maximal*) we derive the strength of all the other emission lines based on the flux ratios from Anders & Fritze-v. Alvensleben (2003) assuming a $Z = 0.2\,Z_{\odot}$ metallicity and a flat F_{ν} underlying optical continuum. Then we calculate the contribution of the emission lines to the broadband magnitudes assuming the redshifts derived from the CSF models in Section 3.2. Figure 6.6 shows the emission line contributions (in magnitudes) as a function of redshift. The solid histograms (arbitrary normalization) show the redshift distribution of our samples.

In a previous study (González et al. 2011), we studied the median SEDs of the present sample by stacking the photometry in bins of UV-luminosity. The SEDs at $z > 4$ showed a consistent excess in [3.6] flux over [4.5], which, as argued in that work, can be explained by the effect of emission lines. A simple model with Hα EW = constant = 300 Å, could simultaneously reproduce within the large uncertainties the observed UV-to-optical and [3.6]-[4.5] colors. This EW is very similar to the value predicted by the *maximal* model at $z \sim 6$.

Next, we subtract the emission line contribution from the photometry, and we re-fitted the SEDs with CSF models. As expected, the SFRs derived in this way are unchanged in both cases (Figure 6.4, bottom row). This is because the SFR of star forming galaxies (with ages

$\gtrsim 100\,\mathrm{Myr}$) depends almost exclusively on the UV fluxes, which are unaffected by the correction. The effects on the stellar masses can be seen in Figure 6.5 (bottom row). This figure only shows the effects for the *maximal* model, the effects from the *conservative* model are much smaller.

The effects of the emission lines consideration on the stellar mass are larger for the $z \sim 6$ sample. This is expected, since at this redshift there are strong emission lines affecting both the [3.6] (Hβ and OIII) and the [4.5] (Hα) channels. The average $\Delta \mathrm{M_{star}}$ for IRAC detected sources at this redshift is $\sim 0.2\,\mathrm{dex}$, with smaller masses when the emission lines are considered, and as a consequence, with larger sSFRs. The effects on the evolution of the sSFR, however, is not as straightforward to establish, since galaxies of the same stellar mass have to be considered as a function of redshift.

6.4 The sSFR at $z \gtrsim 2$

In the preceding sections we have studied the effects that different stellar population modeling assumptions have in the SFR and M_{star} determinations of high-z LBGs. We have shown that the SFRs do not change when a rising SFH is considered instead of a CSF. They are also unchanged when emission lines, which affect the rest-frame optical fluxes, are taking into consideration. For the simple smooth RSF that we consider, the average M_{star} derived for these galaxies does not change systematicaly with respect to the CSF model (although there is a scatter of $\sim 0.25\,\mathrm{dex}$ in the values determined). When the emission lines are considered, however, the stellar masses could be $\sim 0.2\,\mathrm{dex}$ smaller at $z \sim 6$.

Figure 6.7 shows the new values of sSFR determined from our sample as a function of redshift. The top panel shows the sSFR derived from a CSF for galaxies in two different M_{star} bins. The blue circles correspond to galaxies with $M_{\mathrm{star,CSF}} \sim 5 \times 10^9 M_\odot$ (the bins are $\Delta \log(M_{\mathrm{star}}) = 0.3$). The orange pentagons in the same panel show the sSFR for galaxies that are $\sim \times 5$ less massive. Although the uncertainties are large, there is evidence that the sSFR of

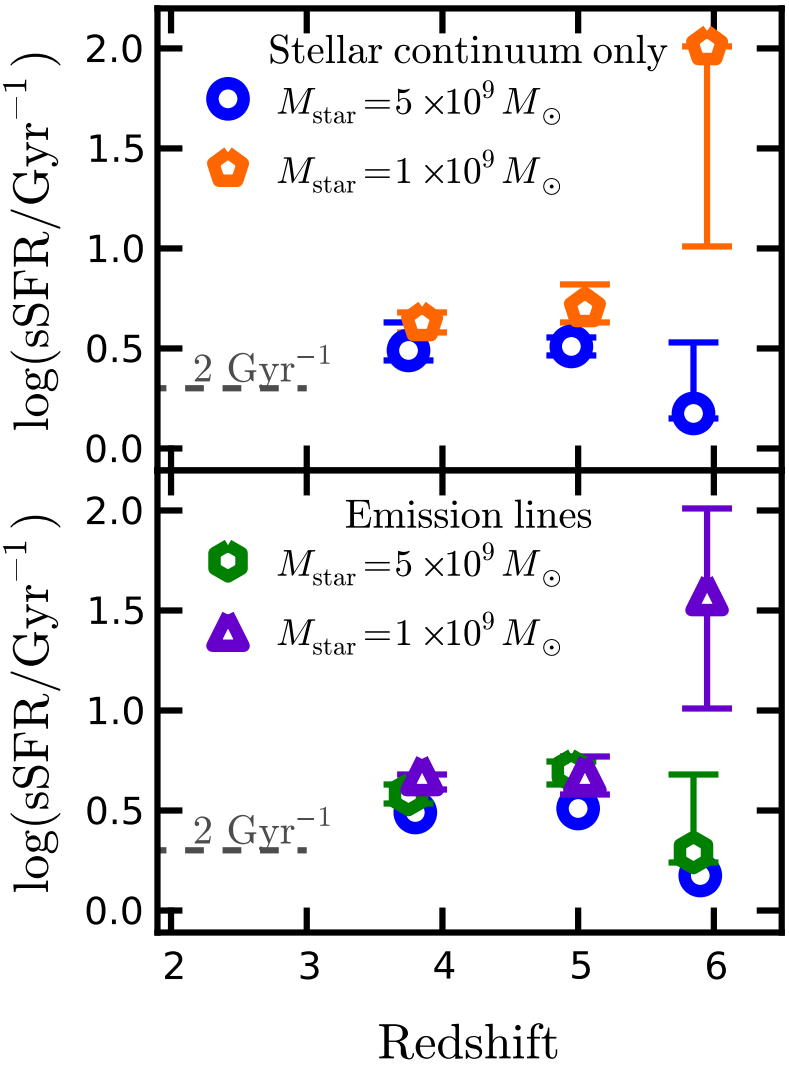

Figure 6.7: The specific SFR as a function of redshift for our samples at $z \sim 4, 5$, and 6. *Top:* The sSFR derived assuming the CSF history and models with stellar continuum only (i.e., ignoring the effects of emission lines). The sSFR was determined for galaxies in two different mass bins. Galaxies with lower mass have larger sSFR at all redshifts. Both mass bins show a fairly flat relation with redshift. Assuming a RSF does not change the results (see section 3.3). *Bottom:* Assuming our *maximal* model for the strength of the emission lines, we re-model the galaxies assuming a CSF history. A very similar behavior is observed to the one shown in the top panel. It should be noted that since the stellar masses have changed, the galaxies in the two bins in the top and bottom panels are not the same. The blue circles are the same as the ones in the top panel and are repeated here for reference only.

the less massive galaxies is larger by $\sim 0.1 - 0.2$ dex. For both mass bins, however, the sSFR shows little variation with redshift, consistent with previous reports (Stark et al. 2009, González et al. 2010, McLure et al. 2011). Since neither the average SFR nor $M_{\rm star}$ are changed when the RSF model is considered, the sSFRs will be the same as shown in this panel.

The bottom panel of Figure 6.7 shows the sSFR obtained when the emission lines are assumed to be as in the *maximal* model. In this case the hexagons (green) show the sSFR for galaxies with $M_{\rm star,em\ line} \sim 5 \times 10^9\, M_\odot$ and the triangles for galaxies with $M_{\rm star,em\ line} \sim 1 \times 10^9\, M_\odot$. The circles (light gray) are the same as the circles in the top panel and are repeated here only for reference.

It should be noted that the galaxies that go in each bin in the bottom panel are not the same compared to the top. In the top panel the $M_{\rm star}$ from CSF models with no emission lines is considered whereas in the bottom, the masses used correspond to the ones derived when the *maximal* model of emission lines is assumed. This is important because, if the same galaxies were considered, then their sSFRs should be larger when the emission lines are considered (because their masses are lower). Most importantly, this effect would be stronger at $z \sim 6$, suggesting a stronger evolution of the sSFR with redshift. This does not seem to be the case when galaxies within the same mass bin are compared.

The reason for the little variation between top and bottom panels may not seem obvious. If we want to study galaxies with $M_{\rm star,em\ line} \sim 5 \times 10^9\, M_\odot$ at $z \sim 6$, these galaxies would have had correspondingly larger masses in the CSF model with no emission lines. As shown in the top panel, galaxies with larger mass have lower sSFR in the CSF model. So we combine the effect of considering galaxies that originally had lower sSFR and now have lower masses (which implies higher sSFRs). As a result of the non-trivial combination, the sSFRs do not change significantly. The values obtained in both models are slightly larger but still close to $\sim 2\,{\rm Gyr}^{-1}$, similar to previous reports and consistent with the values reported at $z \sim 2 - 3$ (Daddi et al. 2007; 2009, Reddy et al. 2012). The possible evolution as a function of redshift is much slower

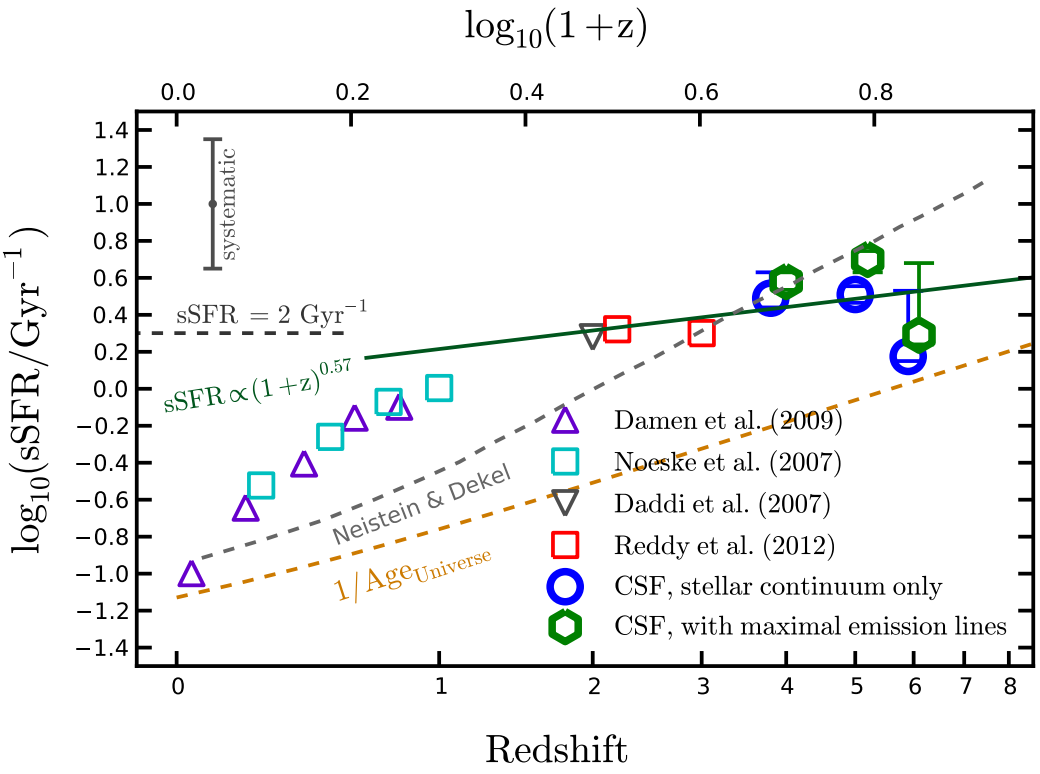

Figure 6.8: The specific star formation rate as a function of Redshift for galaxies with estimated stellar masses $\log(M_{star}/M_{\odot}) = 9.4 - 10$. The values at $z < 4$ are taken from the literature (Damen et al. 2009, Noeske et al. 2007, Daddi et al. 2007, Reddy et al. 2012). The values at $z > 4$ are derived in this work based on stellar population modeling of the full rest-frame UV and Optical SED. The dust reddening was fixed based on the Meurer et al. (1999) relation and the measured UV-slopes, β. Solid symbols correspond to results based on the CSF history model with no correction for emission lines. The open symbols show the results derived when emission lines flux is subtracted based on the model described in Section 3.4.

than observed at $z < 2$, with a best fit relation of the form sSFR $\propto (1+\mathrm{z})^{0.57}$. This relation was derived considering the $z \sim 2-3$ determinations from the literature and the $z \gtrsim 4$ values presented here (considering the models with emission lines, see Figure 6.8).

6.5 Discussion

Previous studies of the sSFR at high z had suggested that this quantity does not evolve strongly at $z \gtrsim 2$. This is very different to the behavior observed at lower redshifts and also to the theoretical models that consistently predict a sSFR that declines monotonically with redshfit when halos of a constant mass are studied. Most previous studies, however, determined SFRs and $M_{\rm star}$ using inconsistent assumptions for the dust reddening, used SFHs that are inconsistent with the evolution of the UV-LF, and did not take into account the effects of nebular emission lines in the stellar population modeling. This is not a complete list of the shortcomings of previous studies but represents the ones that are more amenable to be investigated, as we have done in the previous sections.

With the goal of studying the sSFR vs. z relation at $z \sim 4-6$, we have explored the effects of the different assumptions mentioned above on the SFRs and stellar masses derived from SED fitting of the observed SEDs. We find that the SFR is fairly robust to most assumptions, but there is a large uncertainty due to the age-dust degeneracy which cannot be resolved with current data. Since a simple recipe for the reddening based on the UV-slope β (Meurer et al. 1999) seems to be consistent with the trends of both the UV-to-optical color versus luminosity, as well as the UV-slope versus rest-frame optical luminosity, we have adopted it as our fiducial dust reddening.

We have explored a rising star formation history that better matches the observed evolution of the UV-LF as a function of redshift. The SFRs are not affected by the change from a CSF to a smoothly rising SFH. The SFRs do not change either when a model for the

emission line strength is included in the SED fitting. $M_{\rm star}$, on the other hand, decreases when the emission lines are assumed. This decrement is ~ 0.2 dex when we use a model based on the extrapolation of the lower-z emission line evolution. The change in $M_{\rm star}$varies with redshift, as different emission lines move in and out of the *Spitzer*/IRAC filters, but it is strongest at $z \sim 6$ when both IRAC channels are contaminated by the strongest emission lines: Hα, Hβ, and OIII.

Despite the change in the average stellar masses when the emission lines are considered, the sSFR *at a constant stellar mass* does not change strongly. With or without the consideration of emission lines, the sSFR shows only a weak evolution with at $z \gtrsim 2$ (Figures 6.7 and 6.8). A fit to the *maximal* emission line estimates of the sSFR, which includes the values at $z \sim 2-3$ reported in the literature (Daddi et al. 2007, Reddy et al. 2012), suggest the relation sSFR $\propto (1+\mathrm{z})^{0.57}$. The exponent of this relation is lower if the CSF model without emission lines is considered. Still, the weak evolution at $z \gtrsim 2$ is much weaker than expected from the lower-z trends and inconsistent with the predictions from numerical simulations (e.g., Neistein & Dekel 2008, Weinmann et al. 2011).

6.6 Summary

We have studied the physical properties of LBGs as derived from synthetic stellar population modeling of their rest-frame UV and optical SEDs. We have explored the effects of using a reddening law based on the UV colors only and the effects of assuming a smoothly rising SFH. In particular, we have studied the effects of these assumption in estimating the specific star formation rate of LBGs which has previously been reported to show little evolution at $z \sim 2-7$. The SFH explored here matches the evolution of the UV-LF and is in good agreement with the results from recent smooth particle hydrodynamics simulations. We have also studied the effects of emission lines on the SFR and stellar masses assuming two different models for the emission line strengths. Our main findings are the following:

- LBGs that are fainter in the rest-frame optical show bluer UV colors. This is consistent with the previously reported trends of bluer colors for fainter galaxies when the UV luminosity is taken as reference. The UV-to-optical colors are also bluer for fainter sources. This is expected if the reddening is caused by dust and also if it is caused by aging with a smooth SFH.

- Assuming that the UV slope reddening is caused by dust only as in Equation 6.1 (Meurer et al. 1999; and following a Calzetti et al. 2000, dust law), the corrected UV and UV-to-optical colors are fully within the range of dustless CSF models. A weak residual trend of bluer colors at fainter luminosities can be caused by the effects of aging of the population.

- We derive SFRs and stellar masses for our sample of LBGs using synthetic stellar population modeling. We have fixed the dust reddening normalization on the models assuming that all the reddening of the UV colors of an individual source is caused by dust, using the Meurer et al. (1999) relation.

- We find that the SFRs derived assuming a CSF history do not change when a smoothly rising SFH is used instead. The RSF that we use is chosen to matches the evolution of the UV-LF (SFR $\propto e^{(t-t_0)/\tau}$; $\tau = 500\,\mathrm{Myr}$). The stellar masses are also unchanged when the RSF is assumed, although there is a significant scatter of $\sim 0.25\,\mathrm{dex}$ in the $M_{\mathrm{star,CSF}} - M_{\mathrm{star,RSF}}$ relation.

- We explore the effects of emission lines assuming two different models for the strength of the lines as a function of redshift. The inclusion of emission lines only affects the stellar masses. For the *maximal* emission lines model, the stellar masses are up to 0.2 dex lower at $z \sim 6$ (and the sSFR larger).

- We estimate the sSFR for galaxies in two stellar mass bins at in our samples at $z \sim 4, 5,$ and 6. There is indication that the sSFR of lower mass sources are larger than those of

more massive systems. In particular, for the CSF model, $1 \times 10^9\,M_\odot$ galaxies with have sSFR that are $0.1 - 0.2$ dex larger than sources with $5 \times 10^9\,M_\odot$.

- At a constant $M_{\rm star}$, the sSFR derived from the CSF models shows little evolution with redshift. Considering emission lines affects the $M_{\rm star}$ and the sSFR of individual galaxies, but when galaxies at constant mass are considered, the sSFR still shows weak to no evolution with redshift. The sSFR at $z > 2$ shows a dependence sSFR $\propto (1 + {\rm z})^{0.57}$. This evolution is much slower than observed at $z < 2$ and is inconsistent with the expectations from simulations, which predict a monotonically decreasing sSFR with redshift.

Chapter 7

Summary and Concluding Remarks

The study of galaxies at $z \sim 4-8$ represents the current frontier in our understanding of how galaxies first formed and evolved to become the structures that we see in the local Universe. Observations have demonstrated that this is a period in which galaxy assembly proceeded at a very rapid pace. Studying the evolution of the properties of the galaxies that developed in this period, and their stellar mass assembly history provides crucial information about the process of early galaxy formation and evolution. Such information is elemental to understand the properties of current galaxies and the global history of structure assembly in the Universe.

Great progress has been made over the last few years in identifying galaxies in the first 1.5 Gyr after the Big Bang. The most important driver of this progress has been the *Hubble Space Telescope* (*HST*), in particular, thanks to the combination of ACS, NICMOS, and more recently WFC3/IR, from which we have now unprecedented large samples of candidates (thousands of candidates at $z \sim 4$ and even ~ 60 candidates at $z \sim 8$, Bouwens et al. 2011c).

One significant shortcoming of such observations, however, is that HST can only detect

the rest-frame UV light of galaxies at $z > 2.7$, providing very limited and uncertain information about the stellar masses of these sources. In this thesis we have extensively exploited the IR capabilities of the *Spitzer Space Telescope* to extend the wavelength coverage of $z > 4$ galaxies to the rest frame optical. This has allowed us to derive realistic estimates of the properties of the stellar populations of high-z galaxies, and in particular, of their stellar masses and the mass buildup at early times. The collection of works presented in this thesis represents the most comprehensive study of the properties of galaxies at $z \gtrsim 4 - 8$ to date.

The primary dataset used in this thesis are the *Spitzer*/IRAC observations in the GOODS fields (Giavalisco et al. 2004). These deep images are ideal for studying the very faint galaxies at $z > 4$. The size of the point spread function (PSF), however, generally results in crowded images, for which standard photometric techniques produce unreliable results. Throughout this thesis we have made use of a PSF modeling technique that takes advantage of the higher resolution information available from the HST images of the same fields. This technique has provided some of the most complete and reliable sample of galaxies with deep rest-frame optical measurements.

The extensive optical and mid-IR coverage of the $z > 4$ galaxies in our samples has allowed us to study the spectral energy distributions (SEDs) of high-z galaxies over a large luminosity and redshift range. We have also modeled the observed SED by fitting synthetic stellar population models to the observations. From these models we have learned about the properties of these galaxies (e.g., stellar masses, ages, dust reddening); in particular, we have derived extensive information about their stellar masses.

In Chapter 2 and Chapter 3 (González et al. 2010, Labbé et al. 2010b), we pushed the studies of stellar masses to the highest redshifts currently possible: $z \sim 7$ and 8. Remarkably, in Chapter 3 we present the first rest-frame optical detections of $z \sim 8$ galaxies, resulting in reliable measurement of the stellar masses of these sources and a first estimate of the stellar mass density of the Universe at this time. This estimate indicates a smooth increase by a factor

of $10\times$ in the stellar mass content of the Universe between $z \sim 8$ and $z \sim 4$, roughly consistent with expectations from the star formation rate density (SFRD) measurements based on studies of the UV LF.

The studies from Chapter 2 and 3 also show that the typical SEDs of galaxies at $z \sim 7-8$ appear to be remarkably similar to their $z \sim 4-6$ counterparts, exhibiting rest-frame $U-V$ colors $\sim 0.3-0.5$ mag. This results in a (not necessarily intuitive, but very useful) fairly tight correlation of the stellar masses with the UV luminosities of the sources that does not seem to change strongly with redshift (see also Stark et al. 2009).

We have used the relation found between stellar mass and UV luminosity to construct the first stellar mass functions at $z \sim 4-7$ in Chapter 4 (González et al. 2011). The stellar mass function (SMF) is a fundamental quantity that can provide valuable constraints on simulations. The faint end slope of this function, for example, can help rule out or favor certain mechanisms for supernova feedback that are included in simulations. It is very hard to construct a sample that is complete in mass, however, and so much of the work on the SMF at high z was very limited. The progress shown in Chapter 4 is only possible as a result of the existence of the stellar mass–UV luminosity relation. The median trend of this relation and the scatter at the bright end was studied carefully. At the very faint end of the population, we relied on stacking analysis to derive the mean masses. This was shown to be very important because the effects of variations on the mean trend can be directly translated into changes in the SMF, in particular the low-mass slope. This method for deriving the SMF has the added advantage that a completeness correction to very low masses can be derived. This has provided the first tentative estimates of the low-mass end of the SMF at high z. A first comparison to the predictions from a few hydrodynamical simulations of galaxy formation at high z, indicates that the low mass systems in these simulations may be over-predicted.

Even though the UV and optical SEDs of galaxies at $z \sim 4-7$ seemed very similar, the results from the stacking analysis in Chapter 4 suggested a slight variation in the mass-to-light

ratios (that is, stellar mass to UV light ratios). This change was in the sense that the fainter sources had lower mass-to-light ratios, indicating a slight systematic variation of the colors of the SEDs. Given this, it was important to study the median SEDs at high signal-to-noise. This was done in Chapter 5 (Gonzalez et al. 2011; submitted to ApJ) by studying the stacked SEDs at $z \sim 4-7$ over a wide luminosity range. This study confirmed that the median SEDs of galaxies are very similar across a wide redshift range $z \sim 4-7$ and over a span of luminosities. This probably indicates a typical mode of evolution that is close to self-similar (exponential growth), in agreement with the some numerical simulation results (Finlator et al. 2011, Jaacks et al. 2012) and with the SFHs derived from the evolution of the UV LF (Papovich et al. 2011). There are, however weak color trends with luminosity that are consistent with the previously reported variation in mass-to-light. These variations in the SED are also consistent with reports of evolution in the UV colors of these galaxies (e.g., Bouwens et al. 2011b, Wilkins et al. 2011, Finkelstein et al. 2011). This UV color variation and the UV-to-optical color variation found in this work seem both to be most easily explained by an increase in the dust content as a function of UV luminosity (more dust at higher UV luminosities or SFRs).

One very important outcome of Chapter 4 has to do with the rest-frame optical colors. The colors are the ones with the lowest signal-to-noise in the stacked SEDs, but they are found to be consistently blue at redshifts $z \gtrsim 5$. The blue $[3.6]-[4.5] \sim -0.3$ mag color exhibited by all the median stacked SEDs at $z \gtrsim 5$ is hard to justify with simple stellar-continuum-only stellar population models. The most likely explanation for this blue color is the presence of moderately strong emission lines in the rest-frame optical (which we had generally not included in our modeling). This has been proposed as a possible problem for our estimates of the stellar mass at $z \sim 6-7$ (Schaerer & de Barros 2009; 2010), suggesting that they could be biased high by assuming that all the light corresponds to stellar continuum.

Due to the low signal-to-noise in this color and the lack of more precise redshifts for the sources, it is not possible to use the result to place a robust constraint on the strength of

the emission lines (and hence on their effect on the masses). We show, however, that the color observed is consistent with a couple of recent results (Shim et al. 2011, Atek et al. 2011) that suggest emission line contributions to the IRAC bands that are significant but moderate, being close to 0.3 mag.

The issue of emission lines has become increasingly important to improve the determination of stellar masses of high-z galaxies. At $z > 5$, however, these lines are beyond the reach of current spectroscopic instrumentation. It seems that the actual strength of these lines will remain an unsolved issue until JWST is in orbit to take spectra of these galaxies in the IR, though new capabilities on ground-based 10 m-class telescopes may provide new insights. A direct spectroscopic census of optical lines at $z > 5$ will significantly improve the mass estimates at these redshifts.

It was interesting, however, that these data showed hints of the effect of emission lines. One of the most interesting effects of the emission lines could be on the specific SFR (sSFR) of galaxies.

We had showed for the first time in Chapter 2 (González et al. 2010), that the SEDs of galaxies with similar stellar mass seemed to have very similar sSFR in the period from $z \sim 2$ to $z \sim 7$. This apparent *plateau* in the sSFR vs. redshift relation is at odds with the expectations from theoretical simulations and prompted a series of theoretical works to explain the discrepancy. In most simulations, the gas and star formation follows closely the dark matter assembly, and the rate at which dark matter is accreted into halos declines monotonically with cosmic time approximately as $(1 + z)^{2.5}$. If the sSFR at constant mass is constant, then this indicates that at $z > 2$ the stellar mass assembly is mostly decoupled from the dark matter assembly in a way that is not accounted for in simulations.

The early result from Chapter 2 did not consider the possible effect of emission lines into the modeling. This was only one, though maybe the most important, among a series of simplifications that can now be modeled in some more detail to learn about the effects they

have in the sSFR. The main result in Chapter 6, is that when a simple model for the strength of emission lines as a function of redshift is considered, there is room in the observations for a sSFR that decreases monotonically with cosmic time. The rate of this decline as a function of redshift, however, is much slower than the decline in specific dark matter accretion rate and indicates that the simulations may still be missing an important piece in the behavior of the baryons. This is not necessarily surprising, however, as the effects of baryonic physics in the early galaxy assembly are poorly understood. For example, the behavior of very low metallicity gas at the highest redshifts, which has difficulty in cooling, could partly delay the star formation in these systems, effectively decoupling the rate of stellar mass assembly and the dark matter accretion (e.g., Krumholz & Dekel 2011).

The emission line strengths whose effects we have explored in this work are based on trends of the equivalent widths observed for Hα at low redshifts (Shapley et al. 2006; Fumagalli in preparation). Although these extrapolations are reasonable and consistent with the (not very stringent) observational constraints, it is important to notice that it is still highly speculative, as no direct observations of these lines at $z > 5$ are yet possible. In consequence, there is still the possibility that, when the correct evolution of the strength of emission lines as a function of redshift is finally elucidated, the sSFR may show a very different evolution to what we have presented here (although we consider it unlikely).

7.1 Future outlook

The progress in the understanding of the early buildup of stellar mass has been facilitated primarily by two remarkable instruments, the HST and the *Spitzer* space telescopes. While deep observations with HST have resulted in sizable samples of galaxies at $z \gtrsim 4$, a good fraction of these sources also have reasonably deep *Spitzer*/IRAC measurements that allow for stellar mass estimates. Despite the interesting progress obtained from such data, the shortcom-

ings of these samples are readily apparent. The outlook for progress in this field, however, is quite promising thanks to both the extended life of the current facilities and also to the next generation of instruments currently under planning and construction.

The limitations of the samples used in this work are most apparent at $z > 5$. The number of candidates known at such high redshift that also have deep IRAC coverage is significantly smaller than at $z \sim 4$. But even at $z \sim 4$, only 50% of the sources present significant detections ($> 2\,\sigma$) in the 23 h GOODS data, and are amenable to stellar mass studies. The new data currently being obtained by the CANDELS survey can help to significantly improve this situation. This survey will provide data similar to the used here but over an area $\sim 5\times$ larger. A good fraction of the much larger sample will also be accompanied by IRAC data of depth similar to that of the GOODS and will allow better precision in the study of the massive population at $z > 5$ (the star formation sequence at $z \sim 6 - 8$ for example). Even at the faint, less massive end of the population, stacking of large numbers of galaxies will improve our understanding of the masses and mass to light ratios of this important component of the overall population.

Deeper IRAC observations like the IUDF (150 hr integration in the deepest field, 3 fields total) will also allow us to push our studies to $2 - 5\times$ lower masses (depending on the redshift), and will allow more IRAC detections at $z \sim 8$. Since the *Spitzer* warm mission has recently been extended, it will also be possible to create more such fields to study the faint population. It is also possible to complement lensing surveys like the Cluster Lensing and Supernova Survey with Hubble (CLASH Postman et al. 2012) with deeper IRAC data to study the even fainter population.

Other progress in this field will have to wait somewhat longer but it promises to be worth the wait. The next generation of gigantic ground based telescopes (the Thirty Meter Telescope TMT, the European Extremely Large Telescope E-ELT, the Giant Magellan Telescope GMT) will be able to provide spectroscopic data with impressive efficiency. The current number of sources with spectroscopic identifications at $z > 4$ is very low (probably no more than

~ 200, and not all is yet public) and only available for the brightest sources. In fact the redshift distribution for sources found in $z \gtrsim 6$ LBG searches remain to be validated by spectroscopic surveys. This is obviously due to the extensive telescope investment that is required in today's facilities. The spectroscopic capabilities of the next generation giant telescopes will make extensive spectroscopic surveys feasible at $z \gtrsim 4$, and most importantly, this will be possible not only for the brightest end of the population.

Another line of progress that will probably have to wait less time comes from studies with the Atacama Large Millimeter Array (ALMA). Although not fully completed, this radio facility has already started operations. The enormous collecting area from its 66 antennas (when completed) and its sensitivity at very long wavelengths will allow very sensitive studies of the gas in galaxies at $z \gtrsim 5$. This will allow the first dynamical mass estimates at high redshift, which will provide invaluable constraints in the study of galaxy mass buildup. These observations may also help elucidate one of the most puzzling results of this thesis work: the very slow evolution of the sSFR as a function of redshift. If confirmed, this result indicates that the star forming efficiency of the gas that is infalling into halos decreases with higher redshift. As a consequence, it is predicted that the gas accumulates in galaxies over time until $z \sim 2$ (Krumholz & Dekel 2011). ALMA could obtain the first constraints on the gas reservoir of galaxies at very high redshift, providing invaluable information about the way in which stellar mass buildup proceeds from very early epochs.

Finally, one of the most exciting prospects by far, is the 2018 launch of the James Webb Space Telescope (JWST). This observatory, currently under construction, promises a complete revolution in the field of galaxy evolution. Operating far from earth and shielded from the sun at an orbit around the Lagrange point 2, JWST will be equipped with a 6.5 m mirror and it will be optimized for infrared studies. This makes this instrument particularly suitable for the study of very high redshift galaxies. It is expected that this instrument will provide the first look at the very first galaxies ever formed in the Universe at $z \gtrsim 10$. But even at more modest

redshifts, $z \sim 4 - 8$, the data collected by this telescope will be revolutionary. It will provide a much more complete coverage of the rest-frame optical wavelength range at these redshifts, and it will be much more sensitive, permitting a complete study of the population of galaxies to very low masses. Perhaps most interestingly, the multiobject spectroscopic capabilities of this telescope in the infrared will allow the first direct look at the rest-frame optical emission lines at $z \gtrsim 5$. As mentioned before in this chapter and discussed in Chapter 5 and 6, the contribution of emission lines to the IRAC fluxes measured for these galaxies is one very important source of uncertainty in stellar mass determination today. But the significance of such observations goes far beyond that. For example, the rest-frame optical spectra will allow for independent estimates of the star formation rate and specific star formation rate at high-z, and the first estimates of the metallicity of galaxies at $z \gtrsim 5$ and the mass-metallicity relation at high-z. This only scratches the surface of what is expected from JWST. The most interesting results, however, will be as is most often the case, those that we are not expecting.

The study of the stellar populations and the stellar mass buildup of galaxies during the first 1.5 Gyr has seen significant progress recently and this thesis has played a fundamental role in this progress. Perhaps most importantly, this work has pushed the limits of the studies of the most distant galaxies and showed the path for the future exploration of the early Universe. Future facilities, in particular the JWST space telescope will revolutionize the study of the rest-frame optical properties of high-z galaxies and will hopefully answer many of the questions that this work has left open.

Bibliography

Anders, P. & Fritze-v. Alvensleben, U. 2003, *A&A*, **401**, 1063

Atek, H., Siana, B., Scarlata, C., Malkan, M., McCarthy, P., Teplitz, H., Henry, A., Colbert, J., Bridge, C., Bunker, A. J., Dressler, A., Fosbury, R. A. E., Hathi, N. P., Martin, C., Ross, N. R., & Shim, H. 2011, *ApJ*, **743**, 121

Becker, R. H., Fan, X., White, R. L., Strauss, M. A., Narayanan, V. K., Lupton, R. H., Gunn, J. E., Annis, J., Bahcall, N. A., Brinkmann, J., Connolly, A. J., Csabai, I., Czarapata, P. C., Doi, M., Heckman, T. M., Hennessy, G. S., Ivezić, Ž., Knapp, G. R., Lamb, D. Q., McKay, T. A., Munn, J. A., Nash, T., Nichol, R., Pier, J. R., Richards, G. T., Schneider, D. P., Stoughton, C., Szalay, A. S., Thakar, A. R., & York, D. G. 2001, *AJ*, **122**, 2850

Beckwith, S. V. W., Stiavelli, M., Koekemoer, A. M., Caldwell, J. A. R., Ferguson, H. C., Hook, R., Lucas, R. A., Bergeron, L. E., Corbin, M., Jogee, S., Panagia, N., Robberto, M., Royle, P., Somerville, R. S., & Sosey, M. 2006, *AJ*, **132**, 1729

Bertin, E. & Arnouts, S. 1996, *A&AS*, **117**, 393

Bouwens, R. J., Illingworth, G. D., Blakeslee, J. P., Broadhurst, T. J., & Franx, M. 2004a, *ApJ*, **611**, L1

Bouwens, R. J., Illingworth, G. D., Blakeslee, J. P., & Franx, M. 2006, *ApJ*, **653**, 53

Bouwens, R. J., Illingworth, G. D., Franx, M., Chary, R., Meurer, G. R., Conselice, C. J., Ford, H., Giavalisco, M., & van Dokkum, P. 2009, *ApJ*, **705**, 936

Bouwens, R. J., Illingworth, G. D., Franx, M., & Ford, H. 2007, *ApJ*, **670**, 928

Bouwens, R. J., Illingworth, G. D., Franx, M., & Ford, H. 2008, *ApJ*, **686**, 230

Bouwens, R. J., Illingworth, G. D., González, V., Labbé, I., Franx, M., Conselice, C. J., Blakeslee, J., van Dokkum, P., Holden, B., Magee, D., Marchesini, D., & Zheng, W. 2010a, *ApJ*, **725**, 1587

Bouwens, R. J., Illingworth, G. D., Labbe, I., Oesch, P. A., Trenti, M., Carollo, C. M., van Dokkum, P. G., Franx, M., Stiavelli, M., González, V., Magee, D., & Bradley, L. 2011a, *Nature*, **469**, 504

Bouwens, R. J., Illingworth, G. D., Oesch, P. A., Franx, M., Labbe, I., Trenti, M., van Dokkum, P., Carollo, C. M., Gonzalez, V., & Magee, D. 2011b, *arXiv:1109.0994*

Bouwens, R. J., Illingworth, G. D., Oesch, P. A., Labbé, I., Trenti, M., van Dokkum, P., Franx, M., Stiavelli, M., Carollo, C. M., Magee, D., & Gonzalez, V. 2011c, *ApJ*, **737**, 90

Bouwens, R. J., Illingworth, G. D., Oesch, P. A., Stiavelli, M., van Dokkum, P., Trenti, M., Magee, D., Labbé, I., Franx, M., Carollo, C. M., & Gonzalez, V. 2010b, *ApJ*, **709**, L133

Bouwens, R. J., Illingworth, G. D., Oesch, P. A., Trenti, M., Stiavelli, M., Carollo, C. M., Franx, M., van Dokkum, P. G., Labbé, I., & Magee, D. 2010c, *ApJ*, **708**, L69

Bouwens, R. J., Thompson, R. I., Illingworth, G. D., Franx, M., van Dokkum, P. G., Fan, X., Dickinson, M. E., Eisenstein, D. J., & Rieke, M. J. 2004b, *ApJ*, **616**, L79

Bower, R. G., Benson, A. J., Malbon, R., Helly, J. C., Frenk, C. S., Baugh, C. M., Cole, S., & Lacey, C. G. 2006, *MNRAS*, **370**, 645

Bradley, L. D., Bouwens, R. J., Ford, H. C., Illingworth, G. D., Jee, M. J., Benítez, N., Broadhurst, T. J., Franx, M., Frye, B. L., Infante, L., Motta, V., Rosati, P., White, R. L., & Zheng, W. 2008, *ApJ*, **678**, 647

Brammer, G., van Dokkum, P., Franx, M., Fumagalli, M., Patel, S., Rix, H.-W., Skelton, R., Kriek, M., Nelson, E., Schmidt, K., Bezanson, R., da Cunha, E., Erb, D., Fan, X., Förster Schreiber, N., Illingworth, G., Labbé, I., Leja, J., Lundgren, B., Magee, D., Marchesini, D., McCarthy, P., Momcheva, I., Muzzin, A., Quadri, R., Steidel, C., Tal, T., Wake, D., Whitaker, K., & Williams, A. 2012, *ArXiv e-prints*

Brammer, G. B., van Dokkum, P. G., & Coppi, P. 2008, *ApJ*, **686**, 1503

Brinchmann, J. & Ellis, R. S. 2000, *ApJ*, **536**, L77

Brinchmann, J., Pettini, M., & Charlot, S. 2008, *MNRAS*, **385**, 769

Bruzual, G. & Charlot, S. 2003, *MNRAS*, **344**, 1000

Bunker, A. J., Stanway, E. R., Ellis, R. S., & McMahon, R. G. 2004, *MNRAS*, **355**, 374

Bunker, A. J., Wilkins, S., Ellis, R. S., Stark, D. P., Lorenzoni, S., Chiu, K., Lacy, M., Jarvis, M. J., & Hickey, S. 2010, *MNRAS*, **409**, 855

Calzetti, D., Armus, L., Bohlin, R. C., Kinney, A. L., Koornneef, J., & Storchi-Bergmann, T. 2000, *ApJ*, **533**, 682

Castellano, M., Fontana, A., Boutsia, K., Grazian, A., Pentericci, L., Bouwens, R., Dickinson, M., Giavalisco, M., Santini, P., Cristiani, S., Fiore, F., Gallozzi, S., Giallongo, E., Maiolino, R., Mannucci, F., Menci, N., Moorwood, A., Nonino, M., Paris, D., Renzini, A., Rosati, P., Salimbeni, S., Testa, V., & Vanzella, E. 2010a, *A&A*, **511**, A20

Castellano, M., Fontana, A., Paris, D., Grazian, A., Pentericci, L., Boutsia, K., Santini, P., Testa, V., Dickinson, M., Giavalisco, M., Bouwens, R., Cuby, J.-G., Mannucci, F., Clément,

B., Cristiani, S., Fiore, F., Gallozzi, S., Giallongo, E., Maiolino, R., Menci, N., Moorwood, A., Nonino, M., Renzini, A., Rosati, P., Salimbeni, S., & Vanzella, E. 2010b, *A&A*, **524**, A28

Choi, J. & Nagamine, K. 2010, *MNRAS*, pp 1042–+

Cowie, L. L. & Hu, E. M. 1998, *AJ*, **115**, 1319

Daddi, E., Dannerbauer, H., Stern, D., Dickinson, M., Morrison, G., Elbaz, D., Giavalisco, M., Mancini, C., Pope, A., & Spinrad, H. 2009, *ApJ*, **694**, 1517

Daddi, E., Dickinson, M., Morrison, G., Chary, R., Cimatti, A., Elbaz, D., Frayer, D., Renzini, A., Pope, A., Alexander, D. M., Bauer, F. E., Giavalisco, M., Huynh, M., Kurk, J., & Mignoli, M. 2007, *ApJ*, **670**, 156

Damen, M., Förster Schreiber, N. M., Franx, M., Labbé, I., Toft, S., van Dokkum, P. G., & Wuyts, S. 2009, *ApJ*, **705**, 617

Davé, R., Finlator, K., & Oppenheimer, B. D. 2006, *MNRAS*, **370**, 273

de Santis, C., Grazian, A., Fontana, A., & Santini, P. 2007, *New Astronomy*, **12**, 271

Dickinson, M. 1998, in M. Livio, S. M. Fall, & P. Madau (eds.), *The Hubble Deep Field*, p. 219

Dickinson, M. 1999, in S. Holt & E. Smith (eds.), *After the Dark Ages: When Galaxies were Young (the Universe at 2 < Z < 5)*, Vol. 470 of *American Institute of Physics Conference Series*, pp 122–132

Dunlop, J. S., McLure, R. J., Robertson, B. E., Ellis, R. S., Stark, D. P., Cirasuolo, M., & de Ravel, L. 2012, *MNRAS*, **420**, 901

Egami, E., Kneib, J.-P., Rieke, G. H., Ellis, R. S., Richard, J., Rigby, J., Papovich, C., Stark, D., Santos, M. R., Huang, J.-S., Dole, H., Le Floc'h, E., & Pérez-González, P. G. 2005, *ApJ*, **618**, L5

Ellis, R., Santos, M. R., Kneib, J.-P., & Kuijken, K. 2001, *ApJ*, **560**, L119

Erb, D. K., Shapley, A. E., Pettini, M., Steidel, C. C., Reddy, N. A., & Adelberger, K. L. 2006a, *ApJ*, **644**, 813

Erb, D. K., Steidel, C. C., Shapley, A. E., Pettini, M., Reddy, N. A., & Adelberger, K. L. 2006b, *ApJ*, **647**, 128

Erb, D. K., Steidel, C. C., Shapley, A. E., Pettini, M., Reddy, N. A., & Adelberger, K. L. 2006c, *ApJ*, **646**, 107

Eyles, L. P., Bunker, A. J., Ellis, R. S., Lacy, M., Stanway, E. R., Stark, D. P., & Chiu, K. 2007, *MNRAS*, **374**, 910

Eyles, L. P., Bunker, A. J., Stanway, E. R., Lacy, M., Ellis, R. S., & Doherty, M. 2005, *MNRAS*, **364**, 443

Fan, X., Strauss, M. A., Becker, R. H., White, R. L., Gunn, J. E., Knapp, G. R., Richards, G. T., Schneider, D. P., Brinkmann, J., & Fukugita, M. 2006, *AJ*, **132**, 117

Fazio, G. G., Hora, J. L., Allen, L. E., Ashby, M. L. N., Barmby, P., Deutsch, L. K., Huang, J.-S., Kleiner, S., Marengo, M., Megeath, S. T., Melnick, G. J., Pahre, M. A., Patten, B. M., Polizotti, J., Smith, H. A., Taylor, R. S., Wang, Z., Willner, S. P., Hoffmann, W. F., Pipher, J. L., Forrest, W. J., McMurty, C. W., McCreight, C. R., McKelvey, M. E., McMurray, R. E., Koch, D. G., Moseley, S. H., Arendt, R. G., Mentzell, J. E., Marx, C. T., Losch, P., Mayman, P., Eichhorn, W., Krebs, D., Jhabvala, M., Gezari, D. Y., Fixsen, D. J., Flores, J., Shakoorzadeh, K., Jungo, R., Hakun, C., Workman, L., Karpati, G., Kichak, R., Whitley, R., Mann, S., Tollestrup, E. V., Eisenhardt, P., Stern, D., Gorjian, V., Bhattacharya, B., Carey, S., Nelson, B. O., Glaccum, W. J., Lacy, M., Lowrance, P. J., Laine, S., Reach, W. T., Stauffer, J. A., Surace, J. A., Wilson, G., Wright, E. L., Hoffman, A., Domingo, G., & Cohen, M. 2004, *ApJS*, **154**, 10

Ferguson, H. C., Dickinson, M., Giavalisco, M., Kretchmer, C., Ravindranath, S., Idzi, R., Taylor, E., Conselice, C. J., Fall, S. M., Gardner, J. P., Livio, M., Madau, P., Moustakas, L. A., Papovich, C. M., Somerville, R. S., Spinrad, H., & Stern, D. 2004, *ApJ*, **600**, L107

Finkelstein, S. L., Papovich, C., Giavalisco, M., Reddy, N. A., Ferguson, H. C., Koekemoer, A. M., & Dickinson, M. 2010, *ApJ*, **719**, 1250

Finkelstein, S. L., Papovich, C., Salmon, B., Finlator, K., Dickinson, M., Ferguson, H. C., Giavalisco, M., Koekemoer, A. M., Reddy, N. A., Bassett, R., Conselice, C. J., Dunlop, J. S., Faber, S. M., Grogin, N. A., Hathi, N. P., Kocevski, D. D., Lai, K., Lee, K.-S., McLure, R. J., Mobasher, B., & Newman, J. A. 2011, *arXiv:1110.3785*

Finlator, K., Davé, R., & Oppenheimer, B. D. 2007, *MNRAS*, **376**, 1861

Finlator, K., Oppenheimer, B. D., & Davé, R. 2011, *MNRAS*, **410**, 1703

Fioc, M. & Rocca-Volmerange, B. 1997, *A&A*, **326**, 950

Giavalisco, M., Ferguson, H. C., Koekemoer, A. M., Dickinson, M., Alexander, D. M., Bauer, F. E., Bergeron, J., Biagetti, C., Brandt, W. N., Casertano, S., Cesarsky, C., Chatzichristou, E., Conselice, C., Cristiani, S., Da Costa, L., Dahlen, T., de Mello, D., Eisenhardt, P., Erben, T., Fall, S. M., Fassnacht, C., Fosbury, R., Fruchter, A., Gardner, J. P., Grogin, N., Hook, R. N., Hornschemeier, A. E., Idzi, R., Jogee, S., Kretchmer, C., Laidler, V., Lee, K. S., Livio, M., Lucas, R., Madau, P., Mobasher, B., Moustakas, L. A., Nonino, M., Padovani, P., Papovich, C., Park, Y., Ravindranath, S., Renzini, A., Richardson, M., Riess, A., Rosati, P., Schirmer, M., Schreier, E., Somerville, R. S., Spinrad, H., Stern, D., Stiavelli, M., Strolger, L., Urry, C. M., Vandame, B., Williams, R., & Wolf, C. 2004, *ApJ*, **600**, L93

Gonzalez, V., Bouwens, R., Labbe, I., Illingworth, G., Oesch, P., Franx, M., & Magee, D. 2011, *arXiv:1110.6441*

González, V., Labbé, I., Bouwens, R. J., Illingworth, G., Franx, M., & Kriek, M. 2011, *ApJ*, **735**, L34+

González, V., Labbé, I., Bouwens, R. J., Illingworth, G., Franx, M., Kriek, M., & Brammer, G. B. 2010, *ApJ*, **713**, 115

Hickey, S., Bunker, A., Jarvis, M. J., Chiu, K., & Bonfield, D. 2010, *MNRAS*, **404**, 212

Jaacks, J., Choi, J., & Nagamine, K. 2011, *arXiv:1104.2345*

Jaacks, J., Nagamine, K., & Choi, J.-H. 2012, *arXiv:1204.4846*

Kajisawa, M., Konishi, M., Suzuki, R., Tokoku, C., Uchimoto, Y., Katsuno, Yoshikawa, T., Akiyama, M., Ichikawa, T., Ouchi, M., Omata, K., Tanaka, I., Nishimura, T., & Yamada, T. 2006, *PASJ*, **58**, 951

Khochfar, S. & Silk, J. 2011, *MNRAS*, **410**, L42

Komatsu, E., Dunkley, J., Nolta, M. R., Bennett, C. L., Gold, B., Hinshaw, G., Jarosik, N., Larson, D., Limon, M., Page, L., Spergel, D. N., Halpern, M., Hill, R. S., Kogut, A., Meyer, S. S., Tucker, G. S., Weiland, J. L., Wollack, E., & Wright, E. L. 2009, *ApJS*, **180**, 330

Kriek, M., van Dokkum, P. G., Labbé, I., Franx, M., Illingworth, G. D., Marchesini, D., & Quadri, R. F. 2009, *ApJ*, **700**, 221

Kroupa, P. 2001, *MNRAS*, **322**, 231

Krumholz, M. R. & Dekel, A. 2011, *arXiv:1106.0301*

Labbé, I., Bouwens, R., Illingworth, G. D., & Franx, M. 2006, *ApJ*, **649**, L67

Labbé, I., Franx, M., Rudnick, G., Schreiber, N. M. F., Rix, H.-W., Moorwood, A., van Dokkum, P. G., van der Werf, P., Röttgering, H., van Starkenburg, L., van der Wel, A., Kuijken, K., & Daddi, E. 2003, *AJ*, **125**, 1107

Labbé, I., Franx, M., Rudnick, G., Schreiber, N. M. F., van Dokkum, P. G., Moorwood, A., Rix, H.-W., Röttgering, H., Trujillo, I., & van der Werf, P. 2007, *ApJ*, **665**, 944

Labbé, I., González, V., Bouwens, R. J., Illingworth, G. D., Franx, M., Trenti, M., Oesch, P. A., van Dokkum, P. G., Stiavelli, M., Carollo, C. M., Kriek, M., & Magee, D. 2010a, *ApJ*, **716**, L103

Labbé, I., González, V., Bouwens, R. J., Illingworth, G. D., Oesch, P. A., van Dokkum, P. G., Carollo, C. M., Franx, M., Stiavelli, M., Trenti, M., Magee, D., & Kriek, M. 2010b, *ApJ*, **708**, L26

Laporte, N., Pelló, R., Schaerer, D., Richard, J., Egami, E., Kneib, J. P., Le Borgne, J. F., Maizy, A., Boone, F., Hudelot, P., & Mellier, Y. 2011, *A&A*, **531**, A74+

Lee, K.-S. 2007, *Ph.D. thesis*, The Johns Hopkins University

Lee, K.-S., Dey, A., Reddy, N., Brown, M. J. I., Gonzalez, A. H., Jannuzi, B. T., Cooper, M. C., Fan, X., Bian, F., Glikman, E., Stern, D., Brodwin, M., & Cooray, A. 2011a, *ApJ*, **733**, 99

Lee, K.-S., Ferguson, H. C., Wiklind, T., Dahlen, T., Dickinson, M. E., Giavalisco, M., Grogin, N., Papovich, C., Messias, H., Guo, Y., & Lin, L. 2011b, *arXiv:1111.1233*

Lee, K.-S., Giavalisco, M., Gnedin, O. Y., Somerville, R. S., Ferguson, H. C., Dickinson, M., & Ouchi, M. 2006, *ApJ*, **642**, 63

Lehnert, M. D. & Bremer, M. 2003, *ApJ*, **593**, 630

Madau, P., Haardt, F., & Rees, M. J. 1999, *ApJ*, **514**, 648

Madau, P., Pozzetti, L., & Dickinson, M. 1998, *ApJ*, **498**, 106

Maiolino, R., Nagao, T., Grazian, A., Cocchia, F., Marconi, A., Mannucci, F., Cimatti, A., Pipino, A., Ballero, S., Calura, F., Chiappini, C., Fontana, A., Granato, G. L., Matteucci, F., Pastorini, G., Pentericci, L., Risaliti, G., Salvati, M., & Silva, L. 2008, *A&A*, **488**, 463

Maraston, C. 2005, *MNRAS*, **362**, 799

Marchesini, D., van Dokkum, P. G., Förster Schreiber, N. M., Franx, M., Labbé, I., & Wuyts, S. 2009, *ApJ*, **701**, 1765

McLure, R. J., Cirasuolo, M., Dunlop, J. S., Foucaud, S., & Almaini, O. 2009, *MNRAS*, **395**, 2196

McLure, R. J., Dunlop, J. S., Cirasuolo, M., Koekemoer, A. M., Sabbi, E., Stark, D. P., Targett, T. A., & Ellis, R. S. 2010, *MNRAS*, **403**, 960

McLure, R. J., Dunlop, J. S., de Ravel, L., Cirasuolo, M., Ellis, R. S., Schenker, M., Robertson, B. E., Koekemoer, A. M., Stark, D. P., & Bowler, R. A. A. 2011, *MNRAS*, **418**, 2074

Meurer, G. R., Heckman, T. M., & Calzetti, D. 1999, *ApJ*, **521**, 64

Michałowski, M. J., Watson, D., & Hjorth, J. 2010, *ApJ*, **712**, 942

Mobasher, B., Dickinson, M., Ferguson, H. C., Giavalisco, M., Wiklind, T., Stark, D., Ellis, R. S., Fall, S. M., Grogin, N. A., Moustakas, L. A., Panagia, N., Sosey, M., Stiavelli, M., Bergeron, E., Casertano, S., Ingraham, P., Koekemoer, A., Labbé, I., Livio, M., Rodgers, B., Scarlata, C., Vernet, J., Renzini, A., Rosati, P., Kuntschner, H., Kümmel, M., Walsh, J. R., Chary, R., Eisenhardt, P., Pirzkal, N., & Stern, D. 2005, *ApJ*, **635**, 832

Neistein, E. & Dekel, A. 2008, *MNRAS*, **383**, 615

Noeske, K. G., Weiner, B. J., Faber, S. M., Papovich, C., Koo, D. C., Somerville, R. S., Bundy, K., Conselice, C. J., Newman, J. A., Schiminovich, D., Le Floc'h, E., Coil, A. L., Rieke, G. H., Lotz, J. M., Primack, J. R., Barmby, P., Cooper, M. C., Davis, M., Ellis, R. S., Fazio, G. G., Guhathakurta, P., Huang, J., Kassin, S. A., Martin, D. C., Phillips, A. C., Rich, R. M., Small, T. A., Willmer, C. N. A., & Wilson, G. 2007, *ApJ*, **660**, L43

Oesch, P. A., Bouwens, R. J., Carollo, C. M., Illingworth, G. D., Magee, D., Trenti, M., Stiavelli, M., Franx, M., Labbé, I., & van Dokkum, P. G. 2010a, *ApJ*, **725**, L150

Oesch, P. A., Bouwens, R. J., Illingworth, G. D., Carollo, C. M., Franx, M., Labbé, I., Magee, D., Stiavelli, M., Trenti, M., & van Dokkum, P. G. 2010b, *ApJ*, **709**, L16

Oesch, P. A., Bouwens, R. J., Illingworth, G. D., Labbé, I., Trenti, M., Gonzalez, V., Carollo, C. M., Franx, M., van Dokkum, P. G., & Magee, D. 2012, *ApJ*, **745**, 110

Oesch, P. A., Carollo, C. M., Stiavelli, M., Trenti, M., Bergeron, L. E., Koekemoer, A. M., Lucas, R. A., Pavlovsky, C. M., Beckwith, S. V. W., Dahlen, T., Ferguson, H. C., Gardner, J. P., Lilly, S. J., Mobasher, B., & Panagia, N. 2009, *ApJ*, **690**, 1350

Oke, J. B. & Gunn, J. E. 1983, *ApJ*, **266**, 713

Ouchi, M., Mobasher, B., Shimasaku, K., Ferguson, H. C., Fall, S. M., Ono, Y., Kashikawa, N., Morokuma, T., Nakajima, K., Okamura, S., Dickinson, M., Giavalisco, M., & Ohta, K. 2009, *ApJ*, **706**, 1136

Ouchi, M., Tokoku, C., Shimasaku, K., & Ichikawa, T. 2007, in N. Metcalfe & T. Shanks (eds.), *Cosmic Frontiers*, Vol. 379 of *Astronomical Society of the Pacific Conference Series*, p. 47

Papovich, C., Dickinson, M., & Ferguson, H. C. 2001, *ApJ*, **559**, 620

Papovich, C., Finkelstein, S. L., Ferguson, H. C., Lotz, J. M., & Giavalisco, M. 2011, *MNRAS*, **412**, 1123

Pawlik, A. H., Schaye, J., & van Scherpenzeel, E. 2009, *MNRAS*, **394**, 1812

Peng, E. W., Ford, H. C., Freeman, K. C., & White, R. L. 2002, *AJ*, **124**, 3144

Pettini, M., Steidel, C. C., Adelberger, K. L., Dickinson, M., & Giavalisco, M. 2000, *ApJ*, **528**, 96

Postman, M., Coe, D., Benítez, N., Bradley, L., Broadhurst, T., Donahue, M., Ford, H., Graur, O., Graves, G., Jouvel, S., Koekemoer, A., Lemze, D., Medezinski, E., Molino, A., Moustakas, L., Ogaz, S., Riess, A., Rodney, S., Rosati, P., Umetsu, K., Zheng, W., Zitrin, A., Bartelmann, M., Bouwens, R., Czakon, N., Golwala, S., Host, O., Infante, L., Jha, S., Jimenez-Teja, Y., Kelson, D., Lahav, O., Lazkoz, R., Maoz, D., McCully, C., Melchior, P., Meneghetti, M., Merten, J., Moustakas, J., Nonino, M., Patel, B., Regös, E., Sayers, J., Seitz, S., & Van der Wel, A. 2012, *ApJS*, **199**, 25

Reddy, N. A., Pettini, M., Steidel, C. C., Shapley, A. E., Erb, D. K., & Law, D. R. 2012, *arXiv:1205.0555*

Reddy, N. A. & Steidel, C. C. 2009, *ApJ*, **692**, 778

Reddy, N. A., Steidel, C. C., Fadda, D., Yan, L., Pettini, M., Shapley, A. E., Erb, D. K., & Adelberger, K. L. 2006, *ApJ*, **644**, 792

Richard, J., Kneib, J.-P., Ebeling, H., Stark, D. P., Egami, E., & Fiedler, A. K. 2011, *MNRAS*, **414**, L31

Richard, J., Stark, D. P., Ellis, R. S., George, M. R., Egami, E., Kneib, J.-P., & Smith, G. P. 2008, *ApJ*, **685**, 705

Rudnick, G., Rix, H.-W., Franx, M., Labbé, I., Blanton, M., Daddi, E., Förster Schreiber, N. M., Moorwood, A., Röttgering, H., Trujillo, I., van der Wel, A., van der Werf, P., van Dokkum, P. G., & van Starkenburg, L. 2003, *ApJ*, **599**, 847

Salpeter, E. E. 1955, *ApJ*, **121**, 161

Sawicki, M., Iwata, I., Ohta, K., Thompson, D., Tamura, N., Akiyama, M., Aoki, K., Ando, M., & Kiuchi, G. 2007, in J. Afonso, H. C. Ferguson, B. Mobasher, & R. Norris (eds.), *Deepest Astronomical Surveys*, Vol. 380 of *Astronomical Society of the Pacific Conference Series*, p. 433

Sawicki, M. & Yee, H. K. C. 1998, *AJ*, **115**, 1329

Schaerer, D. 2002, *A&A*, **382**, 28

Schaerer, D. & de Barros, S. 2009, *A&A*, **502**, 423

Schaerer, D. & de Barros, S. 2010, *A&A*, **515**, A73+

Schiminovich, D., Ilbert, O., Arnouts, S., Milliard, B., Tresse, L., Le Fèvre, O., Treyer, M., Wyder, T. K., Budavári, T., Zucca, E., Zamorani, G., Martin, D. C., Adami, C., Arnaboldi, M., Bardelli, S., Barlow, T., Bianchi, L., Bolzonella, M., Bottini, D., Byun, Y.-I., Cappi, A., Contini, T., Charlot, S., Donas, J., Forster, K., Foucaud, S., Franzetti, P., Friedman, P. G., Garilli, B., Gavignaud, I., Guzzo, L., Heckman, T. M., Hoopes, C., Iovino, A., Jelinsky, P., Le Brun, V., Lee, Y.-W., Maccagni, D., Madore, B. F., Malina, R., Marano, B., Marinoni, C., McCracken, H. J., Mazure, A., Meneux, B., Morrissey, P., Neff, S., Paltani, S., Pellò, R., Picat, J. P., Pollo, A., Pozzetti, L., Radovich, M., Rich, R. M., Scaramella, R., Scodeggio, M., Seibert, M., Siegmund, O., Small, T., Szalay, A. S., Vettolani, G., Welsh, B., Xu, C. K., & Zanichelli, A. 2005, *ApJ*, **619**, L47

Shapley, A. E., Steidel, C. C., Pettini, M., Adelberger, K. L., & Erb, D. K. 2006, *ApJ*, **651**, 688

Shim, H., Chary, R.-R., Dickinson, M., Lin, L., Spinrad, H., Stern, D., & Yan, C.-H. 2011, *ApJ*, **738**, 69

Smit, R., Bouwens, R. J., Franx, M., Illingworth, G. D., Labbé, I., Oesch, P. A., & van Dokkum, P. G. 2012, *arXiv:1204.3626*

Stanway, E. R., Bunker, A. J., & McMahon, R. G. 2003, *MNRAS*, **342**, 439

Stanway, E. R., McMahon, R. G., & Bunker, A. J. 2005, *MNRAS*, **359**, 1184

Stark, D. P., Bunker, A. J., Ellis, R. S., Eyles, L. P., & Lacy, M. 2007a, *ApJ*, **659**, 84

Stark, D. P., Ellis, R. S., Bunker, A., Bundy, K., Targett, T., Benson, A., & Lacy, M. 2009, *ApJ*, **697**, 1493

Stark, D. P., Ellis, R. S., Richard, J., Kneib, J.-P., Smith, G. P., & Santos, M. R. 2007b, *ApJ*, **663**, 10

Steidel, C. C., Adelberger, K. L., Shapley, A. E., Pettini, M., Dickinson, M., & Giavalisco, M. 2000, *ApJ*, **532**, 170

Steidel, C. C., Giavalisco, M., Pettini, M., Dickinson, M., & Adelberger, K. L. 1996, *ApJ*, **462**, L17

Taylor, E. N., Franx, M., van Dokkum, P. G., Quadri, R. F., Gawiser, E., Bell, E. F., Barrientos, L. F., Blanc, G. A., Castander, F. J., Damen, M., Gonzalez-Perez, V., Hall, P. B., Herrera, D., Hildebrandt, H., Kriek, M., Labbé, I., Lira, P., Maza, J., Rudnick, G., Treister, E., Urry, C. M., Willis, J. P., & Wuyts, S. 2009, *ApJS*, **183**, 295

Thompson, R. I., Illingworth, G., Bouwens, R., Dickinson, M., Eisenstein, D., Fan, X., Franx, M., Riess, A., Rieke, M. J., Schneider, G., Stobie, E., Toft, S., & van Dokkum, P. 2005, *AJ*, **130**, 1

Thompson, R. I., Storrie-Lombardi, L. J., Weymann, R. J., Rieke, M. J., Schneider, G., Stobie, E., & Lytle, D. 1999, *AJ*, **117**, 17

Weinmann, S. M., Neistein, E., & Dekel, A. 2011, *MNRAS*, **417**, 2737

Wilkins, S. M., Bunker, A. J., Ellis, R. S., Stark, D., Stanway, E. R., Chiu, K., Lorenzoni, S., & Jarvis, M. J. 2010, *MNRAS*, **403**, 938

Wilkins, S. M., Bunker, A. J., Stanway, E., Lorenzoni, S., & Caruana, J. 2011, *MNRAS*, pp 1340–+

Williams, R. E., Blacker, B., Dickinson, M., Dixon, W. V. D., Ferguson, H. C., Fruchter, A. S., Giavalisco, M., Gilliland, R. L., Heyer, I., Katsanis, R., Levay, Z., Lucas, R. A., McElroy, D. B., Petro, L., Postman, M., Adorf, H.-M., & Hook, R. 1996, *AJ*, **112**, 1335

Windhorst, R. A., Cohen, S. H., Hathi, N. P., McCarthy, P. J., Ryan, Jr., R. E., Yan, H., Baldry, I. K., Driver, S. P., Frogel, J. A., Hill, D. T., Kelvin, L. S., Koekemoer, A. M., Mechtley, M., O'Connell, R. W., Robotham, A. S. G., Rutkowski, M. J., Seibert, M., Straughn, A. N., Tuffs, R. J., Balick, B., Bond, H. E., Bushouse, H., Calzetti, D., Crockett, M., Disney, M. J., Dopita, M. A., Hall, D. N. B., Holtzman, J. A., Kaviraj, S., Kimble, R. A., MacKenty, J. W., Mutchler, M., Paresce, F., Saha, A., Silk, J. I., Trauger, J. T., Walker, A. R., Whitmore, B. C., & Young, E. T. 2011, *ApJS*, **193**, 27

Wuyts, S., Labbé, I., Franx, M., Rudnick, G., van Dokkum, P. G., Fazio, G. G., Förster Schreiber, N. M., Huang, J., Moorwood, A. F. M., Rix, H., Röttgering, H., & van der Werf, P. 2007, *ApJ*, **655**, 51

Yan, H., Dickinson, M., Giavalisco, M., Stern, D., Eisenhardt, P. R. M., & Ferguson, H. C. 2006, *ApJ*, **651**, 24

Yan, H., Dickinson, M., Stern, D., Eisenhardt, P. R. M., Chary, R., Giavalisco, M., Ferguson, H. C., Casertano, S., Conselice, C. J., Papovich, C., Reach, W. T., Grogin, N., Moustakas, L. A., & Ouchi, M. 2005, *ApJ*, **634**, 109

Yan, H. & Windhorst, R. A. 2004, *ApJ*, **600**, L1

Yan, H., Windhorst, R. A., Hathi, N. P., Cohen, S. H., Ryan, R. E., O'Connell, R. W., & McCarthy, P. J. 2010, *Research in Astronomy and Astrophysics*, **10**, 867

Yoshida, M., Shimasaku, K., Kashikawa, N., Ouchi, M., Okamura, S., Ajiki, M., Akiyama, M., Ando, H., Aoki, K., Doi, M., Furusawa, H., Hayashino, T., Iwamuro, F., Iye, M., Karoji, H., Kobayashi, N., Kodaira, K., Kodama, T., Komiyama, Y., Malkan, M. A., Matsuda, Y.,

Miyazaki, S., Mizumoto, Y., Morokuma, T., Motohara, K., Murayama, T., Nagao, T., Nariai, K., Ohta, K., Sasaki, T., Sato, Y., Sekiguchi, K., Shioya, Y., Tamura, H., Taniguchi, Y., Umemura, M., Yamada, T., & Yasuda, N. 2006, *ApJ*, **653**, 988

Zheng, W., Bradley, L. D., Bouwens, R. J., Ford, H. C., Illingworth, G. D., Benítez, N., Broadhurst, T., Frye, B., Infante, L., Jee, M. J., Motta, V., Shu, X. W., & Zitrin, A. 2009, *ApJ*, **697**, 1907

Zheng, W., Postman, M., Zitrin, A., Moustakas, J., Shu, X., Jouvel, S., Host, O., Molino, A., Bradley, L., Coe, D., Moustakas, L. A., Carrasco, M., Ford, H., Benıtez, N., Lauer, T. R., Seitz, S., Bouwens, R., Koekemoer, A., Medezinski, E., Bartelmann, M., Broadhurst, T., Donahue, M., Grillo, C., Infante, L., Jha, S., Kelson, D. D., Lahav, O., Lemze, D., Melchior, P., Meneghetti, M., Merten, J., Nonino, M., Ogaz, S., Rosati, P., Umetsu, K., & van der Wel, A. 2012, *arXiv:1204.2305*

Appendix A

Estimating the Depth of the Stacked Photometry

To quantify the rest-frame optical properties of very faint high-redshift galaxies, in Chapter 5 we have stacked the IRAC images for a large number of faint galaxies, after removing the flux contribution from nearby neighbors (Section 5.4). While we do not expect large systematics in the photometry of individual sources from our deblending procedure to remove neighboring sources, it is possible that modest systematics could arise when stacking a large number of sources. The role of this appendix is to determine how large such systematics might be. Fortunately we are able to demonstrate that the fluxes that we measure in the stacked IRAC images are unbiased and that their significance is properly determined.

We started by selecting 200 empty areas in the HUDF field. We select them based on the segmentation maps derived from the high resolution *HST* images. We processed each of the selected empty areas as if they were the position of one of the real sources in our catalog, i.e. we ran them through the de-blending code to remove the flux from nearby un-associated sources. To determine the rms for a given $N_{\rm stacked}$ number of stacked stamps, we randomly draw (with

replacement) $N_{\rm stacked}$ stamps from the 200 empty areas, median combine them and perform aperture photometry in the median stack in the same fashion as for our real stacks. We repeat the drawing 300 times and measure the rms of these 300 trials. This determination of the noise only considers the sky background noise. This is in fact the dominant source of noise in the image; the contribution of shot noise from the faint sources considered here is less than 2%. As can be seen in the upper panel of Figure A.1, the limiting flux decreases as $\propto 1/\sqrt{N_{stacked}}$, as expected for background-limited noise. In the case of the stacks that contain real sources, the rms is larger than the image noise because it is also affected by the intrinsic variation in the distribution of fluxes that are being stacked.

As can be seen in the lower panel, the flux of the median stacks is very close to the expected zero flux.

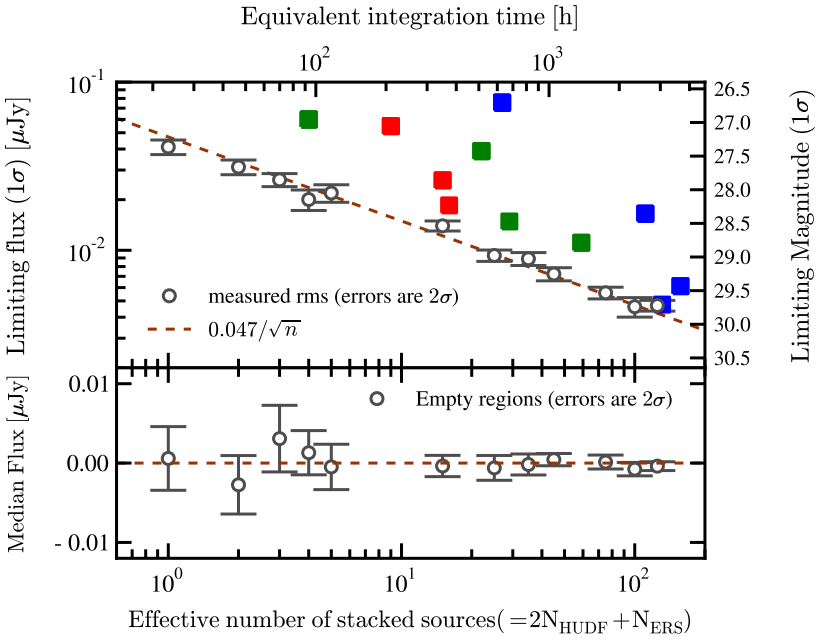

Figure A.1: *Upper:* The $1\,\sigma$ limiting flux (in μJy) as a function of the number of IRAC [3.6] stamps stacked (results are similar for the [4.5] channel but the depths are ~ 0.5 mags shallower). All the stamps have the same integration time of ~ 23.4 h. The estimates (open symbols) come from stacking large numbers of empty areas of the GOODS images. Each empty area was cleaned of neighboring fluxes using the code described in the text. The noise decreases $\propto \sqrt{n}$, with n being the number of empty regions stacked. The filled symbols are the actual RMS determined for each of our stacked stamps: blue for the $z \sim 4$ stamps, green $z \sim 5$, and red $z \sim 6$ (see Figures 5.2, 5.3, and 5.4). These RMS values are $\gtrsim$ than the ones derived for empty regions. This is expected because the uncertainties in the stack include both the image noise and intrinsic variations in the population being stacked. *Lower:* The flux of the median combined stacks of cleaned empty regions as a function of the number of stamps combined. As expected, this is very close to zero.